Master thesis and internship[BR]- Master's thesis : Hair dryer aero-acoustic study and passive solutions for noise reduction.[BR]- Integration Internship

Auteur : Lahaye, Lucile
Promoteur(s) : Terrapon, Vincent
Faculté : Faculté des Sciences appliquées
Diplôme : Master en ingénieur civil en aérospatiale, à finalité spécialisée en "aerospace engineering"
Année académique : 2021-2022
URI/URL : http://hdl.handle.net/2268.2/14383

University of Liège
Faculty of Applied Sciences

Hair dryer aero-acoustic study and passive solutions for noise reduction

Academic supervisor: Prof. Vincent Terrapon

Internship supervisor: Ir. Marie Bilterijs

Graduation Studies conducted for obtaining the Master's degree in Aerospace Engineering by Lucile Lahaye

Master thesis realised in collaboration with GDTech

Academic year 2021-2022

Hair dryer aero-acoustic study and passive solutions for noise reduction

Lucile Lahaye

Academic supervisor: Prof. Vincent Terrapon
Internship supervisor: Ir. Marie Bilterijs
Master in Aerospace Engineering
Faculty of Applied Sciences, University of Liège
Academic year 2021-2022

Abstract

Fan engines are widely used in the aeronautical industry especially for ventilation applications. However, this component generates a lot of flow-induced noise that has to be reduced to not alter the comfort of the users. In this context, this master thesis has been proposed by GDTech Engineering at the request of BaByliss in order to study the propagation of aero-acoustic sources in a hair dryer and to find solutions for noise attenuation.

To do so, a preliminary study of a point source propagation inside a rigid cylinder is carried out. This set-up makes it possible to tame the ACTRAN software through the highlight of resonance phenomenon and the analysis of propagation modes. From parameters influence studies, it is shown that only the internal cylinder of the geometry is important, indicating that the whole hair dryer study can be realised on a simple cylinder.

Lighthill analogy is then implemented based on computational fluid dynamic results for the engine inside the cylinder. The ICFD module is used to obtain the aero-acoustic surface and volume sources of noise. On one hand, the surface results show dipole distributions as a consequence of rotor-stator interaction at the harmonics of the rotor rotation speed and on the other hand, volume source linked to turbulence effects are especially marked at the blade passing frequency. The resulting sound pressure level is therefore important at all the rotor rotation speed frequency harmonics. However, these results are biased by an important numerical error.

The main objective is then to passively attenuate these peaks. Four methods are implemented based on absorbers and metamaterials. It is shown that adding a porous lining in the hair dryer casing can create a broad attenuation at high frequencies. Micro-perforated panels are also designed at the blade passing frequency but these present poorer performance. The combination of both, *i.e.* micro-perforated panels backed by a porous material, is the most efficient solution in the present case, creating a broad attenuation even more significant at the blade passing frequency. Finally, a helical metamaterial is presented to attenuate a specific lower frequency. Even if one design is shown to be satisfying, the limitations of this solution are highlighted.

Acknowledgements

My gratitude goes first to my academic supervisor Prof. Vincent Terrapon who gave me the feeling to be at the right place in these engineering studies during his Heat Transfer class. He then picked my interest for fluid dynamics, giving me the motivation to always learn more. Working under his wing was really rewarding. I also want to present my respect to Prof. Koen Hillewaert for being part of the jury.

I would also like to properly thank my internship supervisors Laurent Fitschy and Marie Bilterijs from GDTech. They welcomed me, gave me all the necessary resources and training so that I was ready to tackle the work that awaited me. In addition to them two, I could not have achieved this work without the precious help and time from Nicolas Berckmans and Adrien Ciancio from the CFD department.

Furthermore, I want to thank Julie Camal, language teacher, for her precious correction of my master thesis. Her availability was a real relief in the writing.

I pledge to honour my mother Michele Gauthy and my father Roland Lahaye. They gave me and my siblings everything a child could hope for: the incredible chance to do what we love in life. Their tireless work taught me to surpass myself and their endless love comforted me in difficult times. My family supported me relentlessly throughout this long journey, my success is theirs.

A big thank also goes to my friends. They surrounded me with a positive atmosphere throughout my studies and especially during my master's thesis. They all should know that their support is what motivates me everyday to achieve my work. A special mention goes to Aurore Schmitz, I am so grateful these studies led me to meet her.

Finally, I would like to conclude by expressing my gratitude to Mrs. Lesoinne, my high school mathematics teacher. He gave me a taste for mathematics and I would not be there without his subtle provocations.

Contents

List of Figures vi

List of Tables ix

1 Introduction 1
- 1.1 Context and motivations . . . 1
- 1.2 Objectives and methodology . . . 2
- 1.3 Actran software . . . 3
- 1.4 Structure of the work . . . 3

2 Theoretical background 4
- 2.1 Generalities . . . 4
- 2.2 Governing equations . . . 5
- 2.3 Fourier analysis . . . 7
  - 2.3.1 Fourier series . . . 7
  - 2.3.2 Fourier transform . . . 8
- 2.4 Helmholtz equation . . . 8
- 2.5 Acoustic impedance . . . 9
- 2.6 Acoustic intensity . . . 10
- 2.7 Sound level . . . 10
- 2.8 Interaction with medium boundaries . . . 11

3 Preliminary study 14
- 3.1 Study case . . . 14
- 3.2 Resonance . . . 15
- 3.3 Analytical solution . . . 15
- 3.4 Numerical solution . . . 17
  - 3.4.1 Basic set-up . . . 18
    - 3.4.1.1 Geometry . . . 18
    - 3.4.1.2 Components . . . 18
    - 3.4.1.3 Boundary conditions . . . 18
    - 3.4.1.4 Acoustic excitation . . . 18
    - 3.4.1.5 Post-processing . . . 19

3.4.2 Convergence studies . . . 19
3.4.2.1 Mesh . . . 20
3.4.2.2 Infinite surface . . . 21
3.4.3 Results . . . 24
3.4.4 Influence studies . . . 27
3.4.4.1 Non-reflecting boundary condition . . . 27
3.4.4.2 Source position . . . 28
3.4.4.3 Complex geometry . . . 28

4 Aero-acoustic sources **30**
4.1 Fan noise . . . 30
4.2 Lighthill analogy . . . 31
4.3 Numerical implementation . . . 33
4.3.1 CAD model . . . 34
4.3.2 CFD analysis . . . 34
4.3.3 Acoustic set-up . . . 35
4.3.4 ICFD . . . 37
4.3.5 Numerical results . . . 38
4.4 Comparison with experiments . . . 40

5 Noise attenuation **41**
5.1 Acoustic set-up . . . 41
5.2 Acoustic Absorbers . . . 42
5.2.1 Porous/fibrous materials . . . 43
5.2.1.1 Theoretical background . . . 43
5.2.1.2 Numerical implementation . . . 45
5.2.2 Perforated panels . . . 49
5.2.2.1 Theoretical background . . . 49
5.2.2.2 Numerical implementation . . . 52
5.2.3 Micro-perforated panels with porous materials . . . 55
5.2.3.1 Theoretical background . . . 55
5.2.3.2 Numerical implementation . . . 55
5.2.4 Discussion . . . 58
5.3 Metamaterials . . . 59
5.3.1 Theoretical background . . . 59
5.3.2 Numerical implementation . . . 61
5.3.3 Experimental results . . . 66
5.4 Final combination . . . 68

6 Conclusion **70**
6.1 Key results . . . 70
6.2 Further works . . . 71
6.2.1 Major improvement . . . 72
6.2.2 Air flux verification . . . 72
6.2.3 Three speeds generalisation . . . 72

6.2.4 Engine modifications 72
6.2.5 Active noise control 73

Appendices **74**

A Fourier transform properties **74**

B Bessel equation and functions **75**

Bibliography **77**

List of Figures

1.1 Complete hair dryer device received from BaByliss. 2

2.1 Mechanical acoustic wave propagation from a source as pressure fluctuations. 5
2.2 Representation of the one dimensional solution of the wave equation that is the superposition of two waves travelling in opposite directions at speed c [31]. 7
2.3 Total plane wave reflection on a rigid wall [31]. 12
2.4 Total plane wave reflection on a soft wall [31]. 12

3.1 Dimensions and position of the point source in the studied geometry. 14
3.2 Pressure distribution of the first three eigenmodes of an open-open tube. . . 17
3.3 Set-up created in ACTRAN showing the components, the boundary conditions and the excitation. 19
3.4 Decomposition of a sinus in 8 linear elements. 20
3.5 SPL as a function of the frequency for three different mesh element sizes at a microphone placed in the middle of the cylinder. 20
3.6 SPL as a function of the frequency for four different ellipsoids at a microphone placed at 20 cm of the cylinder extremity for a mesh of 1.7 mm. 22
3.7 SPL as a function of the frequency for three different interpolation orders at a microphone placed at 20 cm of the cylinder extremity for a mesh of 1.7 mm and an ellipsoid of size 15-15-30 [cm]. 23
3.8 Visualisation of the final mesh for a cutting plane perpendicular to the z-axis obtained in ACTRAN. 24
3.9 SPL based on the mean acoustic pressure as a function of the frequency with infinite elements boundary condition. 25
3.10 Sound pressure level pattern of the transversal modes. 26
3.11 Sound pressure level output maps at the first four resonance frequencies. . . 26
3.12 SPL based on the mean acoustic pressure as a function of the frequency with non-reflecting surfaces boundary condition. 27
3.13 SPL based on the mean acoustic pressure as a function of the frequency for the centred and shifted source cases with infinite elements boundary condition. 28
3.14 Simplified hair dryer geometry. 29
3.15 SPL based on the mean acoustic pressure as a function of the frequency for the simple and complex geometries with infinite elements boundary condition. 29

4.1 ACTRAN process for the computation of aero-acoustic sources [42]. 33
4.2 Rotor stator geometry of engine *Keli* provided by BaByliss. 34
4.3 Polyhedral mesh of the rotor stator geometry with the rotating mesh in red and static mesh in grey. 35
4.4 Acoustic set-up with Lighthill surfaces in red and Lighthill volume in green. 36
4.5 SPL as a function of the frequency for three different interpolation orders at a microphone placed at 20 cm of the cylinder extremity for a mesh of 1.7 mm and an ellipsoid of size 15-15-30 [cm]. 36
4.6 Acoustic Lighthill surfaces source terms expressed in [kg/(m^{2}s^2)] for three frequencies: 1 250, 2 500 and 16 250 Hz. 38
4.7 Acoustic Lighthill volume source terms expressed in [kg/(m^{3}s^2)] for three frequencies: 1 250, 2 500 and 16 250 Hz. 38
4.8 SPL as a function of the frequency for three loadcases: Lighthill surfaces, Lighthill volume or both boundary conditions at a microphone placed at 1 m of the cylinder axis, perpendicularly to it. 39
4.9 SPL as a function of the frequency provided by BaByliss for engine *Keli* at a microphone placed at 1 m on the transversal axis of the engine. 40

5.1 Representation of the polar virtual microphones in blue with micro 1 in red. 42
5.2 Concepts of incidence, reflection, dissipation and transmission through an absorber layer. 42
5.3 Absorption coefficient α as a function of the frequency for different depths of porous cavity using Miki model with R=22 000 N·s/m^4. 44
5.4 Porous cavities (in red) in the internal thickness of the cylinder. 45
5.5 SPL as a function of the frequency at micro 1 without absorber and for three different cavity depths with R=22 000 N·s/m^4. 45
5.6 SPL at different frequencies obtained at the polar set of microphones without absorber and for three different cavity depths with R=22 000 N·s/m^4. 46
5.7 SPL at 16 250 Hz obtained at the polar set of microphones for a thicknesses of porous absorber equal to 5.5 mm and three different resistivities R. 47
5.8 SPL as a function of the frequency at micro 1 without absorber and for a 7.5 mm porous cavity depth with R=22 000 N·s/m^4. 48
5.9 SPL at 1 250 Hz obtained at the polar set of microphones without absorber and for a 7.5 mm porous cavity depth with R=22 000 N·s/m^4. 48
5.10 Schematic of an Helmholtz resonator equivalent to a spring mass system. . . 49
5.11 Optimal air cavity depth D_{opti} as a function of the frequency for different fractional open area σ. 51
5.12 Maximum absorption coefficient α_{max} obtained with D_{opti} from figure 5.11 as a function of the frequency for different fractional open area σ. 51
5.13 Absorption coefficient as a function of the frequency for three MPPs described in table 5.2. 52
5.14 SPL as a function of the frequency at micro 1 without absorber and for three MPPs listed in table 5.2. 53
5.15 SPL at different frequencies obtained at the polar set of microphones without absorber and for three MPPs listed in table 5.2. 54

5.16 Absorption coefficient as a function of the frequency for three MPPs described in table 5.2 and the comparison with the same MPPs backed by porous cavities. 55
5.17 SPL as a function of the frequency at micro 1 without absorber and for three types of MPPs backed by porous cavities. 56
5.18 SPL at different frequencies obtained at the polar set of microphones without absorber and for three types of MPPs backed by air or porous material filled cavities. 57
5.19 Transverse bilayer metamaterial as theoretically presented in [16] for a wave with normal incidence. 60
5.20 Ultra-open metamaterial with channels coiled in the form of helix with region 1 for $0<r<r_1$ and region 2 for $r_1<r<r_2$. 60
5.21 Ultra open metamaterial (in red) added in the cylinder set-up. 61
5.22 SPL as a function of the frequency at micro 1 for the two geometries. 62
5.23 SPL output map [dB] at 1 250 Hz for the two geometries. 62
5.24 SPL as a function of the frequency at micro 1 without metamaterial and for three metamaterials as described in table 5.6. 63
5.25 SPL at 1250 Hz obtained at the polar set of microphones without metamaterials and for three metamaterials as described in table 5.6. 63
5.26 Pressure phase output map at 1 250 Hz for Meta 1. 64
5.27 SPL output map at 1 250 Hz for Meta 1. 64
5.28 SPL as a function of the frequency at microphone 1 without metamaterial and for three metamaterials as described in table 5.7. 66
5.29 SPL as a function of the frequency at microphone 1 without metamaterial and for two metamaterials as described in table 5.7. 66
5.30 Cylinder with Meta 1 3D printed in ABS. 67
5.31 Experiments set-up in an anechoic room with the suspended model. 67
5.32 SPL as a function of the frequency from experiments for the engine *Keli* inside a simple cylinder and inside a cylinder with Meta 1. 68
5.33 SPL as a function of the frequency at micro 1 without attenuation solution and for the combination of Meta 1 and MPP 3 porous backed. 69
5.34 SPL at different frequencies obtained at the polar set of microphones without attenuation solution and for the combination of Meta 1 and MPP 3 porous backed. 69

List of Tables

2.1 Sound pressure level with examples of characteristics sound levels in common environment [47]. 11

3.1 Cut-off frequencies f_{mn} [Hz] of mode (m,n) in the audible range for a cylinder of radius $R = 15.5$ mm. 16
3.2 Plane wave uncorrected and corrected resonance frequencies f_n for a cylinder of length $l = 200$ mm and radius $R = 15.5$ mm. 17
3.3 Number of elements obtained, simulation time needed (per frequency), memory necessary (per frequency) and coordinates of the first peak in figure 3.5b for three element sizes. 21
3.4 Number of elements obtained, simulation time needed (per frequency) and memory necessary (per frequency) for four ellipsoid sizes. 22
3.5 Simulation time needed (per frequency) and memory necessary (per frequency) for three interpolation orders. 23

5.1 Mean SPL [dB] at different frequencies over the polar set of microphones for three thicknesses of porous absorber and without absorber. 47
5.2 Identifier, radius a, thickness l, porosity σ leading to an optimal cavity depth D at 16 250 Hz of three MPPs. 52
5.3 Mean SPL [dB] at different frequencies over the polar set of microphones for three types of MPP presented in table 5.2 and without absorber. 54
5.4 Mean SPL [dB] at different frequencies over the polar set of microphones for three types of MPPs backed by porous cavities and without absorber. 57
5.5 Mean attenuation [dB] over the polar set of microphones for the different types of absorbers with the best result highlighted in red for each frequency. 58
5.6 Identifier, helix angle ϕ, thickness t, internal radius r_1 and external radius r_2 of five ultra open metamaterials (1,2,3,4,5). 62
5.7 Identifier, helix angle ϕ, thickness t, internal radius r_1 and external radius r_2 of six ultra open metamaterials (1,6,7,8,9,10). 65

B.1 mth first zeros ξ_{mn} of the derivative of the Bessel functions $J'_n(\xi)$ for n=0, 1, 2, 3, 4 and 5. 76

Chapter 1

Introduction

1.1 Context and motivations

Noise is defined by the NASA as "*an acoustic phenomenon producing an auditory sensation considered unpleasant or annoying*" [35]. With the development of road and air transport, industrialisation and construction activities, noise is becoming a ghost pollution of the modern society. Environmentally or man-made, people often do not have the control on the noise in which they live. What is problematic is that it can lead to unsuspected health problems. The World Health Organisation reported although seven categories of adverse health effects induced by noise [37]. Among them, depression, anxiety, concentration issues, sleep difficulties, hearing impairment and cardiovascular disturbances are the most highlighted.

In this context, developers of new technologies are compelled to take their customers' noise sensitivity into account. Beyond performance, price or design, the sound level generated by new devices is now entering the race in comparative studies. In order to compete, appliance brands among others are forced to create new designs that produce the least noise possible, keeping them compact and economical. In this framework, BaByliss, professionals in the creation of electrical hairdressing appliances, contacted GDTech Engineering [15] to realise an acoustic study of a hair dryer. GDTech is an engineering consultancy office located in Alleur, in Belgium, that integrated this research work as part of a master thesis.

Acoustics, the physical study of sound, is then the main subject of this work. This discipline is a very large topic that can be applied to various arts and sciences. To cite a few, branches such as architecture, music, biology, oceanography, medicine, vibration mechanics require the application of acoustics. Especially, the present work focuses on aero-acoustics. This specific field studies the generation of sound from turbulent fluid motion and aerodynamic forces created from interaction with boundaries. It is of application here since the hair dryer contains a ducted fan engine composed of a rotor-stator system that generates noise due to the interaction with the air that is then propagated in a duct. Great care has therefore been taken to highlight the fluid mechanic concepts involved in the acoustics study.

1.2 Objectives and methodology

The main purpose of this master thesis is to provide a solution to attenuate the noise produced by a hair dryer in order to provide a more comfortable environment for users. The complete hair dryer on which the study is based is shown in figure 1.1. To achieve the objective, a few steps are first necessary to understand the source of noise and the different mechanisms of attenuation.

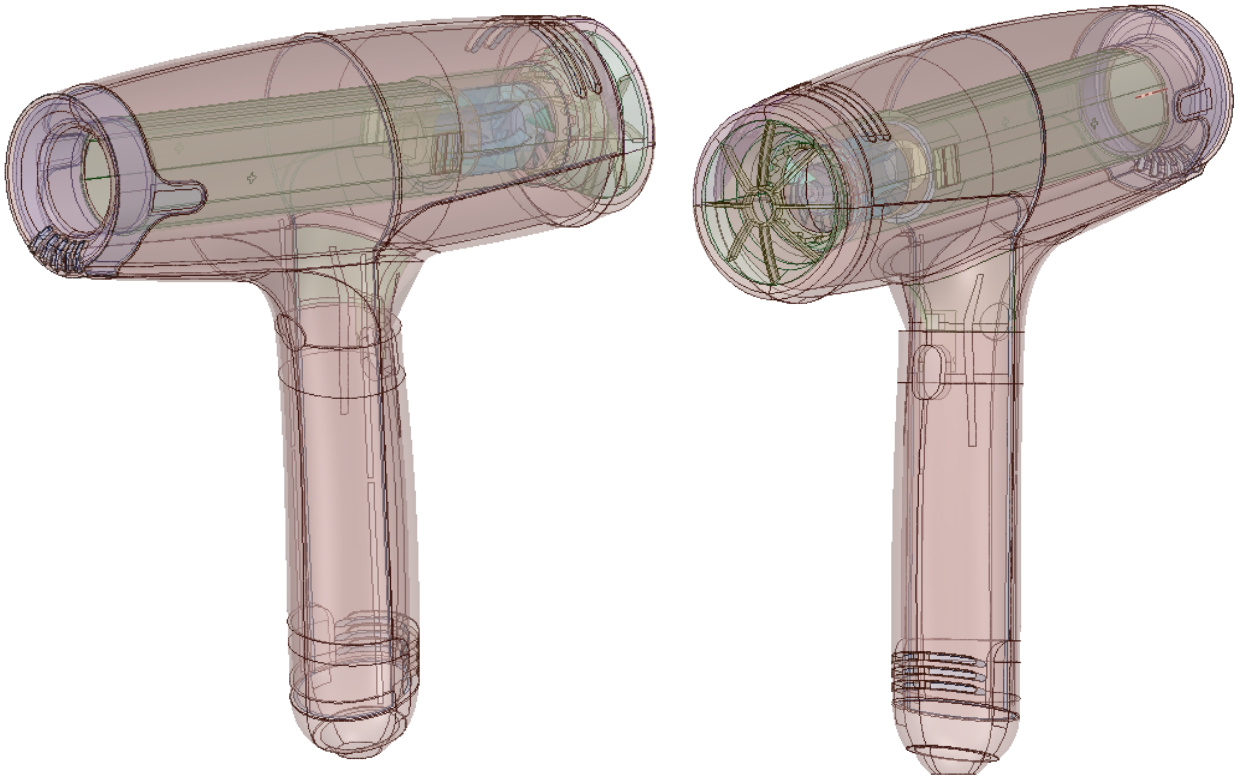

Figure 1.1: Complete hair dryer device received from BaByliss.

The method consists in first studying the geometry of a simple cylinder and its way of propagating a point source. This helps understanding the basic principles of linear acoustics and resonance. After that, the case is made more complex by replacing the point source by the real noise source which is that generated by the interaction between the rotor and the stator. It is thus an aero-acoustic study that can be compared to experimental results provided by BaByliss. Finally, mainly based on literature review, various passive mitigation solutions can be proposed. However, some constraints apply, such as the fact that the engine is fixed and therefore not a degree of freedom in the study and that the solution must be implemented in the restricted space of the internal casing without altering the air flow.

To reach this goal, theoretical researches are led and various numerical simulations are created using the Actran software detailed further. This enables to obtain analytical results and to numerically test them. Results can then be interpreted and the most promising solutions can eventually be experimentally tested on the geometry.

1.3 Actran software

Actran (acronym of ACoustic TRANsmission) is a Belgian software created by the company Free Field Technologies (FFT) founded in 1998. It is a finite element program written in Python and C++ languages that contains different modules to handle mainly acoustic, aero-acoustic and vibro-acoustic propagation. The software contains an exhaustive finite elements library, a large choice of materials and a high quantity of possible boundary conditions and acoustic excitations [42].

The calculation procedures can be of various types but the most usual analysis type, the one used in this work, is the direct frequency response. In this case, the system of equations that is solved is the general equation of movement converted in the frequency domain:

$$\underline{\underline{M}}\ \underline{\ddot{x}}(t) + \underline{\underline{C}}\ \underline{\dot{x}}(t) + \underline{\underline{K}}\ \underline{x}(t) = \underline{F}(t) \tag{1.1}$$

$$\Leftrightarrow \tag{1.2}$$

$$(\underline{\underline{K}} + i\omega\underline{\underline{C}} - \omega^2\underline{\underline{M}})\ \underline{X}(\omega) = \underline{F}(\omega) \tag{1.3}$$

where $\underline{\underline{K}}$, $\underline{\underline{C}}$ and $\underline{\underline{M}}$ are respectively the stiffness, damping and mass matrices of the system. The computation of $\underline{X}(\omega)$ is done for a fixed number of pulsations $\omega = 2\pi f$ determined in the analysis set-up.

1.4 Structure of the work

The present work is divided into six chapters. After this introductory one, chapter 2 is a summary of the important concepts of linear acoustics that are necessary to understand the rest of the thesis. It presents the derivation of the global wave equation and other theoretical tools essential to explain and characterise acoustic phenomena. After that, a preliminary study is realised on a cylinder in chapter 3. It first states the principle of resonance and presents the analytical solution of the simplified geometry studied. Then, it describes the numerical set-up created in Actran and the results obtained in this simple source point case to finally study the influence of different parameters on the solution. Chapter 4 allows to go a step further by presenting the Lighthill analogy for an aero-acoustic study of the case. A theoretical part introduces the numerical implementation of the analogy based on computational fluid dynamic (CFD) analysis. Furthermore, the solutions for noise attenuation are presented in a fifth chapter divided into two categories: the acoustic absorbers and the metamaterials. Each of these sections put forward the concepts first in a theoretical way and then thanks to numerical analysis. Finally, the work is concluded in the last chapter with some additional perspective for further studies.

Chapter 2

Theoretical background

An introduction to the linear theory of sound wave motion is presented. The hypotheses made and the foundations of acoustic propagation in non-dissipative media are briefly laid in order to facilitate the reading of the work thereafter. This summary is mainly based on the book "Acoustic" from Migeot *et al.* [31]. Other more specific theoretical concepts on aero-acoustics and noise attenuation are further introduced in corresponding chapters.

2.1 Generalities

Acoustics is the science concerned with the generation, transmission and reception of energy as mechanical waves in matter. A mechanical acoustic wave is a disturbance that constitutes an oscillation of particles in a medium and that propagates longitudinally. This movement of particles illustrated in figure 2.1 creates alternate zones of high (compression) and low (expansion) pressure and this pressure fluctuation is perceived as sound. The acoustic pressure $p_a(t)$, measured in Pascal [Pa], is thus mathematically defined as

$$p_{tot}(t) = p(t) = p_0 + p_a(t) \quad \text{with} \quad p_0 >> p_a(t) \tag{2.1}$$

where

$$p_0 = \frac{1}{T}\int_{t_0}^{t_0+T} p_{tot}(t)\ dt, \tag{2.2}$$

T being a period of time much larger than the acoustic fluctuations time scale. The mean value p_0 is the atmospheric pressure taken equal to $1.01{\cdot}10^5$ Pa. Audible pressure fluctuations are in the range $2{\cdot}10^{-5}$ Pa to 10 Pa.

Frequency, measured in Hertz [Hz], corresponds to the number of oscillations per second; it can then characterise a sound. The spectral range of sound can be divided in different categories: infra-sounds, sounds, ultra- and hyper-sounds. The audible range corresponds to [20;20 000] Hz, frequencies to which the human ear is sensible. A low frequency creates a low sound, while a higher frequency makes a high-pitched sound.

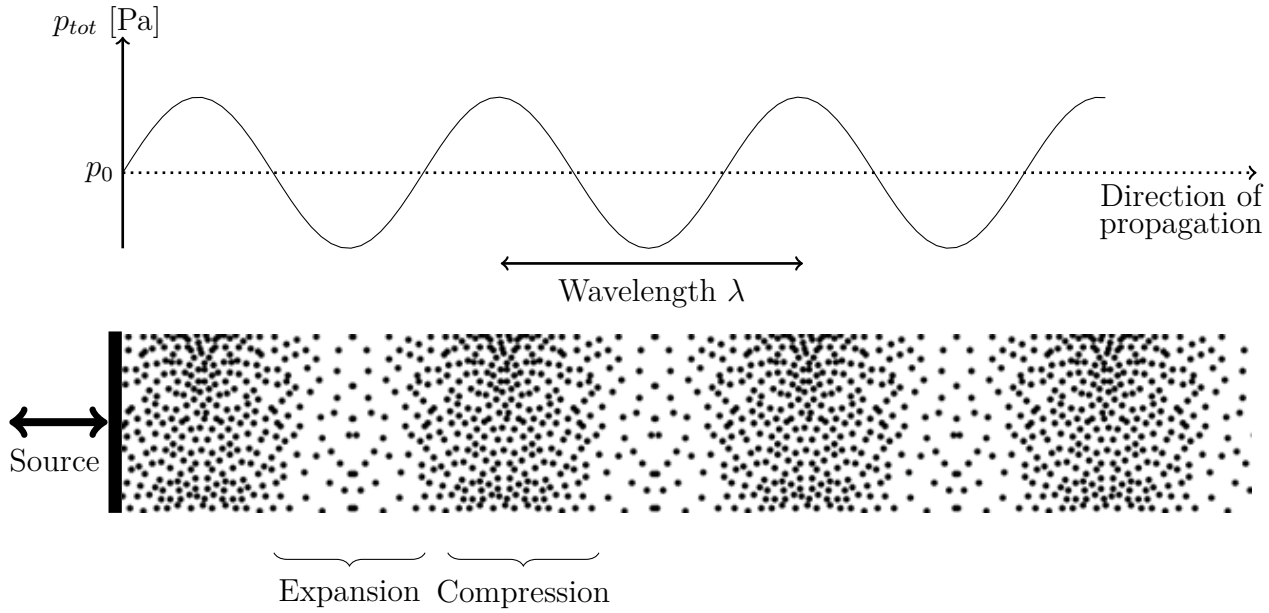

Figure 2.1: Mechanical acoustic wave propagation from a source as pressure fluctuations.

An important feature is that nearly all acoustic systems are linear in nature. For most audible sounds, air is indeed a linear medium. This means that the sound pressure in the air is simply the sum of the sound pressures from every sources present. In these cases, superposition and proportionality principles can be applied. Conversely, non-linearity is present when the amplitude of the pressure variation is of the order of or greater than p_0, when the properties of the medium in which the wave propagates is dependent on pressure or when the amplitude of the source depends on the generated sound. Linearisation of the governing equations, as presented in the next section, are in those cases not possible. This is however not the case in this work.

2.2 Governing equations

The fundamental equation of acoustics that governs the pressure fluctuations is established from the Navier-Stokes equations, *i.e.* the continuity and the momentum equations, in the following form:

$$\begin{cases} \partial_t \rho + \partial_i(\rho v_i) = q, \\ \rho(\partial_t v_i + v_j \partial_j v_i) - \partial_i \tau_{ij} = -q v_i \end{cases} \tag{2.3}$$

where the state variables pressure p, density ρ and velocity $\underline{v}$ describe the fluid properties. In this formulation, τ_{ij} is the stress tensor and a distributed source of mass q is taken into account. The theory of linear acoustics exploited in this work is based mainly on six key hypotheses:

1. The propagation is adiabatic because even if the fluid heats up during the compression and cools down when expanding, this process is so rapid that no appreciable thermal energy is transferred;

2. The propagation of the acoustic wave is done in a fluid for which the viscosity can be neglected: $\tau_{ij} = -p\delta_{ij}$;

3. The pressure and the density of the particles can be divided into two contributions: a mean reference and a fluctuating part which is much smaller:

$$p = p_0 + p_a, \quad p_a << p_0, \tag{2.4}$$
$$\rho = \rho_0 + \rho_a, \quad \rho_a << \rho_0, \tag{2.5}$$

   where $\rho_0 = 1.225$ kg/m^3;

4. The fluid is barotropic $p = p(\rho)$ and therefore, Taylor expansion around point (p_0, ρ_0) gives:

$$p(\rho_0 + \rho_a) = p(\rho_0) + (\rho - \rho_0)\left(\frac{\partial p}{\partial \rho}\right)_{\rho=\rho_0} + \mathcal{O}((\rho - \rho_0)^2). \tag{2.6}$$

   Since $p(\rho_0) = p_0$, it follows the linearised constitutive relationship:

$$p_a = c^2 \rho_a, \tag{2.7}$$

   where $c^2 = \left(\frac{\partial p}{\partial \rho}\right)_{\rho=\rho_0}$ is the speed of sound in perfect gases equal to 340 m/s;

5. The fluid is globally at rest:

$$v_{0i} = 0 \quad \text{and} \quad v_{ai} << c, \tag{2.8}$$

   which is a reasonable assumption since the Mach number considered in a hair dryer is around M=0.08 what does not have a significant effect on the acoustic propagation;

6. There is no distributed sources of mass: q=0.

The relationships resulting from linearisation of the equations mentioned above are the wave and the pressure-velocity equations for the acoustic disturbances p_a and $\underline{v}_a$:

$$\frac{1}{c^2}\frac{\partial^2 p_a}{\partial t^2} - \Delta p_a = 0, \tag{2.9}$$
$$\frac{\partial \underline{v_a}}{\partial t} = -\frac{1}{\rho_0}\underline{\nabla} p_a. \tag{2.10}$$

In the following developments, the indices "a" are not explicitly mentioned anymore to lighten the notations.

It can easily be demonstrated that the one-dimensional solution of the wave equation 2.9 takes the following form:

$$p(x,t) = p^+\left(t - \frac{x}{c}\right) + p^-\left(t + \frac{x}{c}\right). \tag{2.11}$$

The first contribution is a wave travelling at a speed c from left to right and the second one is also a wave travelling at speed c but from right to left, as represented in figure 2.2.

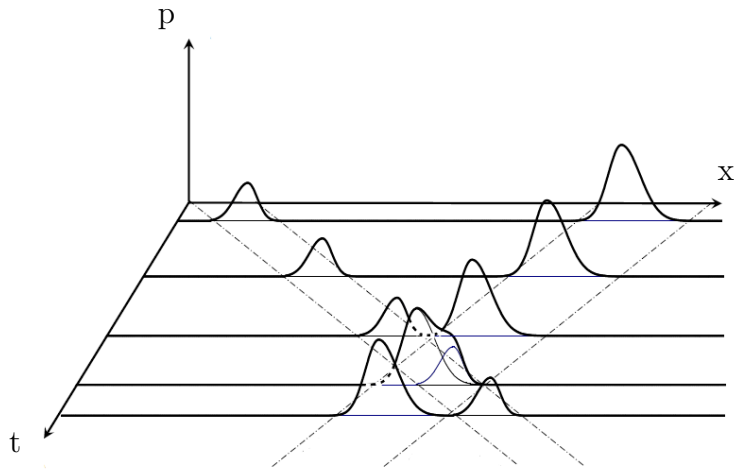

Figure 2.2: Representation of the one dimensional solution of the wave equation that is the superposition of two waves travelling in opposite directions at speed c [31].

The wave equation 2.9 can also be written in spherical coordinates, considering a purely radial solution:

$$\frac{\partial^2(pr)}{\partial r^2} - \frac{1}{c^2}\frac{\partial^2(pr)}{\partial t^2} = 0. \tag{2.12}$$

A spherical wave is a wave propagating from a point source symmetrically in all directions. The one-dimensional solution of this equation is

$$p(r,t) = \frac{p^+(t-\frac{r}{c})}{r} + \frac{p^-(t+\frac{r}{c})}{r}. \tag{2.13}$$

It also represents the sum of two waves: a symmetric disturbance propagating at speed c in the positive radial direction and an incoming wave converging at $r = 0$. By the causality condition stating that sound created by a source must be propagated away from this source, the second term is nonphysical and is therefore suppressed from the solution.

2.3 Fourier analysis

Fourier analysis allows to decompose general functions into simpler elementary signals such as trigonometric or exponential functions. In the case of periodic signals, the expansion is called Fourier series and the generalisation to non-periodic functions is the Fourier transform.

2.3.1 Fourier series

If $p(t)$ is a periodic signal of period T such as

$$\exists T : \forall t : p(t+T) = p(t), \tag{2.14}$$

it can be written as a discrete sum of trigonometric functions with specific frequencies equally spaced, called harmonics $\Delta f = 1/T$. Its Fourier series is therefore:

$$p(t) = \sum_{n=0,\infty} A_n \cos(\omega_n t) - \sum_{n=0,\infty} B_n \sin(\omega_n t) \tag{2.15}$$

where $\omega_n = 2n\pi/T$. The Fourier coefficients are found to be

$$A_m = \frac{2}{T}\int_{t_0}^{t_o+T} p(t)\,\cos(\omega_m t)dt, \tag{2.16}$$

$$B_m = \frac{-2}{T}\int_{t_0}^{t_0+T} p(t)\,\sin(\omega_m t)dt. \tag{2.17}$$

2.3.2 Fourier transform

The Fourier transform is a generalisation of the Fourier series expansion for non necessarily periodic signals. This tool allows to work in the frequency domain and to associate to each time domain signal an integral of exponential functions with a continuum in frequencies or pulsation ω:

$$p(t) = \frac{1}{2\pi}\int_{-\infty}^{\infty} P(\omega)e^{i\omega t}d\omega, \tag{2.18}$$

$$\Leftrightarrow P(\omega) = \int_{-\infty}^{\infty} p(t)e^{-i\omega t}dt, \tag{2.19}$$

where $P(\omega)$ is in [Pa·s].

2.4 Helmholtz equation

Taking the Fourier transform of equation 2.9 (cf. appendix A for the Fourier transform properties) gives the Helmholtz equation:

$$\Delta P(\omega) + k^2 P(\omega) = 0 \tag{2.20}$$

where $P(\omega)$ is the sound pressure spectrum and $k = \omega/c$ is the wave number. The one dimensional plane and spherical wave general solutions to equations 2.11 and 2.13 in the frequency domain are respectively

$$P(x,\omega) = P^+(\omega)e^{-ikx} + P^-(\omega)e^{ikx}, \tag{2.21}$$

$$P(r,\omega) = P^+(\omega)\frac{e^{-ikr}}{r}. \tag{2.22}$$

A solution in three dimensions can also be developed for the Helmholtz equation. Considering a pressure field

$$P(\underline{r},\omega) = X(x)\cdot Y(y)\cdot Z(z) \tag{2.23}$$

and inserting it into equation 2.20:

$$\frac{1}{X}\frac{d^2X(x)}{dx^2} + \frac{1}{Y}\frac{d^2Y(y)}{dy^2} + \frac{1}{Z}\frac{d^2Z(z)}{dz^2} + k^2 = 0, \tag{2.24}$$

it can be seen that each term must be constant for the left hand side to equal zero. Then, for the first as for the two other terms:

$$\frac{1}{X}\frac{d^2X(x)}{dx^2} = -k_x^2 \Rightarrow X(x) = Ae^{-ik_x x} \tag{2.25}$$

and the function

$$P(\underline{r},\omega) = P \cdot e^{-i(k_x x + k_y y + k_z z)} = P \cdot e^{-i\underline{k}\cdot\underline{r}} \tag{2.26}$$

is a solution of the 3D Helmholtz equation only if the dispersion relation holds:

$$k^2 = k_x^2 + k_y^2 + k_z^2. \tag{2.27}$$

Furthermore, the Fourier transform can also be applied on equation 2.10 what yields an equation linking the acoustic velocity and pressure gradient spectra:

$$V_j(\omega) = \frac{i}{\rho_0 \omega} \partial_j P(\omega). \tag{2.28}$$

2.5 Acoustic impedance

The ratio between the amplitudes of the acoustic pressure and velocity spectra at one point is defined as the acoustic impedance:

$$Z_j(\omega) = \frac{P(\omega)}{V_j(\omega)} \tag{2.29}$$

where j is the direction considered, usually normal to the boundary. The acoustic impedance of a medium characterises its resistance to the passage of an acoustic wave. Therefore, a perfectly rigid wall and a soft surface have a normal impedance $Z_n(\omega)$ which is respectively infinite ($v_n = 0$) and zero ($p = 0$).

Considering a plane wave travelling in air towards the positive x:

$$P(x,\omega) = P^+(\omega) e^{-ikx}, \tag{2.30}$$

the velocity spectrum can be deduced from equation 2.28:

$$V_x(x,\omega) = \frac{P^+(\omega)}{\rho_0 c} e^{-ikx}. \tag{2.31}$$

The acoustic air impedance through equation 2.29, is then

$$Z_c = \rho_0 c. \tag{2.32}$$

This particular impedance $\rho_0 c$, independent of the position x, is called the characteristic impedance. The normal acoustic impedance of a material is usually compared to this one by defining the reduced impedance coefficient as:

$$z_n = \frac{Z_n}{Z_c}. \tag{2.33}$$

The surface impedance is a complex quantity where the real part is the acoustic resistance and the imaginary part is the acoustic reactance.

2.6 Acoustic intensity

The instantaneous sound intensity $i(t)$, measured in [W/m^2], is defined as the power per unit area required for the sound wave to propagate in a direction perpendicular to this area. It is therefore computed as the product of the instantaneous pressure $p(t)$ and velocity $v(t)$. Its spectrum is then represented in the frequency domain by a convolution:

$$I(\omega) = \frac{1}{2\pi} \int_{-\infty}^{\infty} P(\sigma) \cdot V(\omega - \sigma) d\sigma. \tag{2.34}$$

The active intensity $I(\omega = 0)$ is a constant part of the spectrum $I(\omega)$. It can be proved by mathematical developments in the frequency domain that its spectral density is given by:

$$I(\omega) = \frac{Z_r}{Z_r^2 + Z_i^2} \frac{\left|P^+(\omega)\right|^2}{2} \tag{2.35}$$

where Z_r and Z_i are respectively the real and imaginary parts of the local acoustic impedance $Z(\omega)$.

2.7 Sound level

The intensity of a sound pressure is measured through the sound pressure level (SPL) which is the comparison between the root mean square pressure at the considered point and a reference pressure:

$$L_p = 20 \log \frac{p_{RMS}}{p_{ref}} = 20 \log \frac{p}{\sqrt{2} p_{ref}} \tag{2.36}$$

where p_{ref} is $2 \cdot 10^{-5}$ Pa in the air, corresponding to the magnitude of the acoustic pressure at the threshold of perception in the frequency domain where the ear sensitivity is maximum. This quantity is measured in decibels [dB]. An idea of common environment sources and their resulting sound pressure level is presented in table 2.1.

It is also possible to represent the magnitude of the acoustic wave assuming the intensity proportional to the square of the acoustic pressure:

$$L_I = 10 \log \frac{I}{I_{ref}} \tag{2.37}$$

where $I_{ref} = 10^{-12}$ W/m^2.

To better understand the general idea of the noise level addition, it is important to mention that the global sound level perceived by the combination of two sources A and B is computed by adding their intensities:

$$L_{tot} = 10 \log \left(\frac{p_{A,eff}^2}{p_{ref}^2} + \frac{p_{B,eff}^2}{p_{ref}^2} \right). \tag{2.38}$$

From this equation, it can be shown that the combination of two identical levels results in a level that is 3 dB higher than the one perceived with only one of those sources.

Sound pressure level [dB]	Common environment sources
120	jet engine nearby
110	police siren nearby
100	inside subway train, discotheque
90	using hair dryer
80	truck passing by, loud radio music
70	street with car traffic, loud conversation
60	normal conversation at office
50	moderate rainfall
40	quiet residential area, refrigerator
30	whispering
20	rustling leaves
10	breathing
0	inaudible, hearing threshold

Table 2.1: Sound pressure level with examples of characteristics sound levels in common environment [47].

2.8 Interaction with medium boundaries

When rigid, free or partially absorbing surfaces are interfering with propagating waves in air, two interesting phenomena can happen: the incident wave is partially reflected back and partially absorbed by the material. The nature of these phenomena depends on the media properties (ρ and c), the type of boundary surface (planar or irregular), the incident front wave (planar, spherical or random wave) and the angle of incidence.

Considering a plane wave hitting a planar surface located at $x = 0$ with normal incidence, the dimensional pressure and velocity distributions are at that point:

$$P(0,\omega) = P^{+}(\omega) + P^{-}(\omega) \tag{2.39}$$

$$V_x(0,\omega) = \frac{P^{+}(\omega) - P^{-}(\omega)}{\rho_0 c}. \tag{2.40}$$

Different conditions can then be considered. For instance, if the surface is a rigid wall, a zero velocity condition is imposed at that point. Therefore, $P^{+}(\omega) = P^{-}(\omega)$ and total reflection

is obtained, the absorption is null. In this case, the surface is seen as a mirror on which the acoustic pressure is twice that of the incident wave. An other extreme configuration is the free surface in which case a zero pressure is fixed on the boundary. The whole incident energy is reflected back with the same amplitude but with a phase difference of π. These two extreme cases are represented in figures 2.3 and 2.4.

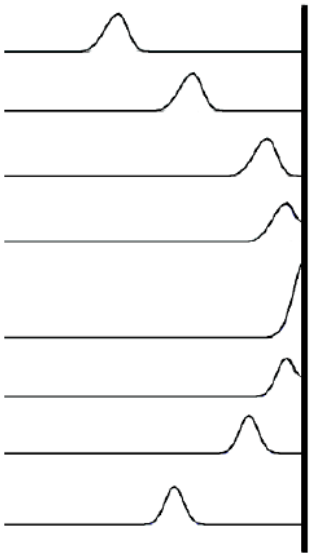

Figure 2.3: Total plane wave reflection on a rigid wall [31].

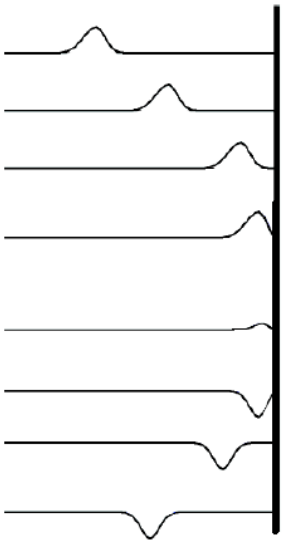

Figure 2.4: Total plane wave reflection on a soft wall [31].

An intermediate boundary condition is the absorbing surface for which the acoustic impedance is

$$Z(\omega) = \rho_0 c \, \frac{P^+(\omega) + P^-(\omega)}{P^+(\omega) - P^-(\omega)}. \tag{2.41}$$

The reflection factor $R(\omega)$ is defined as

$$R(\omega) = \frac{P^-(\omega)}{P^+(\omega)} = \frac{Z(\omega) - \rho_0 c}{Z(\omega) + \rho_0 c}. \tag{2.42}$$

Furthermore, using equation 2.35, the incident and reflected intensities are given by:

$$I_{inc} = \frac{\left|P^+(\omega)\right|^2}{2\rho_0 c} \tag{2.43}$$

$$I_{ref} = \frac{\left|P^+(\omega)\right|^2 \left|R(\omega)\right|^2}{2\rho_0 c}. \tag{2.44}$$

From these two quantities, the absorption coefficient of the surface can be obtained:

$$\alpha = \frac{I_{abs}}{I_{inc}} = \frac{I_{inc} - I_{ref}}{I_{inc}} = 1 - \left|R(\omega)\right|^2. \tag{2.45}$$

Therefore, if the normal impedance to the surface is known to be $Z = \rho_0 c\ (z_r + iz_i)$, the absorption coefficient can be computed using equation 2.42:

$$\alpha(\omega) = \frac{4z_r(\omega)}{(1 + z_r(\omega))^2 + z_i^2(\omega)}. \tag{2.46}$$

In this case, the noise absorption is maximum when the imaginary part of the reduced impedance at the surface is zero. For a wave with an oblique incidence, the development is similar to the one presented here and the absorption coefficient is

$$\alpha(\omega) = \frac{4z_r(\omega)\ \cos\ \theta}{(1 + z_r(\omega)\ \cos\ \theta)^2 + z_i^2(\omega)\ \cos^2\ \theta} \tag{2.47}$$

where θ is the angle of incidence.

Chapter 3

Preliminary study

This chapter aims to introduce the concept of resonance by studying a simple geometry in a case of pure acoustic propagation, without mean flow. The study case allows to introduce the physics of the problem and the influence of the numerical set-up.

3.1 Study case

The case of a complex geometry as a hair dryer is simplified through the analysis of a cylinder with thickness. The dimensions of the circular duct are chosen to be similar to those of a complex dryer geometry provided by BaByliss studied further in this chapter *i.e.* an internal radius R of 15.5 mm, a thickness t of 12 mm and a length l of 200 mm as depicted in figure 3.1. The propagation of a spherical source placed at z=170 mm of the duct entrance is studied in the frequency range $[0; 20\,000]$ Hz.

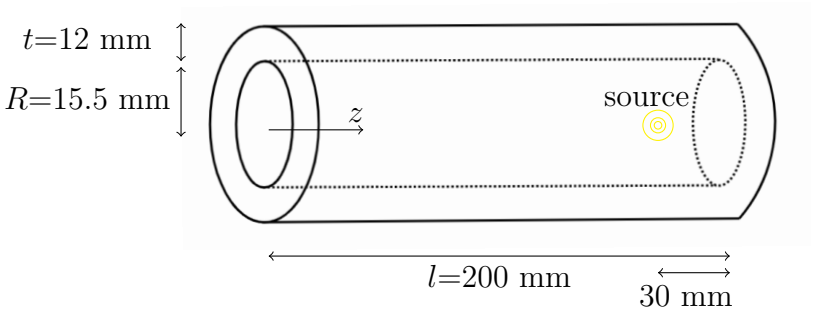

Figure 3.1: Dimensions and position of the point source in the studied geometry.

In order to tame the global geometry as well as the software, this preliminary step focuses on comparing the resonance frequencies derived from the duct theories and the numerical ones produced by the calibration of the ACTRAN study. The comparison of the system eigenfrequencies is realised through the analysis and interpretation of the frequency spectrum. It is therefore essential to first correctly understand the concept of acoustic resonance.

3.2 Resonance

In each constrained medium, rigid boundaries impose that, in absence of an external sound source, the pressure waves existing in the natural state in the medium can only have discrete and fixed wave numbers and frequencies that depend on the medium dimensions. As a matter of fact, the particles velocity being zero at each boundary surfaces, a zero pressure gradient is imposed at those specific points creating a condition on the existing frequencies in equation 2.21. These frequencies are named eigenfrequencies or natural frequencies. Furthermore, the particular wave shapes taken under these frequencies are called modes or shape functions. Altogether, those modes form a base from which any solution can be reconstructed.

If a continuous external source is applied in the constrained medium, the approach of the driving source frequency to one of the natural frequencies of the system causes its particles to oscillate with relatively large amplitudes. This phenomenon is called resonance. More generally, resonance can appear at all frequencies depending on the type of excitation and geometry and characterises a state at which the system starts to vibrate with high amplitude. Usually, this phenomena must be avoided since in this case, higher pressure fluctuations lead to a higher sound pressure level at this frequency, creating more noise.

3.3 Analytical solution

From linearity principle, the dynamic response of each system can be approximated by a combination of its eigenmodes. Considering the z-axis as the principal axis of the cylinder, the general solution of the acoustic wave inside a duct can take the following form:

$$P(r,\theta,z) = \sum_{mn} A_{mn}\ \phi_{mn}(r,\theta)\ e^{ik_{z,mn}z}, \tag{3.1}$$

$$\phi_{mn}(r,\theta) = J_n(r;k_{z,mn})\ e^{in\theta} \tag{3.2}$$

where A_{mn} and ϕ_{mn} are respectively the amplitude and the mode shape of mode (m,n) and $e^{ik_{z,mn}z}$ represents the variation along the duct axis, $k_{z,mn}$ being the axial wave number. J_n is the Bessel function presented in appendix B.

Considering the propagation of only one mode, an individual solution of the Helmholtz equation is obtained by inserting the form presented in equation 3.1 into equation 2.20. The development is presented in appendix B and leads to

$$p_{mn}(r,\theta,z) = J_n(\kappa_{mn}r)e^{in\theta}e^{ik_{z,mn}z} \tag{3.3}$$

where $\kappa_{mn} = \sqrt{k^2 - k_{z,mn}^2}$. At a fixed z, angular travelling waves of the form $p \propto e^{in\theta}$ are obtained while at fixed θ, $p \propto e^{ik_{z,mn}z}$ and transversal travelling waves are observed. The global solution of a given mode is therefore the combination of a spinning travelling wave and an axial one.

Solution 3.3 respects the boundary condition imposed by the rigid wall at $r = R$ only if the acoustic velocity is zero at the wall:

$$J'_n(\kappa_{mn}R) = 0, \tag{3.4}$$

i.e. if, considering ξ_{mn} as the mth-zero of the function J'_n,

$$\kappa_{mn}R = \xi_{mn} \Rightarrow k_{z,mn} = \sqrt{k^2 - \left(\frac{\xi_{mn}}{R}\right)^2}. \tag{3.5}$$

From equation 3.5, two cases can occur:

- either $f < f_{nm} \doteq c\xi_{mn}/(2\pi R)$ and $k_{z,mn}$ is imaginary, the angular mode is evanescent and said to be "cut-off";
- or $f \geqslant f_{nm}$ and the mode corresponding to the pressure distribution $J_n(\xi_{mn}\frac{r}{R})e^{in\theta}$ propagates along the z-axis of the duct without attenuation and with a wave number $k_{z,mn}$, the mode is "cut-on".

It is important to highlight that the plane wave mode corresponds to $m = n = 0$, and thus to a zero cut-off frequency $f_{00} = 0$ Hz. Therefore, plane waves propagate at all frequencies. At higher frequencies however, other modes can be propagated. Cut-off frequencies existing in the audible range for the present study case are listed in table 3.1. Bellow 6 427.89 Hz, only plane waves propagate. The frequency range [0;6 427.89] Hz can then be studied with the simple plane wave theory to deduce the natural frequencies of the geometry.

m \ n	0	1	2	3	4
1	13 377.00	6 427.89	10 662.64	14 666.98	18 564.14
2	-	18 612.67	-	-	-

Table 3.1: Cut-off frequencies f_{mn} [Hz] of mode (m,n) in the audible range for a cylinder of radius $R = 15.5$ mm.

The eigenfrequencies of a rigid tube open on both ends can be obtained by imposing the pressure to be zero at both extremities through the plane wave theory presented previously. The boundary conditions are:

$$\begin{cases} P(z=0) = 0 \\ P(z=l) = 0 \end{cases} \overset{eq.\ 2.21}{\Rightarrow} \begin{array}{l} P^+ + P^- = 0, \\ P^+e^{-ikl} + P^-e^{ikl} = 0. \end{array} \tag{3.6}$$

A non trivial solution is obtained for:

$$P^+ = -P^- \text{ and } \sin(kl) = 0 \Leftrightarrow kl = n\pi \Leftrightarrow f_n = \frac{nc}{2l}. \tag{3.7}$$

where f_n is the nth harmonic resonance frequency of the open tube, n being an integer. Resonance can then occur when the length l of the tube is an integer multiple of the half excitation wavelength as shown in figure 3.2 and listed in table 3.2 (first line).

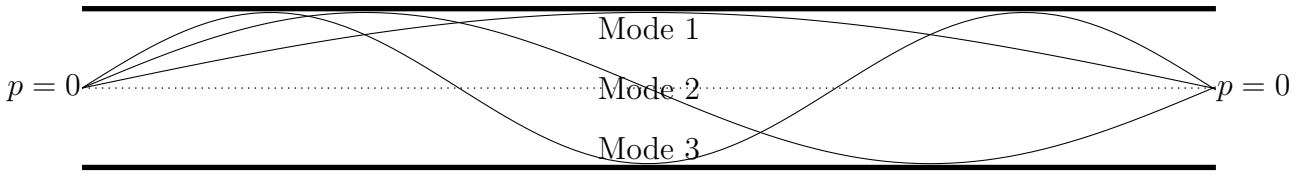

Figure 3.2: Pressure distribution of the first three eigenmodes of an open-open tube.

However, some reflection occurs at the extremities of the open tube due to a difference of impedance created by what is called a radiation impedance. It means that some part of the wave energy is actually sent back inside the cylinder, even at an open end. The theoretical resonance frequencies (cf. equation 3.7) can therefore be improved by a length correction. For such a case of cylinder with thickness, the correction Δl (to add to l in equation 3.7) accounts for about $0.75 \cdot R$, *i.e.* a coefficient in between those computed for the extreme cases: 0.6133 for a pipe without thickness and 0.8216 for an infinite flange [9].

The natural frequencies of the plane wave mode of propagation are listed in table 3.2. These analytical results will further be compared to the numerical ones. At frequencies higher than 6427.89 Hz, as mentioned, other transverse modes are propagating and the resonating state of the tube becomes too complex to analyse.

n	1	2	3	4	5	6	7	8
f_n [Hz] uncorrected	850	1 700	2 550	3 400	4 250	5 100	5 950	6 800
f_n [Hz] Δl correction	803.3	1 606.6	2 409.9	3 213.2	4 016.5	4 819.8	5 623.2	6 426.5

Table 3.2: Plane wave uncorrected and corrected resonance frequencies f_n for a cylinder of length $l = 200$ mm and radius $R = 15.5$ mm.

3.4 Numerical solution

The frequency spectrum can be numerically obtained in order to visualise the peaks created by the resonance phenomenon and to compare the resonance frequencies to those analytically computed in table 3.2. To do so, the numerical set-up is described and then adjusted to ensure the convergence of the results. The total spectrum is then presented. Finally, the influence of parameters such as the boundary conditions, the position of the source or the geometry shape on the final result is shown.

3.4.1 Basic set-up

3.4.1.1 Geometry

A cylinder of length l=200 mm, internal radius R=15.5 mm and external radius 27.5 mm is created. Additionally, an ellipsoid surface is created around the cylinder; it represents the delimitation of the studied domain, parameter deepened later. A volume can then be defined between the cylinder surfaces and the ellipsoid as depicted in figure 3.3. The dimensions as well as the mesh of this external 3D domain influence a lot the quality of the results, these points are dealt with in section 3.4.2.

3.4.1.2 Components

In this simple analysis, only one 3D acoustic component is defined: a finite fluid component. The 3D finite fluid acoustic component is simply used to model finite acoustic media and encompasses then the whole volume created between the two surfaces. The fluid set is air at rest with the following standard properties:

- speed of sound: 340 m/s,
- fluid density: 1.225 kg/m^{-3},
- damping: 0%.

3.4.1.3 Boundary conditions

The second component defined in ACTRAN is rather a 2D boundary condition and is imposed on the ellipsoid surface delimiting the 3D domain. This component is called infinite elements. It allows to model radiation in free field through a non-reflecting boundary condition. The pressure at points located outside the domain, at a distance r from the source, can then be computed by a multipole expansion:

$$p(r) = \frac{A_1}{r} + \frac{A_2}{r^2} + \frac{A_3}{r^3} + ...\frac{A_N}{r^N} \tag{3.8}$$

where N is the interpolation order of the component, its value is detailed further. The domain chosen to study a cylinder is an ellipsoid denoted by "*a*-*b*-*c*" where *a, b* and *c* are the ellipsoid's axes length in the x, y and z directions.

After the specification of the ellipsoid boundary condition through infinite fluid elements, it remains to impose the cylinder walls to be rigid. This boundary condition is set by default in ACTRAN on any surface for which no boundary condition is specified and numerically sets the velocity to be zero on those surfaces.

3.4.1.4 Acoustic excitation

In addition to this, a point source is defined as mentioned on the principal axis of the cylinder at z=170 m and generates an incident pressure field at a distance r of the source equal to

$$p = A\frac{e^{-ikr}}{r} \tag{3.9}$$

where A is the amplitude set to 1 Pa·m and k is the wave number. This source is represented in yellow in figure 3.3.

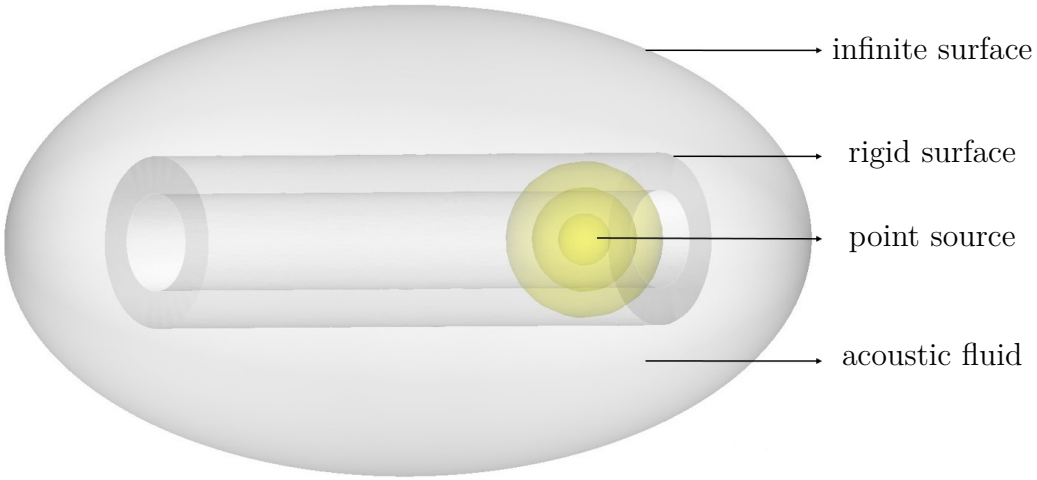

Figure 3.3: Set-up created in ACTRAN showing the components, the boundary conditions and the excitation.

3.4.1.5 Post-processing

Two main types of post-processing are implemented in this preliminary case: a field point and an output map.

The field point is defined by a set of points that act as virtual microphones, specific quantities such as the pressure can therefore be obtained at these points. The infinite surface defined previously allows them to be outside the finite element domain. Two important points are specified here: one in the middle of the cylinder at z=100 mm and one outside the domain located arbitrarily on the cylinder principal axis at z=-200 mm, *i.e.* at 20 cm of the extremity of the cylinder. These two are necessary for the convergence studied.

In addition to this, the output map allows to visualise the computed fields (acoustic pressure and velocity) in the whole domain for a specified frequency. In this case, the 3D acoustic component is selected.

3.4.2 Convergence studies

Convergences studies have been led with the set-up previously specified on the mesh elements size and on the surface of infinite elements (size and interpolation order) to ensure the convergence of results.

3.4.2.1 Mesh

The surface and volume meshes are respectively triangular and tetrahedral homogeneous meshes with linear interpolation. A rule a thumb is to use at least 8 elements per wavelength to capture correctly the acoustic oscillations (cf. figure 3.4). As the direct frequency response is computed from 0 to 20 000 Hz, the required maximum element size is 2.125 mm.

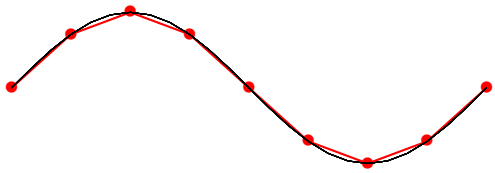

Figure 3.4: Decomposition of a sinus in 8 linear elements.

Mainly three mesh sizes have been tested: 1.5, 1.7 and 2.1 mm for low and high frequency ranges [500;2 500] Hz and [12 500;14 500] Hz. To quantify correctly the convergence of the mesh, the results are presented in figures 3.5a and 3.5b for a microphone positioned inside the domain, in the middle of the cylinder. In these three cases, the infinite surface domain considered is an ellipsoid of size 20-20-35 [cm]. It is necessary to highlight the fact that the following analysis would have been more solid if the mesh size step had been constant since, here, the variation is first 0.4 mm and then 0.2 mm.

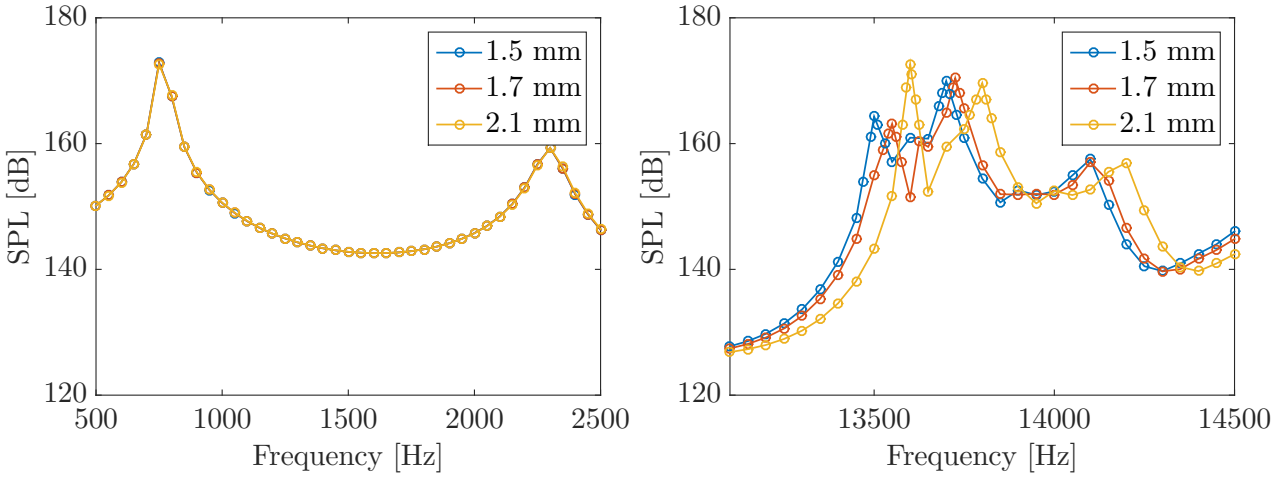

(a) Low frequencies.

(b) High frequencies.

Figure 3.5: SPL as a function of the frequency for three different mesh element sizes at a microphone placed in the middle of the cylinder.

Furthermore, the cost of the different simulations can be evaluated through the time and the memory needed to calculate each frequency. These are listed in table 3.3. Each case has been run on 32 processors in multi-threading. The comparison is also done regarding the

amplitude of the first notable peak in figure 3.5b for which the frequency step as been refined in other to obtain a consistent comparison.

El. size [mm]	Nb el. [-]	Time [min]	Mem. [MB]	1^{st} peak coord.
1.5	21 485 238	55	352 124	(13 520;164.31)
1.7	14 774 102	22	221 287	(13 545;163.16)
2.1	7 875 655	8	102 807	(13 610;172.66)

Table 3.3: Number of elements obtained, simulation time needed (per frequency), memory necessary (per frequency) and coordinates of the first peak in figure 3.5b for three element sizes.

It can easily be observed that the size of the mesh does not have a big impact at low frequencies as expected since the wavelength to capture is larger. However, at higher frequencies, the differences are significant and must be analysed.

What is important in the present chapter regarding the quality of the mesh is to correctly capture the peak frequencies in order to compare them with the analytical solution. In chapter 5 presenting solutions for attenuating the noise, this is mainly the modification of peaks amplitude that will take its importance. However, if the cases with and without attenuation system are compared based on the same mesh and interpolation order, the analysis is judged consistent since the numerical bias is similar in both cases.

From table 3.3, it can be seen that refining the mesh from 2.1 to 1.7 mm leads to a relative modification in the SPL amplitude and peak frequency of respectively 5.5% and 0.47% at the cost of an increase in required time and memory of about respectively 175% and 115%. Additionally, the mesh with an elements size of 1.5 mm allows to gain only 0.7% and 0.18% of amplitude and frequency precision against a simulation time once again doubled. The memory required for this type of computation is also very important, leading to out-of-core much longer computations. For these reasons, it has been decided to build all the further set-ups with a mesh of element length of 1.7 mm judged enough to lead a consistent study but reasonable in term of the time and memory required.

3.4.2.2 Infinite surface

Once the convergence of points inside the domain is reached, the size of the domain and the interpolation order must be investigated to make sure that results obtained outside the domain are also correct. An important point to mention is the fact that the optimal infinite domain size and interpolation order are not independent. If the domain is small, the solution outside of this one cannot be approximated by a low interpolation order. Inversely, if a low interpolation order is used, the outer sound field is well approximated only for a larger domain [42]. In addition to this, it must be kept in mind that the complexity of the radiation

field and thus of the source plays a role in the interpolation order required for convergence. In this case, it has been decided to study the domain size with an interpolation order of 10.

The results at a microphone placed 20 cm before the cylinder are firstly displayed in figure 3.6 and table 3.4 for four ellipsoids. For a converged mesh, it can be observed that each ellipsoid present peaks with the same amplitude and at the same frequencies without major differences. In order to save resources, the smaller ellipsoid is selected.

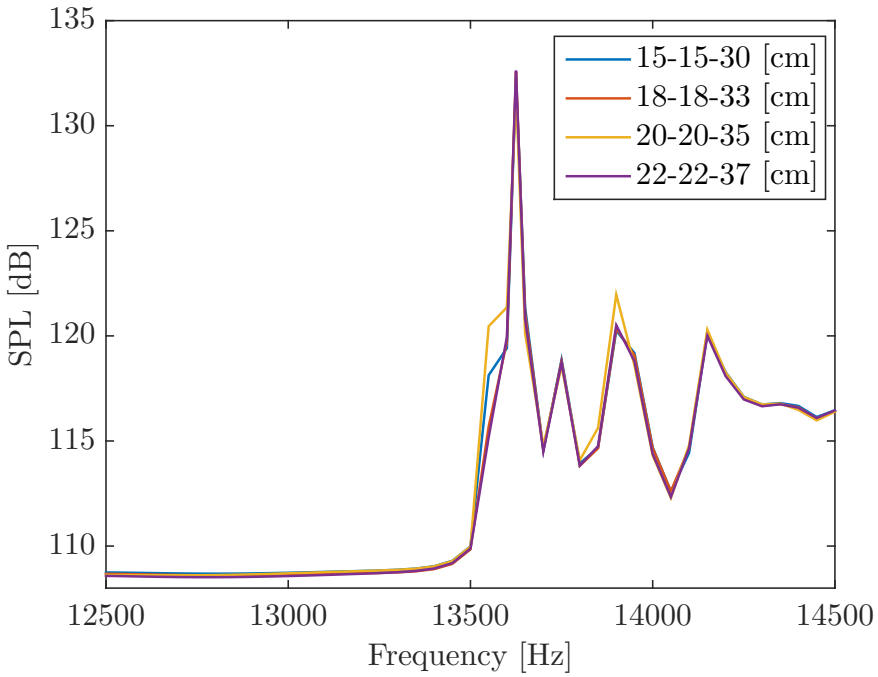

Figure 3.6: SPL as a function of the frequency for four different ellipsoids at a microphone placed at 20 cm of the cylinder extremity for a mesh of 1.7 mm.

Ellips. axes [cm]	Nb el. [-]	Time [min]	Mem. [MB]
15-15-30	6 458 075	3.2	78 333
18-18-33	10 745 882	12.1	148 903
20-20-35	14 774 102	22.3	221 287
22-22-37	18 681 754	43.4	310 694

Table 3.4: Number of elements obtained, simulation time needed (per frequency) and memory necessary (per frequency) for four ellipsoid sizes.

Finally, the interpolation order of the multipole expansion used to determine the pressure outside the domain can be studied. The SPL and the numerical resources needed for the

set-up with three different values are displayed in figure 3.7 and table 3.5. Once again, mainly for the sake of saving time, the smaller interpolation order *i.e.* 6 is chosen to be enough to catch correctly the position of the peaks in the context of a preliminary study. Moreover, an interpolation order of 4 has not been tested due to the difference appearing between the curves for 6 and 8.

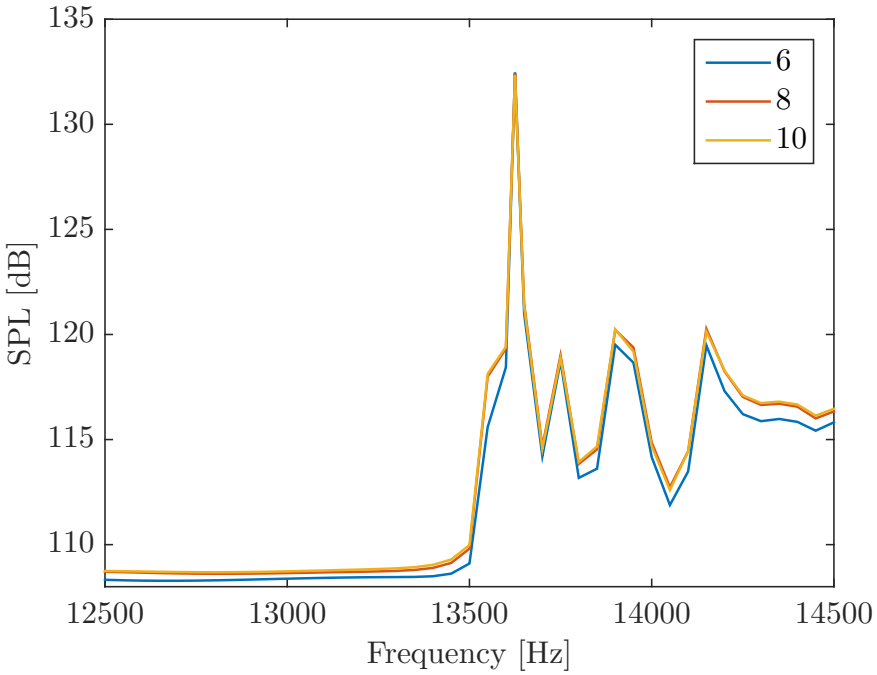

Figure 3.7: SPL as a function of the frequency for three different interpolation orders at a microphone placed at 20 cm of the cylinder extremity for a mesh of 1.7 mm and an ellipsoid of size 15-15-30 [cm].

Interpol. order [-]	Time [s]	Mem. [MB]
6	96	59 354
8	126	68 247
10	192	78 333

Table 3.5: Simulation time needed (per frequency) and memory necessary (per frequency) for three interpolation orders.

The conclusions of those convergence analysis lead to a mesh of size 1.7 mm inside an ellipsoid shaped domain of size 15-15-30 [cm] with an interpolation order of 6 used on the infinite elements. The resulting meshed acoustic domain is displayed in figure 3.8.

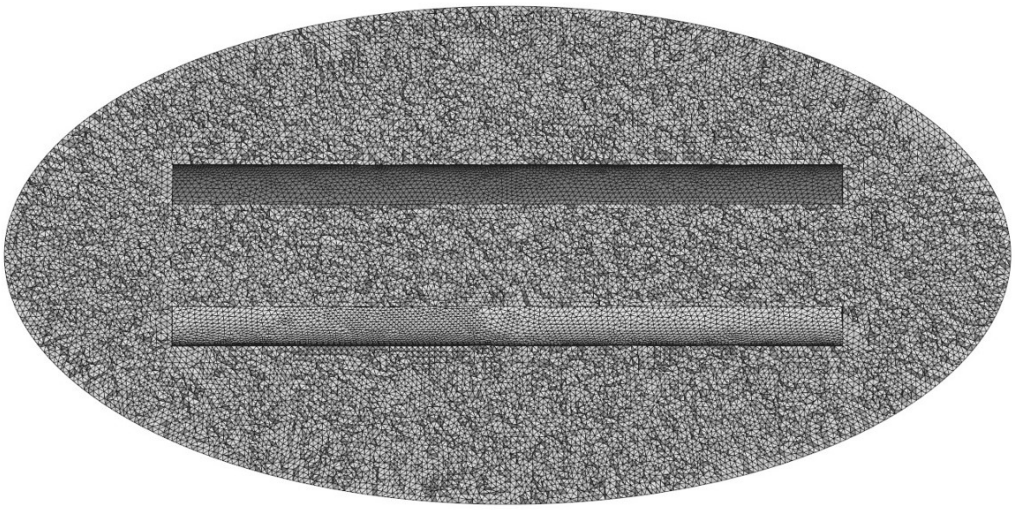

Figure 3.8: Visualisation of the final mesh for a cutting plane perpendicular to the z-axis obtained in ACTRAN.

3.4.3 Results

The spectrum of the mean acoustic pressure in the domain obtained by the propagation of the point source is displayed in figure 3.9. The resonance frequencies of plane waves propagation are well marked below f_{11}=6 427.89 Hz. However, the peaks are positioned at frequencies multiple of 775 Hz instead of about 800 Hz as derived from the theory (cf. table 3.2).

This small shift can be a consequence of different error sources beside the mesh size as it has no influence at low frequencies. A possible numerical error is the frequency step used in this simulation which is equal to 5 Hz what means that the first peak is in reality located between 770 and 780 Hz.

Errors can also result from the theory used. As a matter of fact, the length correction that tries to deal with the singularities at the duct extremities is an approximation based on an interpolation between two extreme values. The next subsection presents thus an other boundary condition to see the effect of this termination. Additionally, it is important to signal that the modal expansion can be done on propagating modes, neglecting those evanescent, only far from singularities linked to the geometry or an existing source. The theory presented above is therefore not completely in agreement with the case simulated.

Moreover, the quasi-silence zone between 6 000 Hz and 13 000 Hz is not theoretically predicted as some other modes should start to propagate from 6 427 Hz and should then be more marked, as at 13 000 Hz. It is assumed that, as the point source is positioned exactly on the cylinder principal axis, the angular asymmetric modes can not propagate correctly

due to a blockage from the geometry. This hypothesis is verified in the following section with an additional test.

It is important to mention that this case is highly theoretical. In practice, a SPL of 160 dB is never reached but it is the level obtained in this work since the amplitude of the source is arbitrarily imposed to be equal to 1 Pa·m. Additionally, an excitation is never perfectly imposed at one precise point as on the cylinder axis so the result obtained would never be achieved in a practical case.

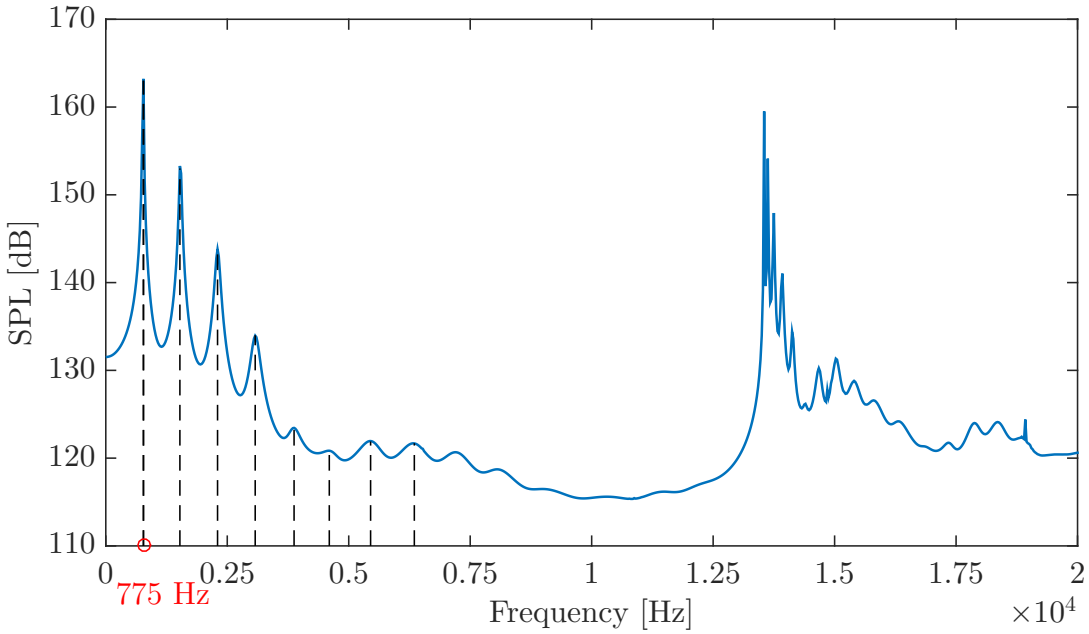

Figure 3.9: SPL based on the mean acoustic pressure as a function of the frequency with infinite elements boundary condition.

Furthermore, the output maps can be visualised through two cutting planes in order to see the different transverse patterns (cutting plane perpendicular to the z-axis) and the plane waves eigenmodes (cutting plane parallel to the z-axis).

Figure 3.10 shows the pressure distribution patterns of the first four cut-on modes. The scales have not been specified since they have been adapted in order to visualise the shapes. Mode (0,0) represents the classical plane wave with the pressure constant through any plane perpendicular to the propagation axis. Mode (1,0) is highly marked and is dominant even at higher frequencies. The other modes are therefore not visible even above 15 000 Hz.

Moreover, figure 3.11 displays the sound pressure level output map for the natural frequency 775 Hz and its first three harmonics. On those figures, the nodes *i.e.* the points at which the air pressure variation is zero and the anti-nodes are very visible. The results are in accordance with figure 3.2.

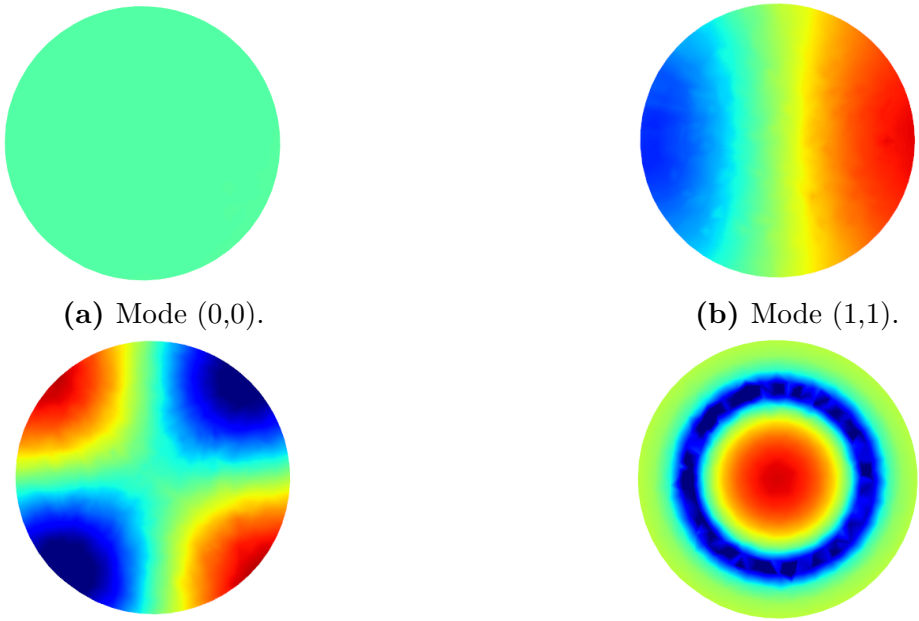

(a) Mode (0,0). **(b)** Mode (1,1). **(c)** Mode (1,2). **(d)** Mode (1,0).

Figure 3.10: Sound pressure level pattern of the transversal modes.

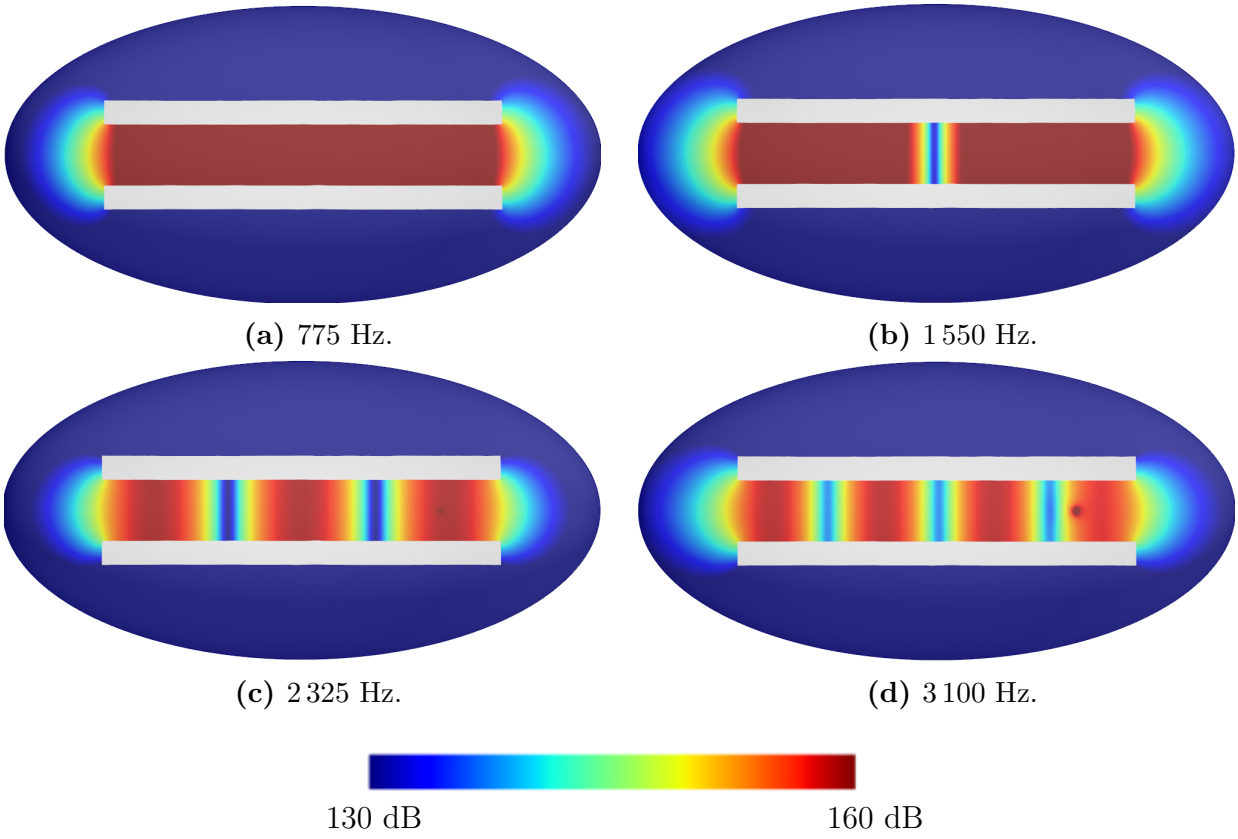

(a) 775 Hz. **(b)** 1 550 Hz. **(c)** 2 325 Hz. **(d)** 3 100 Hz.

Figure 3.11: Sound pressure level output maps at the first four resonance frequencies.

3.4.4 Influence studies

In order to better understand the frequency spectrum obtained, an other boundary condition replacing the infinite fluid component is tested. The point source is also shifted to see the influence of the source location on the results. Additionally, the influence of the external casing shape is presented.

3.4.4.1 Non-reflecting boundary condition

Instead of an ellipsoidal domain with infinite elements, a non reflecting boundary condition can be applied on the extremities of the cylinder. This boundary simply imposes anechoic condition on the two disks closing the tube and has been tested to try to fit the analytical solution better. In this case, the termination impedance should not be taken into account since there is absolutely no reflection due to the discontinuity at both ends. In this case, the simple formula of equation 3.7 is of application and this is clearly illustrated in figure 3.12 where the peaks are located at $f_{n=1} = 850$ Hz and its harmonics. The SPL amplitude is not comparable to figure 3.9 since the mean is not derived on the same domain.

This simulation shows explicitly that the shift obtained in the previous case is mainly due to the singularities at the open ends. However, the present case is rather a theoretical set-up to validate the hypothesis made on the error previously and does not correctly represent the reality.

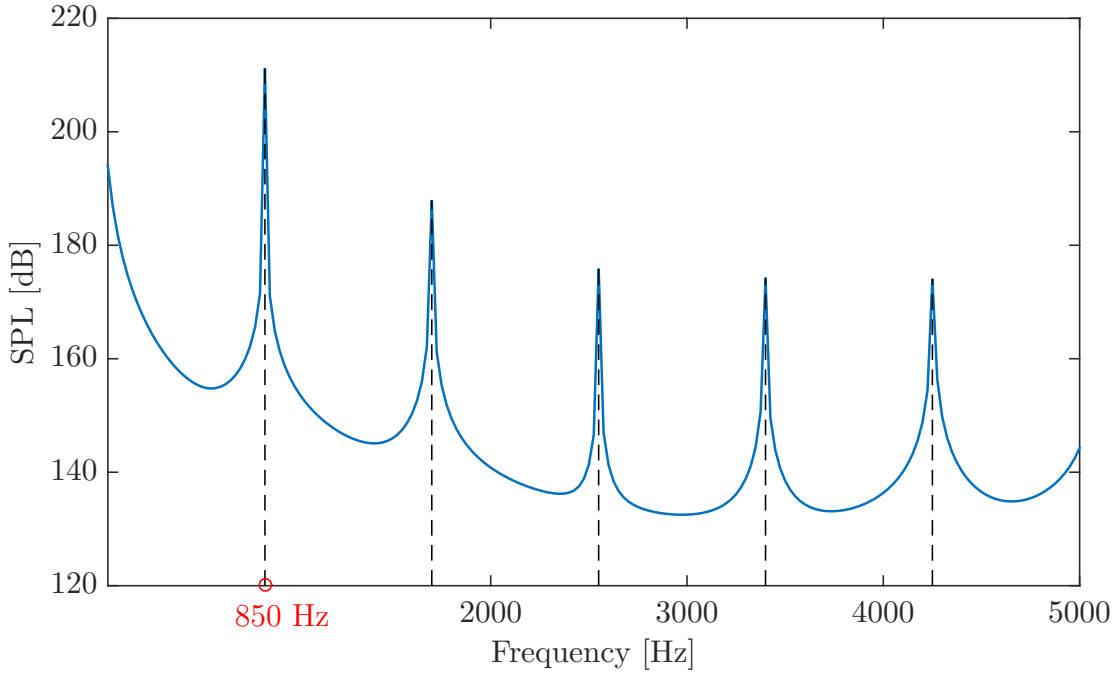

Figure 3.12: SPL based on the mean acoustic pressure as a function of the frequency with non-reflecting surfaces boundary condition.

3.4.4.2 Source position

As mentioned, the frequency spectrum obtained presents a suspicious zone between 6 000 Hz and 13 000 Hz. It has then been decided to test an identical set-up with the source also positioned at z=170 mm but shifted from the principal axis of 10 mm. The case has only been simulated from 5 000 Hz to 13 000 Hz in order to gain time.

The result is displayed in figure 3.13. From this, it can easily be understood that the centred source cancels or strongly damps the propagation of modes that do not present an angular symmetry. As a matter of fact, the peaks present around 6 500 Hz and 11 000 Hz clearly show now the cut on of modes (1,1) and (1,2).

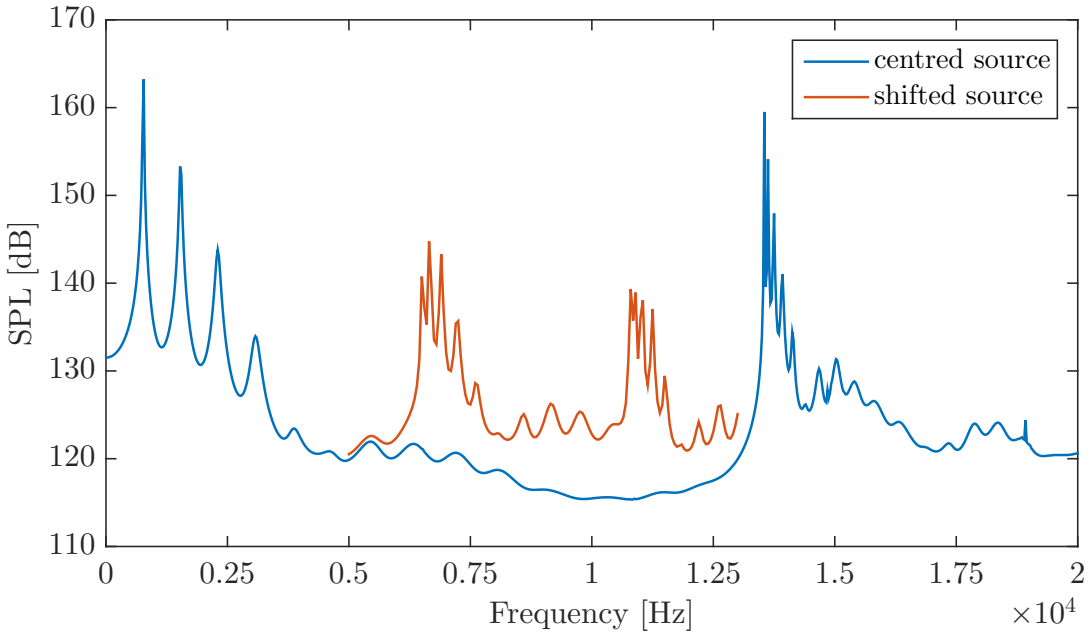

Figure 3.13: SPL based on the mean acoustic pressure as a function of the frequency for the centred and shifted source cases with infinite elements boundary condition.

3.4.4.3 Complex geometry

To conclude the preliminary study, the spectrum of the propagation inside a cylinder has been compared to the one in a more complex geometry of a hair dryer. The casing used has the same general dimensions as the duct and is presented in figure 3.14. It is composed of an inner empty casing and a protection grid at the end of the tube. The handle has been retrieved to simplify the geometry.

The set-up created with this geometry is the same as the one presented in section 3.4.1 except for one particularity: the geometry being more complex, the surface mesh of the casing has been set to 1 mm instead of 1.7 mm for the quality of the interfaces between the different parts. However, the total volume mesh has a mean edge length of 1.7 mm.

The mean sound pressure level over all the audible frequencies are compared to the simple cylinder case in figure 3.15. It can be observed that the additional complexity of the casing does not impact significantly the position of the peaks in the spectrum. Therefore, it has been decided to realise all the studies in the next chapters on the simple cylinder geometry only.

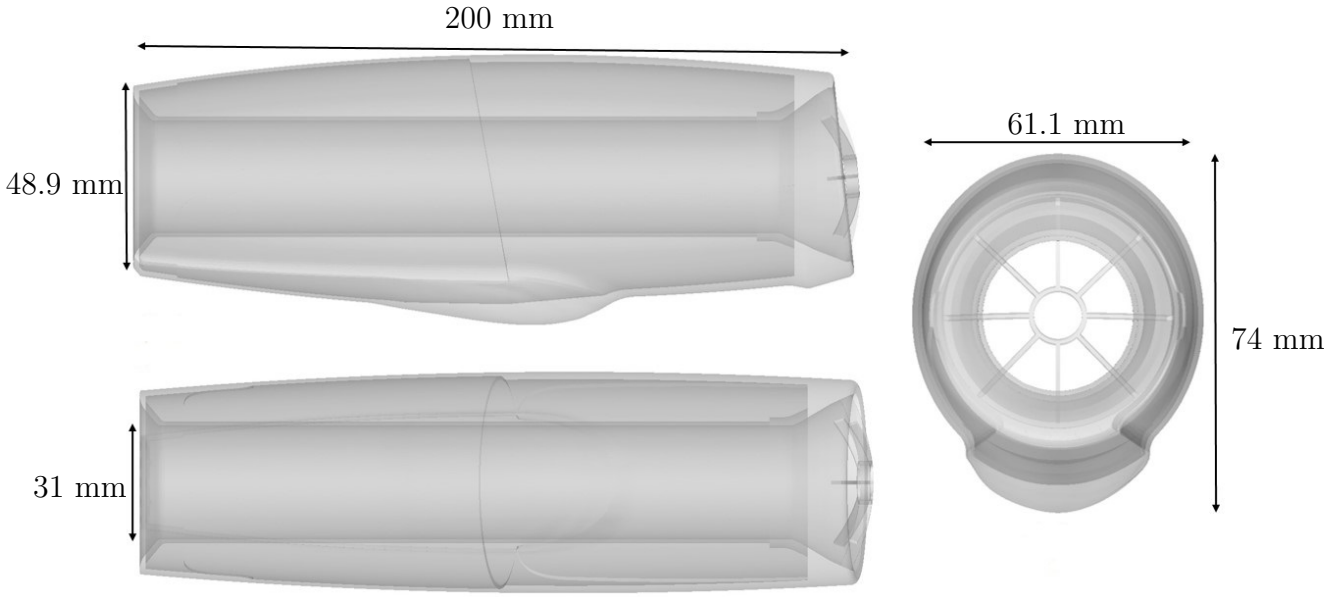

Figure 3.14: Simplified hair dryer geometry.

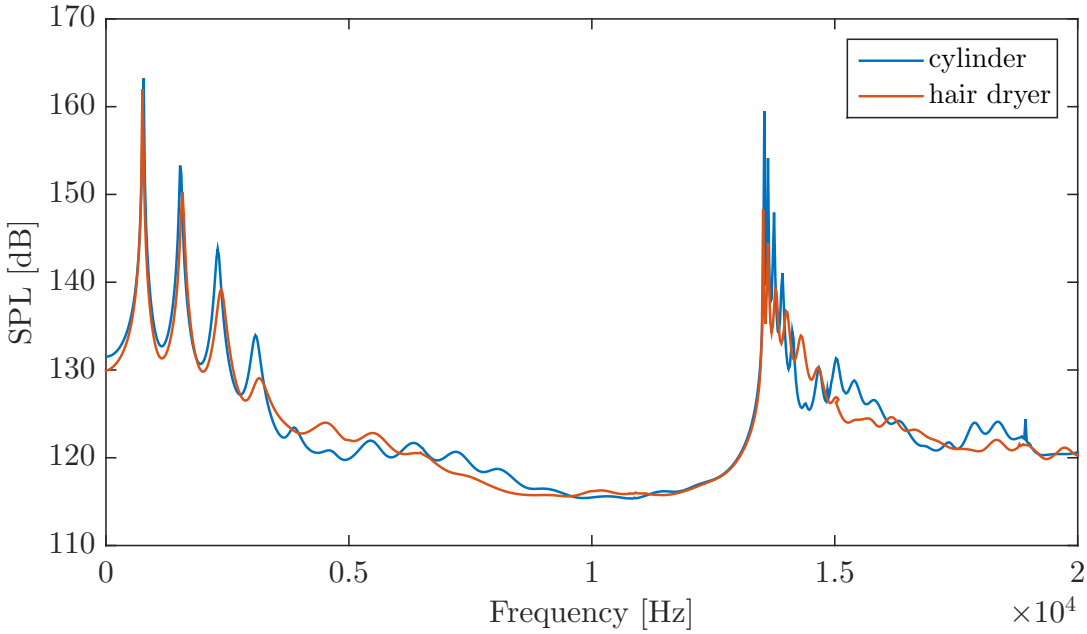

Figure 3.15: SPL based on the mean acoustic pressure as a function of the frequency for the simple and complex geometries with infinite elements boundary condition.

Chapter 4

Aero-acoustic sources

The point source imposed until now allows to easily excite all the frequencies and to highlight the classical duct modes in a purely acoustic study case. However, the noise generated by a device such as a hair dryer is typically due to the fan engine. The different sources of fan noise are thus first presented on the basis of a literature review. Then, Lighthill aero-acoustic analogy, an approach built to deal with flow-induced noise, is theoretically detailed and numerically implemented to deal with these specific sources.

4.1 Fan noise

Fan noise can be divided into two categories: mechanical and aerodynamic noises. Mechanical noise is created by structural vibrations; these vibro-acoustic sources manifest themselves as broadband noise. Some tonal noise at harmonics of the rotor rotation speed frequency can also appear in practical cases due to imperfect blade machining creating an unbalanced effect. Since the vibro-acoustic analysis of the engine is a study in its own right, the vibro-acoustic sources are considered as outside the scope of this project.

Additionally, flow-induced noise is mainly generated by three contributions listed bellow [21]. The monopole, dipole or quadrupole character of the sources is also specified according to Ffowcs and Hawkings extension of Lighthill analogy presented next [12].

- The mass fluctuation generated by the volume displacement of the rotor blades generates what is called thickness noise since it is linked to the volume of air displaced by the rotation and thus to the blade thickness. It can be seen as a surface distribution of monopole sources.
- Loading noise, characterised by a dipole distribution, can be divided into two categories: the steady loading noise which is constant in time for a reference placed on the rotating blade and the unsteady source which is time dependant to an observer in the rotating frame. Steady loading noise is created by the aerodynamic pressure acting on the blades solid boundaries. It is the propagation of the rotating pressure disturbance. Unsteady

loading noise is due to the variation of blade loading in each revolution. Typically, the presence of the stator disturbs the rotating periodic pressure field of the rotor. This rotor-stator interaction is the most important source of noise in the present case [48].

- Random flow variations caused by turbulence and distributed throughout the volume exterior to boundaries create a broadband noise component. Turbulence provides a quadrupole distribution.

The first two types come out as a tonal noise at the blade passing frequency (BPF) computed as the number of blades multiplied by the rotation velocity expressed in RPM divided by 60. An impulsive force fluctuation indeed results from air impulses created each time a blade crosses a specific point. In subsonic regime, the main contribution is dipole and thus the most noisy frequency, the problematic one, is the BPF.

4.2 Lighthill analogy

The most direct and complete approach to study aero-acoustics consists in resolving the compressible Navier-Stokes equations through a direct numerical simulation (DNS). The solution automatically accounts for sound generation and propagation. However, in such a case, the grid size should be able to capture the smallest fluctuations at the turbulence length scale and the time resolution should be determined by the fastest oscillation linked to acoustics phenomena. It results then "the worst of both worlds". Engineering problems cannot be solved with such high computational and memory costs and require therefore new procedures.

Rather than studying the mechanisms of complex flow fluctuations generating noise, the principle of the analogy described by Lighthill in 1952 is the decoupling of the noise generation and its propagation [27]. To do so, the fluid is seen as a uniform acoustic medium at rest on which an external fluctuating force is applied. The effect of this field force is obtained by comparing the equations for sound propagation in a uniform medium at rest to the exact governing equations of motion of a fluid. This hybrid approach is valid only for low Mach number flows (below 0.2) since the flow field is implicitly replaced by different types of sources. In this method, the coupling is done only in one way; it means that the acoustic waves have no feedback effect on the mean flow. In practice, this also means that Lighthill analogy can be used only for flows where the convection and refraction effects on acoustic propagation are negligible.

The general equations for the motion of a fluid are

$$\begin{cases} \frac{\partial}{\partial t}(\rho - \rho_0) + \frac{\partial}{\partial x_i}(\rho v_i) = 0 \\ \frac{\partial}{\partial t}(\rho v_i) + \frac{\partial}{\partial x_j}(\rho v_i v_j) = -\frac{\partial p_{ij}}{\partial x_j} \end{cases} \tag{4.1}$$

where the first equation is the continuity equation written in a slightly modified form introducing ρ_0, the constant fluid density, and the second one is Reynolds version of the momentum equation. In these formulations, ρ is the fluid density, $\underline{v}$ is the fluid velocity vector and p_{ij} is

the compressive stress tensor defined as

$$p_{ij} = p\delta_{ij} - \tau_{ij}, \tag{4.2}$$

p and τ_{ij} being the fluid pressure and the viscous stress tensor. By combining these two, it is found that

$$\frac{\partial^2}{\partial t^2}(\rho - \rho_0) = \frac{\partial^2}{\partial x_i \partial x_j}(\rho v_i v_j + p_{ij}). \tag{4.3}$$

And adding the same term on both sides, it gives

$$\frac{\partial^2}{\partial t^2}(\rho - \rho_0) - a_0^2 \nabla^2(\rho - \rho_0) = \frac{\partial^2}{\partial x_i \partial x_j} T_{ij} \tag{4.4}$$

where a_0 is the speed of sound in a uniform medium at rest $a_0 = c$ and T_{ij} is defined as the Lighthill stress tensor:

$$T_{ij} = \rho v_i v_j + (p - p_0)\delta_{ij} - c^2(\rho - \rho_0)\delta_{ij} - \tau_{ij} \tag{4.5}$$

where the constant pressure p_0 is added for convenience. Lighthill analogy is thus an exact reformulation of the fluid dynamic equations. The left hand side of equation 4.4 represents the wave propagation operator and the right hand side is the equivalent acoustic source due to the flow applied in the region of noise radiation.

Some hypothesis can however be done at low Mach numbers only on the Lighthill stress tensor term assuming that there is no entropy change $c^2 = (\partial p/\partial \rho)_{\rho=\rho_0}$ and neglecting viscous effects:

$$\frac{\partial T_{ij}}{\partial x_j} = \frac{\partial \rho v_i v_j}{\partial x_j}. \tag{4.6}$$

The harmonic expansion of equation 4.4 gives in the frequency domain:

$$-\omega^2 \tilde{\rho}_a - c^2 \frac{\partial^2 \tilde{\rho}_a}{\partial x_i \partial x_i} = \frac{\partial^2 \tilde{T}_{ij}}{\partial x_i \partial x_j} \tag{4.7}$$

where $\tilde{\rho}_a$ is the acoustic density spectrum according to the notations specific to this section:

$$q(\underline{x}, t) = \sum_{\omega} \tilde{q}(\underline{x}, \omega) e^{i\omega t} = \sum_{\omega} \mathcal{F}(q) e^{i\omega t}. \tag{4.8}$$

A variational formulation of equation 4.7 has been derived by Oberai *et al.* [36]:

$$-\int_\Omega \omega^2 \tilde{\rho}_a \delta\psi d\Omega - \int_\Omega c^2 \frac{\partial^2 \tilde{\rho}_a}{\partial x_i \partial x_i} \delta\psi d\Omega = \int_\Omega \frac{\partial^2 \tilde{T}_{ij}}{\delta x_i \partial x_j} \delta\psi d\Omega \tag{4.9}$$

where $\delta\psi$ is a finite element shape function and Ω is part of the computational domain. This new formulation allows to solve the problem using a finite element method without making further assumptions.

Equation 4.9 can be modified by integrating the spatial derivatives by parts and by applying the momentum equation, leading to:

$$\omega^2 \int_\Omega \tilde{\rho}_a \delta\psi d\Omega - c^2 \int_\Omega \frac{\partial \tilde{\rho}_a}{\partial x_i} \frac{\partial \delta\psi}{\partial x_i} d\Omega \tag{4.10}$$

$$= \int_\Omega \frac{\partial \delta\psi}{\partial x_i} \frac{\partial \tilde{T}_{ij}}{\partial x_i} d\Omega + i\omega \oint_\Gamma \mathcal{F}(\rho_a v_i n_i) \delta\psi d\Gamma. \tag{4.11}$$

In this case, the right hand side is computed by the CFD results (density, pressure and velocity on the CFD mesh) and is mapped and integrated on the coarser acoustic mesh through the shape function. It represents first a volume contribution accounting for the divergence of convective fluxes usually computed in the stator domain for a case of fan noise. The second term is a surface term and in the present work, the surface considered is the rotor-stator interface which is a permeable surface on which all fluctuations are taken into account.

4.3 Numerical implementation

The set-up of a Lighthill analogy using ACTRAN software follows schematic 4.1. Firstly, the computer-aided design (CAD) is build for the whole study. Then, the unsteady fluid dynamics is computed using a CFD software. In parallel, the acoustic mesh is prepared based on the same CAD model. After these preliminary processes, the acoustic sources are extracted from the CFD results and mapped on an acoustic mesh through a CFD interface called ICFD. Finally, these sources are propagated in the acoustic domain using ACTRAN. These different steps are described next in the context of the present work.

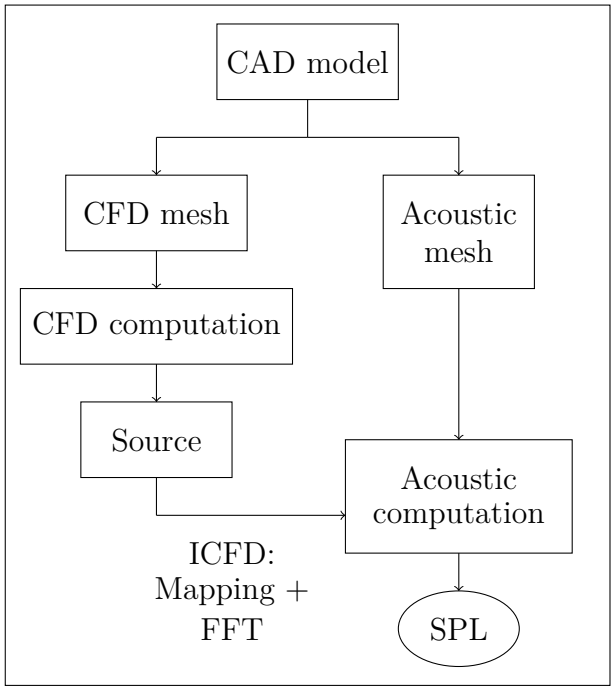

Figure 4.1: ACTRAN process for the computation of aero-acoustic sources [42].

4.3.1 CAD model

The engine fixed in the hair dryer by BaByliss is named *Keli*. It is composed of a rotor made of 13 blades depicted in red in figure 4.2 and a stator with 9 blades. This geometry is common to both CFD and acoustic meshes and is integrated in a cylinder as presented in the preliminary study, centred on z=170 mm.

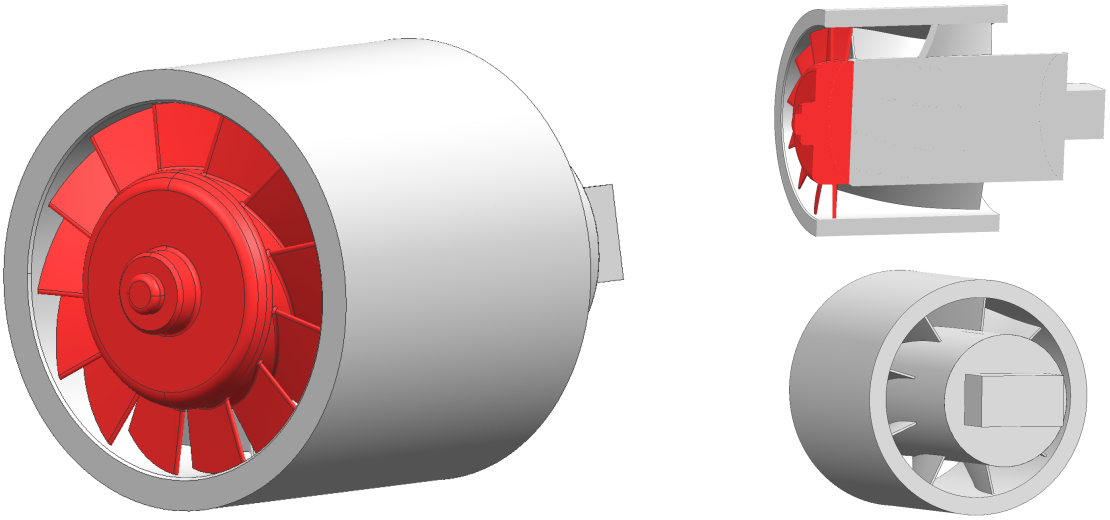

Figure 4.2: Rotor stator geometry of engine *Keli* provided by BaByliss.

The smallest rotation speed, the one used in this work, is 75 000 RPM. In this case, the BPF is equal to 16 250 Hz. But there are also two other rotational positions on this product: 85 200 and 99 600 RPM. Additionally, it is known that the flow rate is equal to 11.82 g/s. It is important to note that the CAD of the stator, depicted in grey, has not been provided by the manufacturer and so it had to be reconstructed by a member of GDTech based on iterations to improve angles and decrease detachment of the flux. This adds an uncertainty on the results compared to the experimental ones.

4.3.2 CFD analysis

The engine has been simulated in the cylinder geometry using StarCCM+. The CFD computation is unsteady, compressible and has been initialised by a stationary frozen rotor simulation without mesh movement. Furthermore, the model of turbulence used is $k-\omega$ SST. The mesh depicted in figure 4.3 is a polyhedral one of average size 0.75 mm. It is divided in a static zone in grey and a rotating one including the rotor in red. No convergence study has been realised on this mesh what could be another source of error in the results.

It is important to note that the CFD analysis has been realised by an other member of GDTech in order to gain time. It has thus been chosen not to show the CFD results since it is considered as out of the scope of the present work.

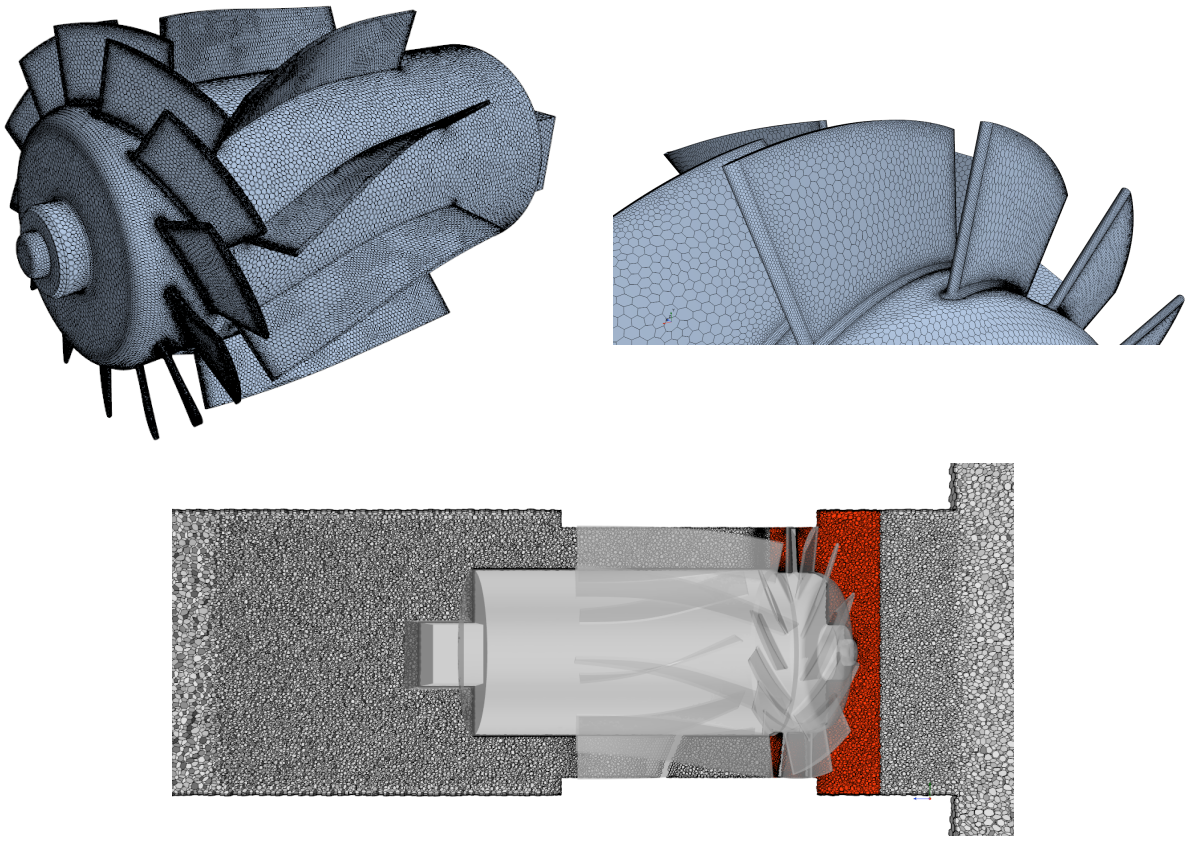

Figure 4.3: Polyhedral mesh of the rotor stator geometry with the rotating mesh in red and static mesh in grey.

The CFD write down time step Δt^{CFD} has to be chosen carefully to respect Nyquist theorem. This one states that for the quality of the sampling and of the time/frequency domain conversion, a sampling frequency at least equal to twice the maximum frequency contained in the signal is required:

$$\frac{1}{\Delta t^{CFD}} > 2 \cdot f_{max}. \tag{4.12}$$

The acoustic results are therefore dependant on the N exported CFD results at the rate Δt^{CFD}. The spectrum indeed ranges from $f_0 = 1/(N\Delta t^{CFD})$ to $f_m = 1/(2\Delta t^{CFD})$ with a frequency step f_0. The values of N and Δt^{CFD} have been chosen equal to 290 and approximately $2.76{\cdot}10^{-5}$ s respectively to obtain a spectrum from 125 to 18 125 Hz with a frequency step of 125 Hz so to sweep and correctly compute all the multiples of the rotation frequency.

4.3.3 Acoustic set-up

The set up of the acoustic propagation is similar to what has been presented in the preliminary study *i.e.* a rigid cylinder surrounded by an acoustic fluid delimited by an infinite surface imposing a free field radiation boundary condition. The only difference is the excitation source. The rotor is indeed suppressed from the geometry and replaced by two Lighthill

boundary surfaces and a Lighthill volume indicated respectively in red and in green in figure 4.4, these boundary conditions are computed through ıCFD described hereafter. The stator geometry is added and required a zone with a thinner mesh having the sole purpose to correctly feel the geometry boundaries.

Figure 4.4: Acoustic set-up with Lighthill surfaces in red and Lighthill volume in green.

The maximum frequency computed being the same, the global mesh size of 1.7 mm is conserved, the same is also true for the size of the ellipsoid. However, as stated in the convergence studies in section 3.4.2, the choice of the infinite fluid surface and of the interpolation order is strongly dependent on the complexity of the acoustic sources present in the domain. Therefore, different interpolation orders have been tested at high frequencies to ensure the convergence of the results with the new source. These are displayed in figure 4.5 for a microphone placed at 20 cm of the hair dryer extremity, for three interpolation orders.

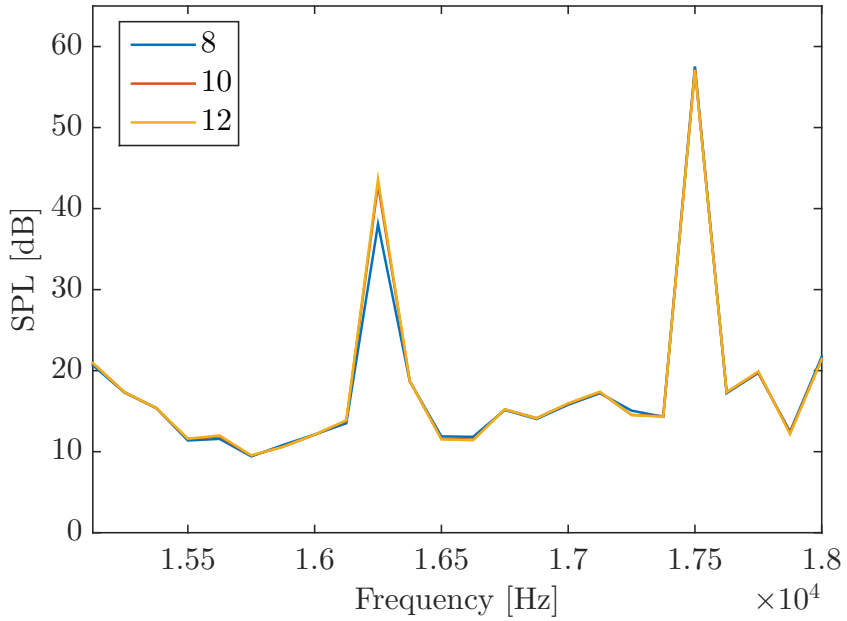

Figure 4.5: SPL as a function of the frequency for three different interpolation orders at a microphone placed at 20 cm of the cylinder extremity for a mesh of 1.7 mm and an ellipsoid of size 15-15-30 [cm].

The amplitude of the peak located at 16 250 Hz changes from 38.08 dB to 43.65 dB when considering an interpolation order equal to 10 instead of 8, that is, a difference of more than 5 dB. Similarly to the preliminary study, this difference of amplitude is judged too important for a spike and then, it has been chosen to study this case with an interpolation order of 10.

4.3.4 ICFD

Actran software has a specific interface to deal with aero-acoustic problems called iCFD. The interface is able to read as input CFD information from different solvers (as OpenFoam or StarCCM) and then to project the relevant data on the acoustic mesh created in Actran. Therefore, this utility allows to compute the aero-acoustic sources based on Lighthill analogy in the time domain. It can then convert time-domain into frequency-domain results, performing a Fourier transform of the quantities.

The visualisations displayed in figures 4.6 and 4.7 represent the ICFD output surfaces source terms, *i.e.* the divergence of the total stresses, and the volume source terms obtained from the CFD results at different frequencies: the rotation frequency 1 250 Hz, its first harmonic 2 500 Hz and the BPF (16 250 Hz). The values in themselves have no physical meaning here since it concerns the way Lighthill analogy is implemented in Actran. However, comparing the orders of magnitude and the shapes obtained is interesting.

As Lighthill analogy only accounts for aero-acoustic sources, there should be no marked source at other rotation speed harmonics than the BPF as those are in practice only due to mechanical unbalance that should not appear in numerical results. The strong symmetry-13 dipole distribution obtained at 16 250 Hz is thus consistent with the theory of the approach but this is not the case for the patterns obtained at 1 250, 2 500 Hz and others not shown here for the sake of compactness. Additionally, the order of magnitude of the first surface source at 1 250 Hz should be much lower than the result at the BPF. This aspect of the results is also nonphysical. It is then really important to keep a critical eye on the ICFD output before propagating these sources.

According to a personal discussion on those results with Jean-Louis Migeot (24 may 2022), author of "Acoustics" [31], and with the support of the FFT team, it can be said that the dipoles distributions obtained at 1 250 and 2 500 Hz seem to be an artefact caused by numerical errors in the flow modeling. The non-periodicity of the CFD mesh on the 13 rotor blades could indeed create a numerical asymmetry resulting in a source component at the harmonics of the rotation speed frequency. This problem could eventually be solved by generating a perfectly symmetrical mesh by an angular reproduction of one meshed rotor blade. Additionally, the lake of convergence study on the CFD mesh is an other possible explanation to these erroneous results.

Finally, it can be seen in figure 4.7 representing the stator volume that most of the sources generated by turbulence are located on the rotor side and is rapidly damped along the stator. Furthermore, the source term is more important at the BPF. There does not seem to be any inconsistency in these results.

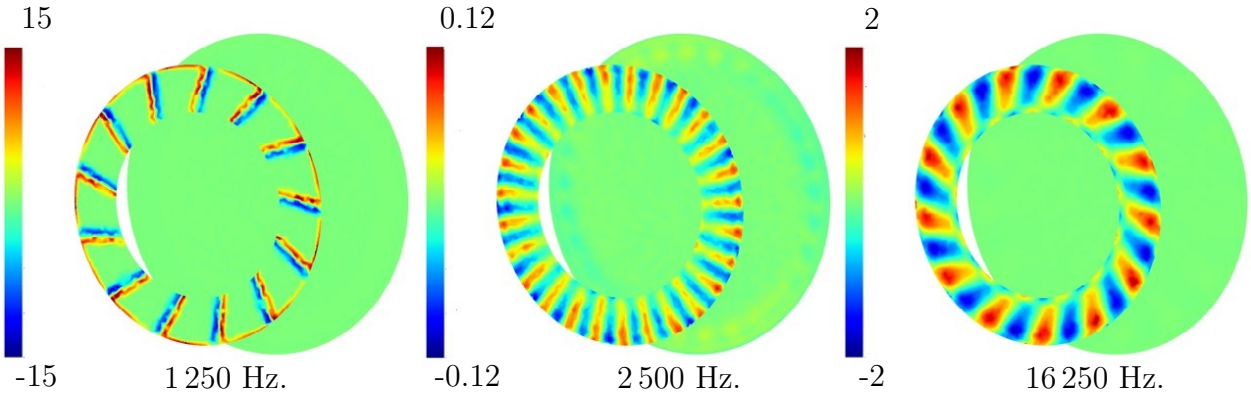

Figure 4.6: Acoustic Lighthill surfaces source terms expressed in [kg/(m^{2}s^2)] for three frequencies: 1 250, 2 500 and 16 250 Hz.

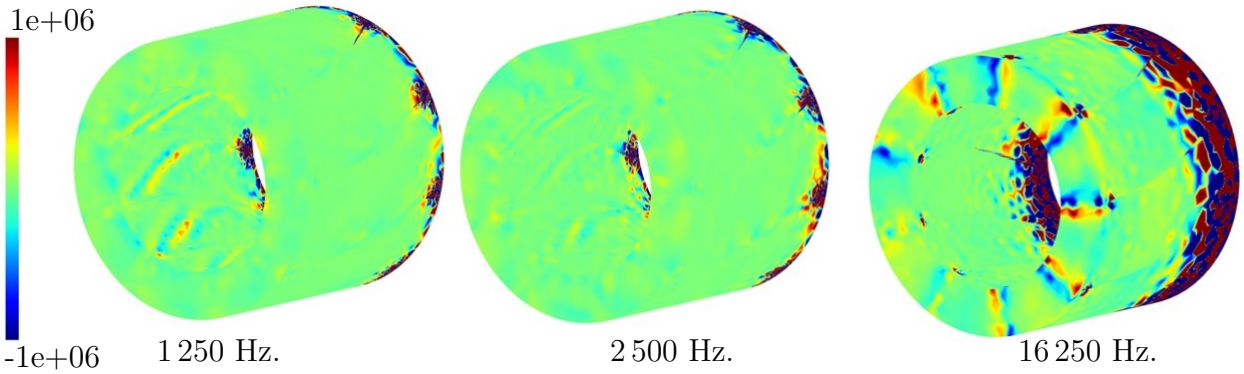

Figure 4.7: Acoustic Lighthill volume source terms expressed in [kg/(m^{3}s^2)] for three frequencies: 1 250, 2 500 and 16 250 Hz.

4.3.5 Numerical results

The SPL obtained at a microphone placed at 1 m of the cylinder axis, perpendicularly to it, resulting from the propagation of these sources is displayed in figure 4.8 on which three curves are presented: the SPL when only the two Lighthill surfaces are imposed as sources, the one when only the Lighthill volume is imposed as source and the combination of both sources.

Firstly, it can be observed that the contribution of aero-acoustic sources in the rotating domain is more significant than those from the statoric volume. As a matter of fact, the Lighthill surfaces are quite representative on their own of the total sources computed by the analogy. This result is consistent since the aerodynamic fan noise is mainly created by the moving rotor which is represented by the surface sources. The volume source represents the effect of turbulence in the domain and are less important in a fan noise case.

Moreover, the difference between the tonal noise created by the passage of the blades and the broadband noise is clearly visible. It can be noted that the first important peak is created at the rotor rotation frequency 1 250 Hz. Around this one, three other frequencies are highlighted in green. They correspond to the eigenfrequencies of a cylinder closed on one side and open on the other side. As a matter of fact, similarly to equation 3.7, such type of resonance frequency (and its harmonics) is computed by

$$f_n = \frac{(2n-1)\cdot c}{4l}. \tag{4.13}$$

In the present case, l corresponds then to 180 mm, *i.e.* the reduced size delimited by the duct opening on one hand and the first Lighthill surface on the other (which is considered in the acoustic model as a rigid boundary). The first resonance frequencies are then 472, 1 416 and 2 361 Hz.

Furthermore, it can be observed that the peak at the BPF is not especially the only or the highest one as predicted by the theory. All the multiples of the rotation frequency produce approximately equivalent sound pressure levels, except 1 250 Hz that is especially high. This of course results from the inconsistent ICFD outputs. Moreover, the especially high amplitude of the SPL at 1 250 Hz could also be explained by the fact that the fan source excites the cylinder at 1 250 Hz which is a frequency close to the natural frequency of the cylinder 1 416 Hz what creates a very high peak of resonance.

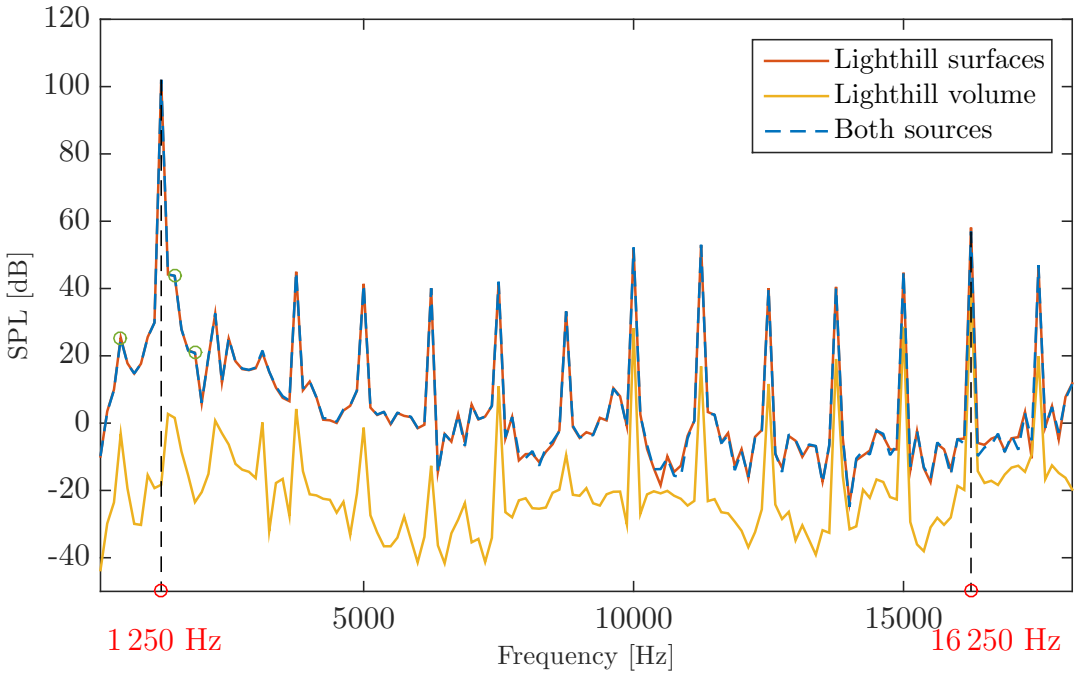

Figure 4.8: SPL as a function of the frequency for three loadcases: Lighthill surfaces, Lighthill volume or both boundary conditions at a microphone placed at 1 m of the cylinder axis, perpendicularly to it.

4.4 Comparison with experiments

This result can be compared to the experimental one provided by BaByliss in figure 4.9. This spectrum has been done for the engine *Keli* without the hair dryer casing at a microphone also placed at 1 m of the engin axis, on a plane perpendicular to it. The SPL value has no meaning in itself since BaByliss can not provide the reference of the sonometer used. It can thus not be superimposed on the numerical results at the same microphone position. Nevertheless, the position as well as the relative height of the peaks can be observed. As predicted by the theory, the most significant frequency is the BPF that manifests itself with a very high spike centred at 16 250 Hz. Additionally, some peaks appear at the rotation speed harmonics but these are by far less important and thus less noisy than the one at the BPF. They are a consequence of the imperfect machining of the blades that arises in experimental cases. It is important to highlight the fact that as the engine is without casing, duct modes are not present in this spectrum and in reality, the peak at 1 250 Hz could be higher due to a resonance effect. Finally, a maximum magnitude of only 50 dB is observed. This is due to the fact that only the first rotation speed is studied, the one requiring the least power and thus the least noisy. The SPL usually achieved for hair dryers is about 90 dB.

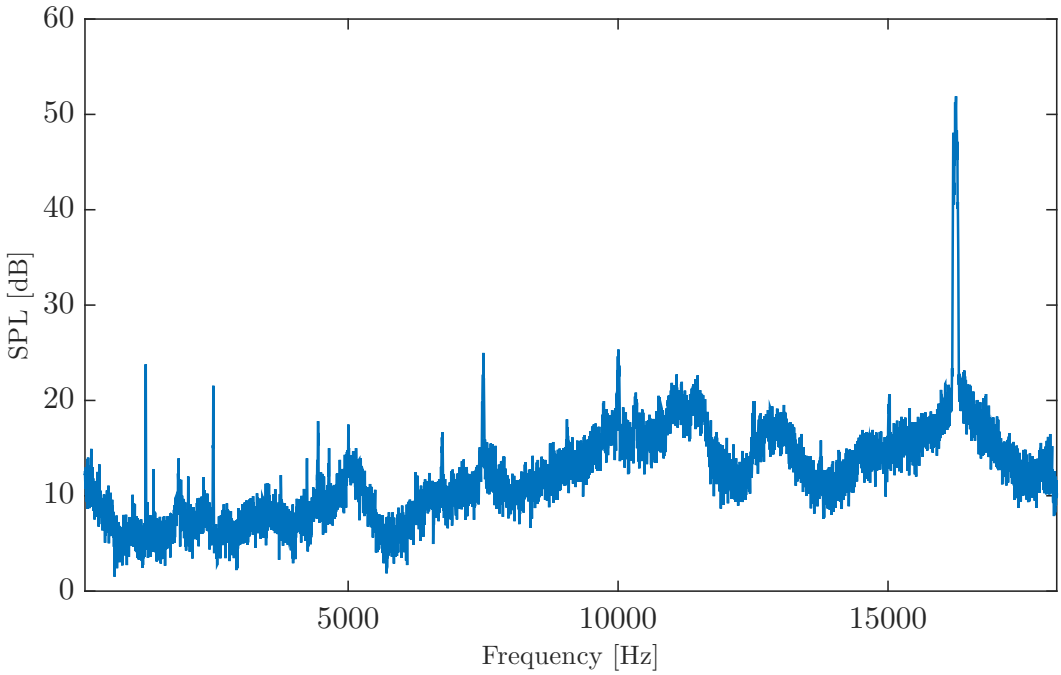

Figure 4.9: SPL as a function of the frequency provided by BaByliss for engine *Keli* at a microphone placed at 1 m on the transversal axis of the engine.

This validates the fact that the Lighthill analogy realised in the previous section shows a lake of consistency. However, as the aim of the following chapter is to reduce the noise produced by such a device, it is not problematic if the components at the rotation speed multiples have been artificially added by the numerical set-up as they are present, although to a lesser extent, in experiments too. Lighthill surfaces only, since they alone represent well the effect of the rotor, are used in the next chapter as excitation boundaries.

Chapter 5

Noise attenuation

Fan noise is not a recent issue in aero-acoustic field. The challenge for the implemented silencers is to reduce noise while avoiding performance losses. It must then be robust, light-weight and durable. Nevertheless, the cost must remain reasonable given that comfort often takes second place, after performances. In the case of this work, it is important to keep in mind that the air passage should not be blocked by the system added and that this system should be integrated inside the available space of the casing, what puts other big constraints to the design.

There are many ways to reduce the sound emission of the engine, starting with changing the rotor blades geometry [3, 24, 25]. However, this is not a degree of freedom in this work since the engine is fixed, provided in advance by another company. Therefore, it has been chosen to add a specific compact sound absorber at lower cost inside the casing of the hair dryer. Another different solution based on metamaterials is also described but firstly, the acoustic set-up is once again summarised.

5.1 Acoustic set-up

The set-up used to evaluate the efficiency of an attenuation solution is similar to the one presented in section 4.3.4, *i.e.* the rigid cylinder is placed inside an infinite elements surface ellipsoid shaped of size 15-15-30 [cm]. The interpolation order imposed is 10, corresponding to the one resulting from the convergence study in chapter 4. The studies are indeed realised applying the Lighthill surface excitation from section 4.2 as source (and not the volume source).

Regarding the post-processing, it has been decided to observe the SPL at different virtual microphones shown in figure 5.1. Microphone 1 is located perpendicularly to the cylinder principal axis, at 20 cm of it with z=100 mm. Additionally, a polar configuration is created with 180 microphones (including micro 1) on a plane perpendicular to the cylinder principal axis too with a radius equal to 20 cm. Micro 1 is then used to visualise the effect of the attenuation on the whole (or a part of the) spectrum while the polar arrangement is used to

see the shape of the SPL at one specific frequency.

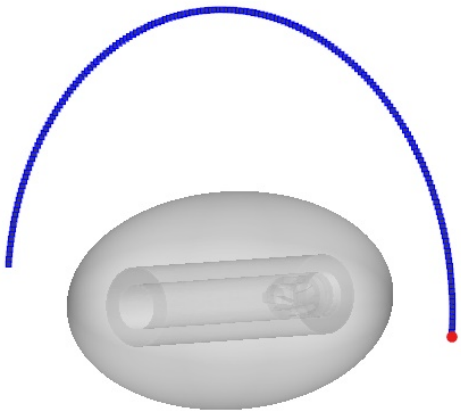

Figure 5.1: Representation of the polar virtual microphones in blue with micro 1 in red.

5.2 Acoustic Absorbers

When an incident acoustic wave hits a material, its energy is partially reflected back and the other part is absorbed by the material. The energy absorbed can then be dissipated into the material or transmitted to the other part (cf. figure 5.2). The objective of noise control through absorbers is to exploit material that reflect and transmit noise as little as possible thanks to a high internal dissipation. This is possible only if the material is designed to allow sound wave to enter, to absorb the energy and thus to decrease the reflection. It should then be studied to dissipate this energy as much as possible and transmit less. With this objective, acoustic absorbers can be mainly classified into two types: porous/fibrous materials and (micro-)perforated panels based on Helmholtz resonators.

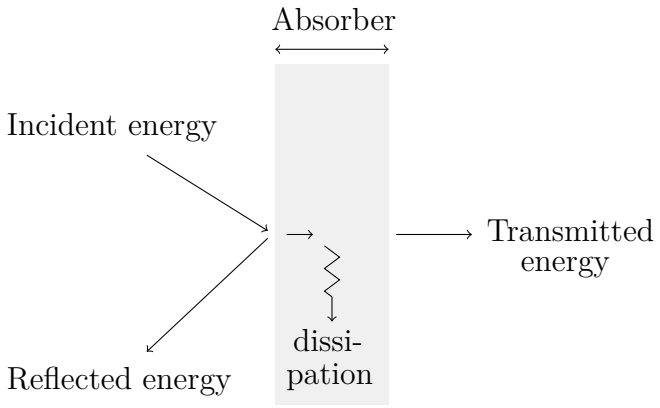

Figure 5.2: Concepts of incidence, reflection, dissipation and transmission through an absorber layer.

5.2.1 Porous/fibrous materials

5.2.1.1 Theoretical background

Porous and fibrous materials such as polyurethane foam or non woven fabrics can be seen as two phases materials with a solid frame and a fluid part (which is air in this case). Their use has the advantages to be low-cost and easy to implement. They are well known to be highly dissipative media what makes them an ideal solution for noise absorption [1, 5, 46]. Dissipation mechanisms take indeed place in four forms, the first two being the dominant contributions:

1. Energy is mainly dissipated through viscous shear given that the frame boundaries lower down the speed of the fluid particles inside the pores, adding viscous resistance;

2. Friction losses are also important since fibres vibrate and rub against each other;

3. Dissipation by scattering is made possible thanks to the bent and tortuous pathway the particles should follow;

4. Sound waves being a continuous compression and expansion of particles, they dissipate energy by creating structural vibrations.

All these viscous friction and thermal exchanges are able to damp the absorbed acoustic energy. The acoustic pressure and velocity fluctuations being inversely proportional to the size of the cavities present in that type of materials, the smaller the holes the higher the dissipation. More complex designs such as sandwich porous panels have also been developed to obtain higher transmission losses.

The most general way to characterise a porous material is through Biot theory [31] which treats the heterogeneous medium as an equivalent homogeneous one with a solid and a fluid phase. This theory is based on some macroscopic physical properties of the porous material that influence the quality of the absorption: the resistivity, porosity and tortuosity. Firstly, flow resistivity R measured in [N.s/m^4] can be described as the resistance offered to steady state fluid inside the porous material. Therefore, if the resistivity is too low, there is less viscous stress and the transmitted energy is higher and conversely, if R is too high, the porous material acts as a solid boundary and the majority of the incident wave is reflected back. Furthermore, the porosity Ω is defined as the volume of open pores divided by the total volume of the material. Similarly, if the porosity is too small, the material is seen as a solid boundary unable to absorb the incident energy. Typical values of acceptable porosities are higher than 85%. Moreover, the tortuosity α_∞ characterises the complexity of the deviation of an air particle moving inside the material. Therefore, if the tortuosity increases, the dissipation also does so.

Other theories also describe the acoustic behaviour of such materials through the use of a surface impedance such as the equivalent Delany-Bazley model [10]. An extension of the Delany-Bazley model for materials with a porosity close to one has also been proposed by

Miki [32] and is of interest for the present work. It estimates the acoustic impedance and the characteristic wave number of the material as:

$$Z_M = \rho_0 c \left[1 + 5.5 \left(10^3 \frac{f}{R} \right)^{-0.632} - j8.43 \left(10^3 \frac{f}{R} \right)^{-0.632} \right], \tag{5.1}$$

$$\tilde{k}_M = \frac{\omega}{c} \left[1 + 7.81 \left(10^3 \frac{f}{R} \right)^{-0.618} - j11.41 \left(10^3 \frac{f}{R} \right)^{-0.618} \right]. \tag{5.2}$$

Therefore, the equivalent fluid is defined by the equivalent speed of sound $\tilde{c}_M$ and density $\tilde{\rho}_M$:

$$\tilde{c}_M = \frac{\omega}{\tilde{k}_M} \quad \text{and} \quad \tilde{\rho}_M = \frac{\tilde{k}_M Z_M}{\omega}. \tag{5.3}$$

The approximation is only valid for a specific range of frequencies: $0.01 < f/R < 1$.

The equivalent surface impedance of a cavity filled with a porous material and backed by a rigid wall for waves with normal incidence is [1]

$$Z_{c,\ porous} = -j\ Z_M\ \mathrm{cotg}(\tilde{k}_M D) \tag{5.4}$$

where D is the cavity depth, the thickness of the porous layer.

The absorption coefficient of the material layer for a wave with normal incidence can be displayed for different cavity depths based on equation 2.46, imposing a resistivity R of 22 000 N·s/m^4. The analytical results are displayed in figure 5.3. The figure clearly shows that at one point, it is not necessary to increase the thickness of the porous layer as no gain is obtain at high frequencies especially.

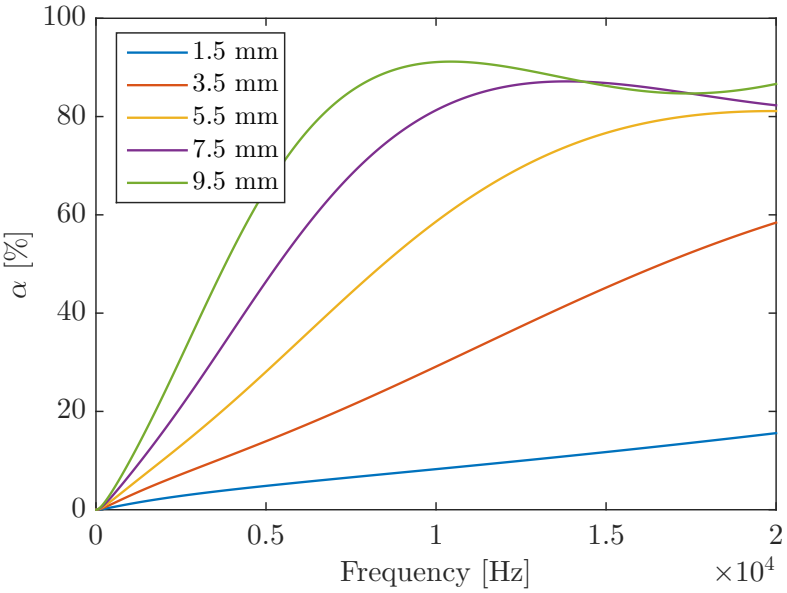

Figure 5.3: Absorption coefficient α as a function of the frequency for different depths of porous cavity using Miki model with R=22 000 N·s/m^4.

In practice, a porous layer is efficient only if its thickness is larger than a quarter of the interesting wavelength. Dissipation is indeed proportional to the local acoustic velocity which is zero on a rigid boundary and thus the highest at a quarter wavelength distance from it. This condition tends to be difficult to respect at lower frequencies, requiring too much space. This solution of attenuation is thus only applied on higher frequencies in this work.

5.2.1.2 Numerical implementation

In the present work, it has been decided to test three different porous thicknesses: 3.5, 5.5 and 7.5 mm with R=22 000 N·s/m^4 using the Miki model implemented in ACTRAN which is similar to the theoretical description just presented. These cavities are dug in the casing as depicted in red in figure 5.4.

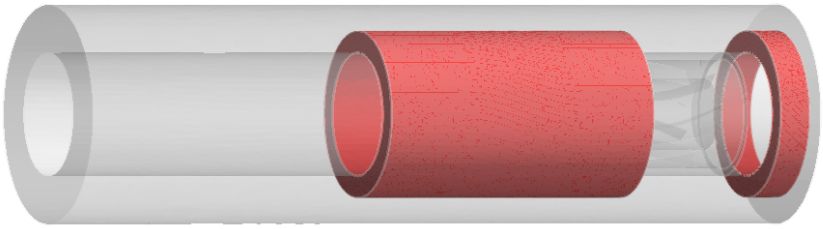

Figure 5.4: Porous cavities (in red) in the internal thickness of the cylinder.

Firstly, the results have been observed at micro 1. As displayed in figure 5.5, a good broadband attenuation is obtained: mean differences of 6.25, 16.70 and 14.09 dB are achieved with 3.5, 5.5 and 7.5 mm respectively compared to the case without absorber.

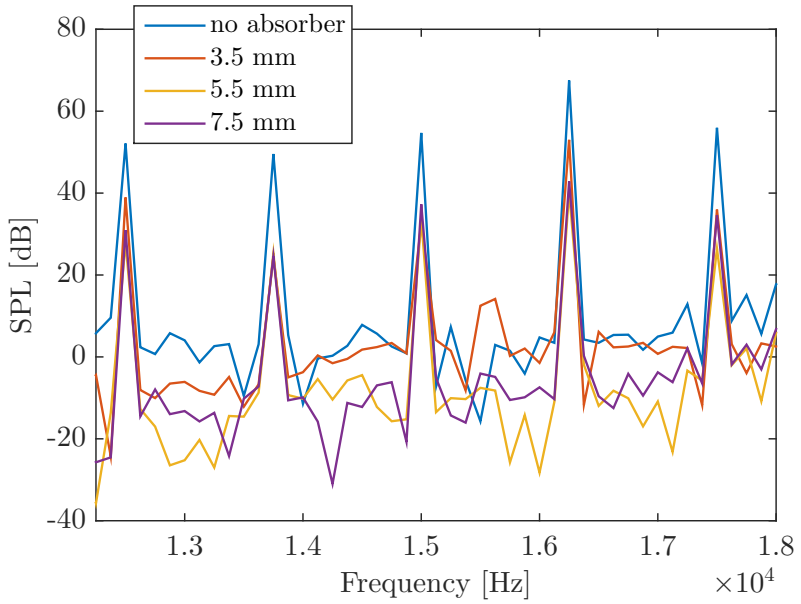

Figure 5.5: SPL as a function of the frequency at micro 1 without absorber and for three different cavity depths with R=22 000 N·s/m^4.

Nevertheless, the most uncomfortable part of the noise is due to the peaks in the SPL. The polar set has then been simulated for all the attenuation solutions, especially at four frequencies: 13 750, 15 000, 16 250 and 17 500 Hz in order to better visualise the effect of the cavity depth. Results are shown in figure 5.6 and the mean SPL (over the polar results) are summarised in table 5.1.

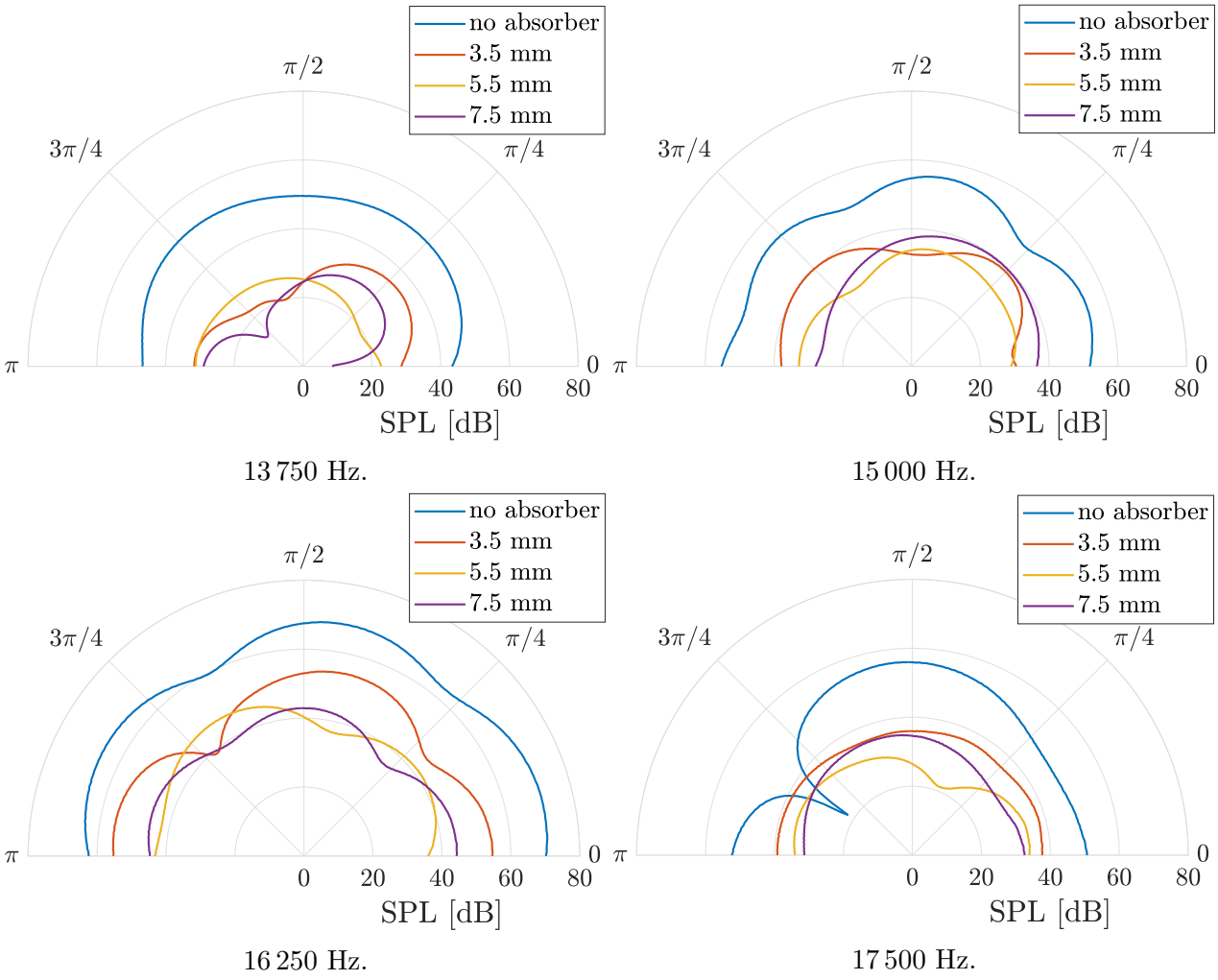

Figure 5.6: SPL at different frequencies obtained at the polar set of microphones without absorber and for three different cavity depths with R=22 000 N·s/m^4.

Porous thickness [mm]	13 750 Hz	15 000 Hz	16 250 Hz	17 500 Hz
3.5	28.47	36.50	50.53	37.14
5.5	25.11	31.69	41.87	30.01
7.5	23.26	34.65	41.64	32.79
No absorber	49.63	52.47	65.73	49.57

Table 5.1: Mean SPL [dB] at different frequencies over the polar set of microphones for three thicknesses of porous absorber and without absorber.

It can be observed that, on average, the layer of 3.5 mm is less efficient than those of 5.5 and 7.5 mm. However, no noticeable improvement is obtained with 7.5 mm compared to 5.5 mm, unlike theoretical predictions (cf. figure 5.3). This could be due to the fact that the theory computes the absorption for waves with normal incidence but in this case, the incidence is random on the cylinder walls. At 16 250 Hz, a mean decrease until 24 dB is achieved with 7.5 mm. This attenuation is satisfying regarding table 2.1 and knowing that Babyliss has only reached a maximum attenuation of 5 dB until now.

Additionally, different flow resistivities R=18 000, 22 000 and 26 000 N·s/m^4 have been tested in figure 5.7 at 16 250 Hz. From this, it can be seen that increasing the resistivity of 4 000 N·s/m^4 allows to gain on average 1 dB in the range of values implemented what can help when choosing the most advantageous material.

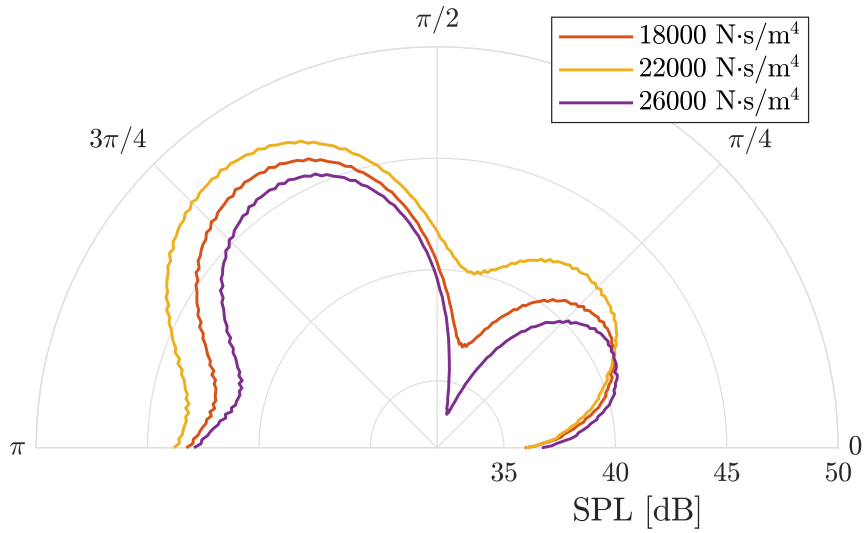

Figure 5.7: SPL at 16 250 Hz obtained at the polar set of microphones for a thicknesses of porous absorber equal to 5.5 mm and three different resistivities R.

Finally, it has been decided to test the efficiency of porous lining on the whole frequency spectrum in order to see the performance obtained at lower frequencies. Figure 5.8 shows

the results for a porous cavity of 7.5 mm depth with R=22 000 N·s/m^4 at micro 1. It can be observed that, despite theoretical predictions again, porous materials also attenuate the broadband noise in a very important way above 5 000 Hz. The amplitude of the peaks is also attenuated even at lower frequencies. A mean attenuation of 3 dB at the polar set of microphones is indeed obtained at 1 250 Hz as shown in figure 5.9. This is not as good as at 16 250 Hz; nevertheless, it is not negligible.

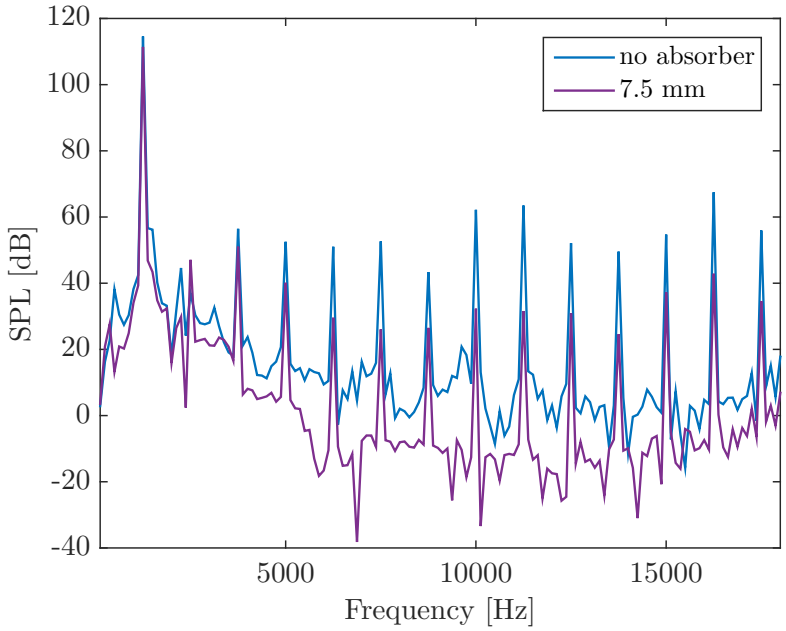

Figure 5.8: SPL as a function of the frequency at micro 1 without absorber and for a 7.5 mm porous cavity depth with R=22 000 N·s/m^4.

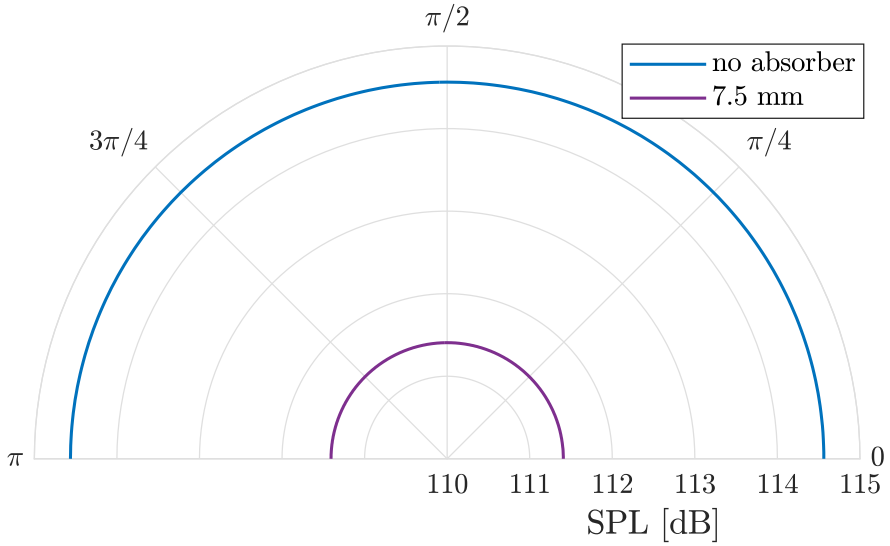

Figure 5.9: SPL at 1 250 Hz obtained at the polar set of microphones without absorber and for a 7.5 mm porous cavity depth with R=22 000 N·s/m^4.

These results seem to be promising. But even if they are efficient and low-cost, porous materials also present some drawbacks. These materials are indeed non-durable, unclean and present poorer performance at low frequencies. This reason pushes to seek other solutions which could replace porous linings or make them cleaner without requiring time maintenance. In this context, perforated panels have been investigated.

5.2.2 Perforated panels

5.2.2.1 Theoretical background

To understand the operation of perforated panels, the basics of the theory on Helmholtz resonators must first be introduced. An Helmholtz resonator (HR) consists in an air cavity closed by a small neck of a certain length l as shown in figure 5.10. It is equivalent to a mass spring system where the mass corresponds to the air oscillating in the neck and the spring to the air in the volume acting as a restoring force against those oscillations of particles. When the frequency of the incident wave is the same as the natural frequency of the system, acoustic coupling occurs, the resonator system offers minimum resistance and the incident wave energy is then exploited to drive the air molecules back and forth through the HR. The energy is thus lost in doing some work against the air molecules and the HR acts as an absorber. As the natural frequency of such a resonator mainly depends on the volume of the cavity V and on the cross sectional area S and length l of the neck, it has the advantage to be tunable to stop the frequency of interest. However, it is only useful in a narrow band around the resonance frequency of the HR which can be found to be [31]:

$$f_{\text{res,HR}} = \frac{c}{2\pi}\sqrt{\frac{S}{Vl}}. \tag{5.5}$$

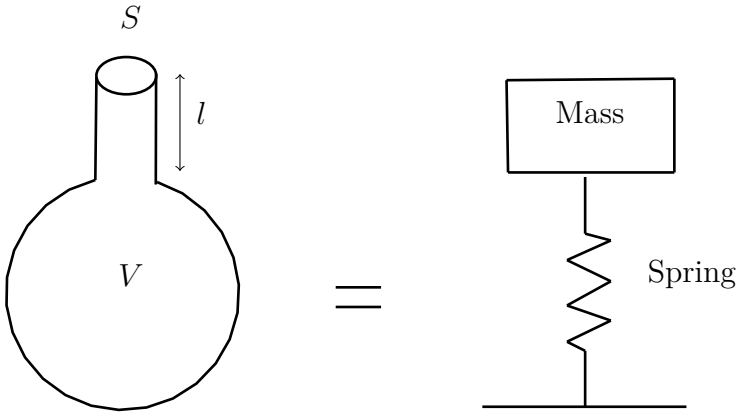

Figure 5.10: Schematic of an Helmholtz resonator equivalent to a spring mass system.

Based on this simple concept, perforated panel absorbers can be brought in. As a matter of fact, for a perforated sheet backed with an air cavity, each hole can be seen as a neck and the individual enclosed volume after as a cavity. The fundamental frequency of the whole

perforated panel being the same as the one of a single repeating unit, it can simply be derived from equation 5.5. Perforated panel are then added as lining solution along the internal walls of a duct classically to dissipate energy at the resonance frequency.

Further than perforated panels, micro-perforated absorbers, *i.e.* air cavity backed by a panel with submillimeter perforations size (MPP), are efficient solutions to increase the absorption magnitude [30, 39, 46]. As a matter of fact, in addition to the energy loss occurring at the resonance frequency of the system, there is another major dissipation mechanism: viscous losses. The viscous boundary layer around the hole orifice in that case has the same size as the hydraulic diameter and then the energy dissipation occurs due to the viscous effects present when the wave passes through the holes. The smaller the holes diameter, the larger the absorption band [40]. As simple perforated panels, it has the advantage to be light-weight, durable, resistant to humidity and to have a flexible design regarding the holes diameter and the panel porosity. Some more sophisticated MPP systems can also be used to attenuate the noise. Among them, the alternative combination of two different MPPs [23] , the use of multiple-layer MPPs [41] or micro-perforated partitions [6] have been proposed to achieve a larger absorption band.

The surface impedance of a micro-perforated panel can be analytically obtained. The analytical model described next, the one implemented in Actran, considers that the surface impedance can be seen as an air cavity in series with a perforated shell:

$$Z_{s,MPP} = Z_{c,\ air} + Z_p. \tag{5.6}$$

The impedance of a perforated shell is approximated through the theory of Maa [30] for a fluid at rest. It is expressed as a function of the perforation radius a, the fractional open area σ of the plate and the thickness l of the panel:

$$Z_p = R_p + jX_p, \tag{5.7}$$

$$R_p = \frac{8\mu l}{\sigma a^2}\left[\sqrt{1+\frac{(k_s a)^2}{32}}\right], \tag{5.8}$$

$$X_p = \frac{\omega\rho_0 l}{\sigma}\left[1+\frac{1}{\sqrt{9+\frac{(k_s a)^2}{2}}}\right]. \tag{5.9}$$

This model is only valid for $1 < |k_s a| < 10$, k_s being the shear wave number defined as $k_s = \sqrt{\omega\rho_0/\mu}$.

Analogously to equation 5.4, the impedance of the air backed cavity of depth D can be expressed as:

$$Z_{c,\ air} = -j\ \rho_0 c\ \mathrm{cotg}(kD) \tag{5.10}$$

where $\rho_0 c$ is the air characteristic impedance and $k = \omega/c$ is the wave number.

In order to respect the model range of validity, the maximum workable hole radius a is 0.11 mm to study the audible range of frequencies. Since this value is already pretty small, it

is considered as fixed in the following work and is never decreased. Similarly, the plate thickness is taken as equal to 1.5 mm for the sake of simplicity. The total impedance $Z_{s,\ MPP}$ can then be tuned considering different values of σ and D to obtain a high absorption coefficient at the frequency needed. As a matter of fact, an optimal cavity depth D_{opti} can be computed in order to cancel the imaginary part of $Z_{s,\ MPP}$ and then obtain the maximum absorption at a specific frequency, following equation 2.46.

Figures 5.11 and 5.12 show respectively the optimal cavity depth ($\Im(Z_{s,\ MPP}) = 0$) and the maximum absorption coefficient achievable with this specific depth as a function of the frequency, both for different percentages of fractional open pore area σ. These graphs are obtained from the analytical equation 5.7 to clearly show the influence of the parameters on the absorption quality but it is important to keep in mind that the absorption coefficient displayed is the one based on the equation constructed for waves with normal incidence.

Firstly, it can easily be observed that the optimal cavity depth decreases as the frequency increases. Bellow 5 000 Hz, a cavity thicker than 2 cm is needed to absorb the incident energy, what is not conceivable in many applications. Furthermore, for a specific frequency, D_{opti} increases with the porosity σ. Figure 5.12 highlights the important increase of the maximum absorption coefficient that can be achieved when σ decreases. It can also be noted that α_{max} slightly grows with the frequency. Therefore, a very important absorption quality can be theoretically obtained at high frequencies for a low σ. However, the blue curve corresponds in figure 5.11 to a very small cavity depth, smaller than 1 mm in the range [15 000;20 000] Hz, quality not always reachable in practice.

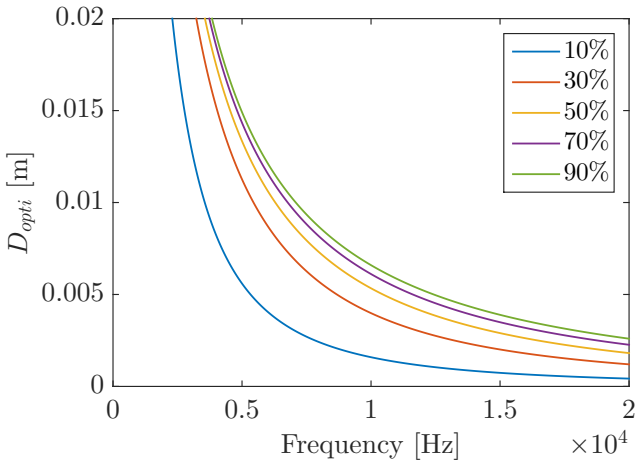

Figure 5.11: Optimal air cavity depth D_{opti} as a function of the frequency for different fractional open area σ.

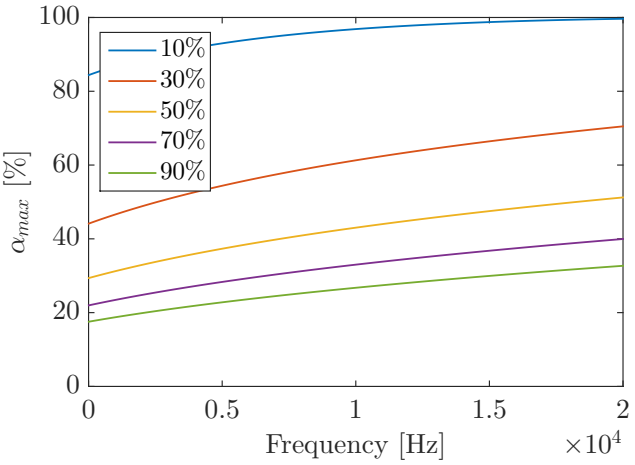

Figure 5.12: Maximum absorption coefficient α_{max} obtained with D_{opti} from figure 5.11 as a function of the frequency for different fractional open area σ.

5.2.2.2 Numerical implementation

Numerical simulations have been realised for three micro-perforated panels detailed in table 5.2 with a set-up identical to what has been highlighted in figure 5.4, imposing a rigid perforated shell component at the interface between the red cavity filled with the acoustic fluid (which is air) and the internal cylinder volume. The Maa's model presented previously is the one implemented in ACTRAN. As mentioned, a and l are fixed while three porosity values σ have been tested, leading to specific values of the cavity depth $D = D_{opti}$ following figure 5.11. These parameters have been chosen to maximise the absorption coefficient (still for a wave with normal incidence) at the BPF (16 250 Hz) as shown in figure 5.13.

Id	a [mm]	l [mm]	σ [%]	D [mm]
MPP 1	0.11	1.5	30	1.7
MPP 2	0.11	1.5	50	2.6
MPP 3	0.11	1.5	70	3.1

Table 5.2: Identifier, radius a, thickness l, porosity σ leading to an optimal cavity depth D at 16 250 Hz of three MPPs.

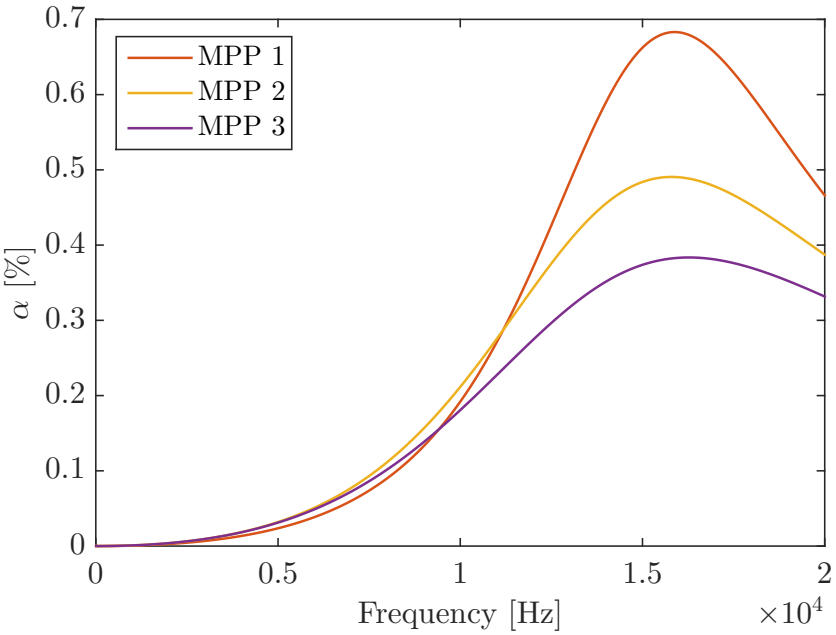

Figure 5.13: Absorption coefficient as a function of the frequency for three MPPs described in table 5.2.

The SPL at micro 1 is displayed in figure 5.14. Additionally, the results at the polar configuration are presented in figure 5.15 for four harmonic frequencies of the rotational speed.

Table 5.3 also lists the mean SPL over this set of microphones similarly to what has been presented for porous materials.

The first obvious result is the fact that micro-perforated panels are less efficient than porous linings. It can be seen that no uniform attenuation is achieved on the spectrum at high frequencies and at some points, MPPs even increase the SPL. The efficiency of each MPPs can however be better visualised by observing specific frequencies.

MPPs allow regarding the mean results a maximal attenuation of about 6 dB at 13 750 Hz (MPP 3), of 5 dB at 15 000 Hz (MPP 2) and of 3 dB at 17 500 Hz (MPP 3). This contrasts a bit with the attenuation of 9 dB obtained at 16 250 Hz, the frequency for which they have been designed. However, this is not as significant as the attenuation of 24 dB obtained in the previous subsection.

Furthermore, it can be observed that the expected result at 16 250 Hz is not marked as predicted by the theory. MPP 1 should indeed be more efficient than the two others what is not particularly the case in practice. Once again, it is important to remember that the results presented in figure 5.13 are theoretical and based on the α equation for a wave with normal incidence. The fact that the waves have random angle of incidence could impinge them to enter into the panel resulting in a better attenuation for panels with a higher porosity.

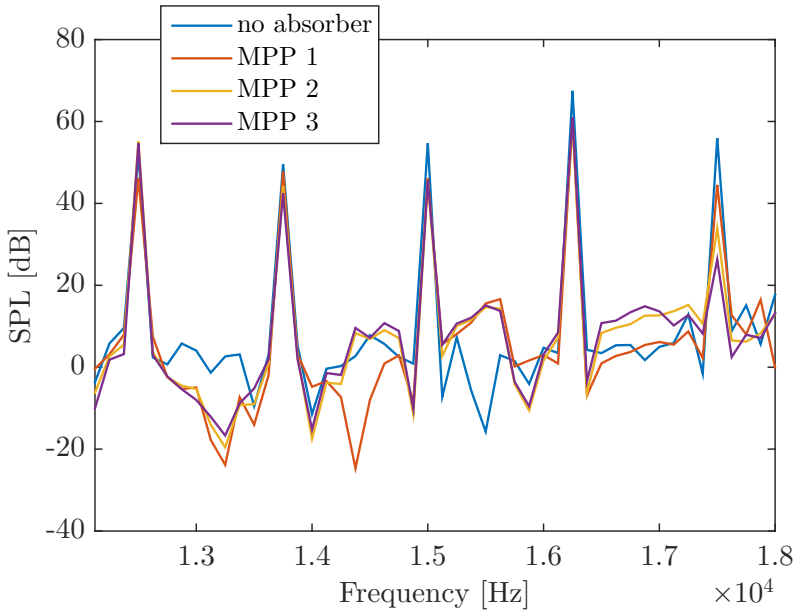

Figure 5.14: SPL as a function of the frequency at micro 1 without absorber and for three MPPs listed in table 5.2.

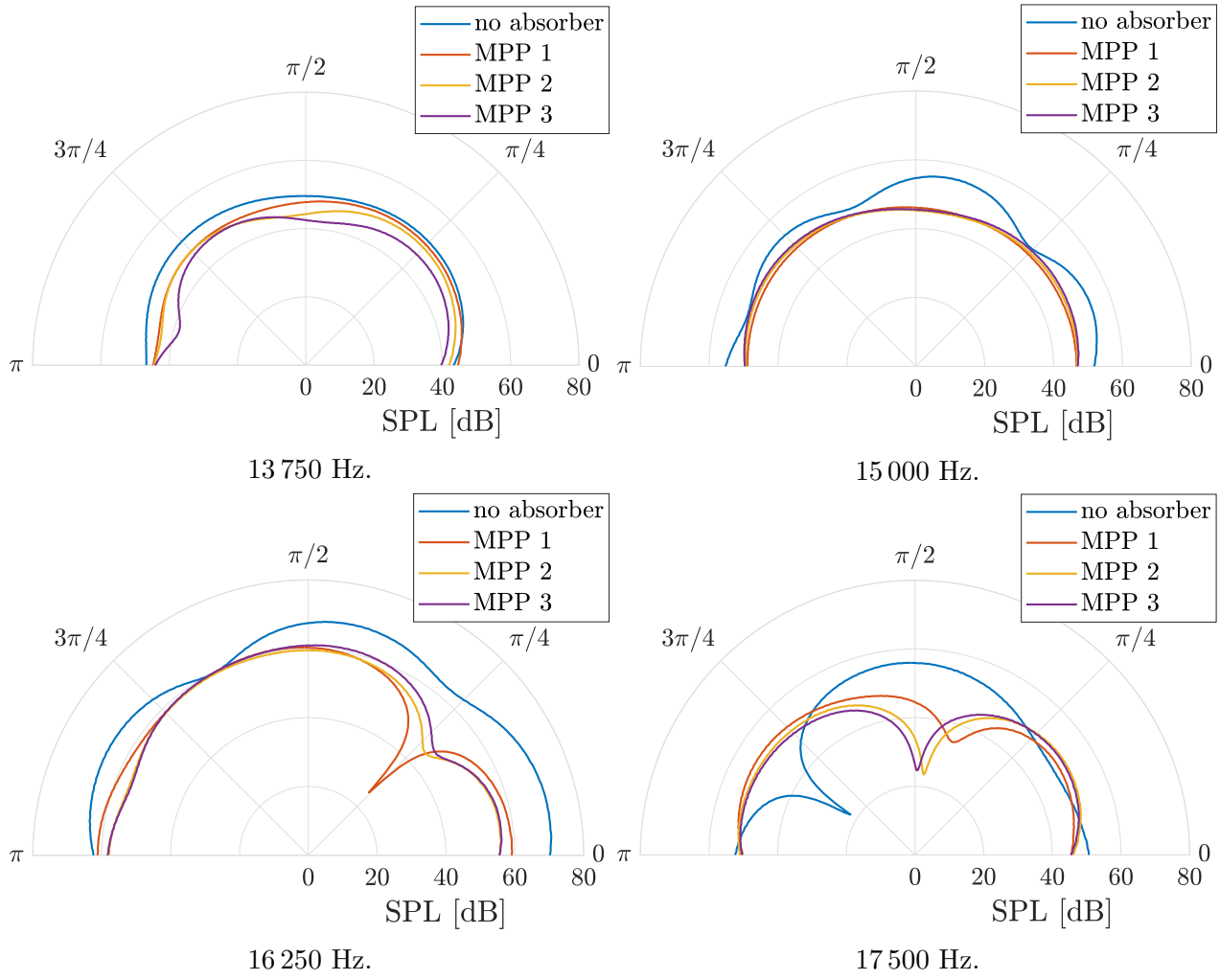

Figure 5.15: SPL at different frequencies obtained at the polar set of microphones without absorber and for three MPPs listed in table 5.2.

Id	13 750 Hz	15 000 Hz	16 250 Hz	17 500 Hz
MPP 1	47.43	47.22	56.97	47.78
MPP 2	46.00	47.57	56.25	46.92
MPP 3	43.74	48.07	57.10	46.48
No absorber	49.63	52.47	65.73	49.57

Table 5.3: Mean SPL [dB] at different frequencies over the polar set of microphones for three types of MPP presented in table 5.2 and without absorber.

5.2.3 Micro-perforated panels with porous materials

5.2.3.1 Theoretical background

In some cases, the cavity of perforated panels can be backed with porous materials to create a double coupling meaning that the longitudinal sound wave makes the panel vibrate and then the panel itself does work on the air particles of the porous medium to create a to and fro movement. Some additional energy is then lost due to viscosity and friction. Adding porous materials allows to obtain a broader attenuation frequency range around the natural frequencies of the equivalent HR network. Similarly, MPPs can also be coupled with porous material filling the cavity [28, 43].

In that case, the surface impedance can be seen as a porous cavity in series with a perforated shell:

$$Z_{s,MPP} = Z_{c,\ porous} + Z_p \tag{5.11}$$

where $Z_{c,\ porous}$ and Z_p are computed using equations 5.4 and 5.7 respectively.

5.2.3.2 Numerical implementation

The porous model implemented is the one from Miki with R=22 000 N·s/m^4. Figure 5.16 shows the theoretical effect of adding porous materials in the cavity on the absorption coefficient for a wave with normal incidence for the three MPPs implemented previously. It can be seen that adding porous materials allows indeed to broaden the absorption frequency band and to create a higher peak in α.

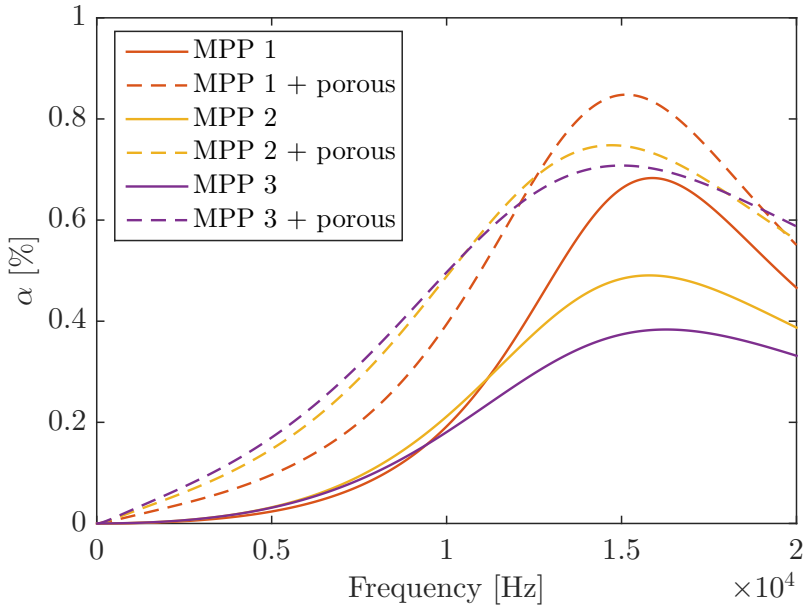

Figure 5.16: Absorption coefficient as a function of the frequency for three MPPs described in table 5.2 and the comparison with the same MPPs backed by porous cavities.

The numerical results are displayed in figures 5.17 and 5.18. The mean values over the polar set of microphones are also listed in table 5.4.

Regarding figure 5.17, it can be observed that adding porous materials in the cavities makes it possible to obtain a uniform attenuation. Over the range [12 125;18 000] Hz, mean attenuations of 9.02, 11.37 and 12.45 dB are indeed achieved with MPP 1, MPP 2 and MPP 3 respectively, all porous backed.

Furthermore, it can be observed that adding porous materials in the cavities enables to obtain better results than for MPPs backed by air cavities at the specific frequencies where peaks appear. A maximal attenuation of 23 dB is observed at 13 750 Hz, of 15 dB at 15 000 Hz and of 12 dB at 17 500 Hz through the use of MPP 3, the panel with the highest porosity. A maximum attenuation until 26 dB appears at 16 250 Hz, the frequency for which it is designed. Once again, the analytical results computed for waves with normal incidence do not correspond to what has been numerically obtained since MPP 1 porous backed should be the most efficient solution.

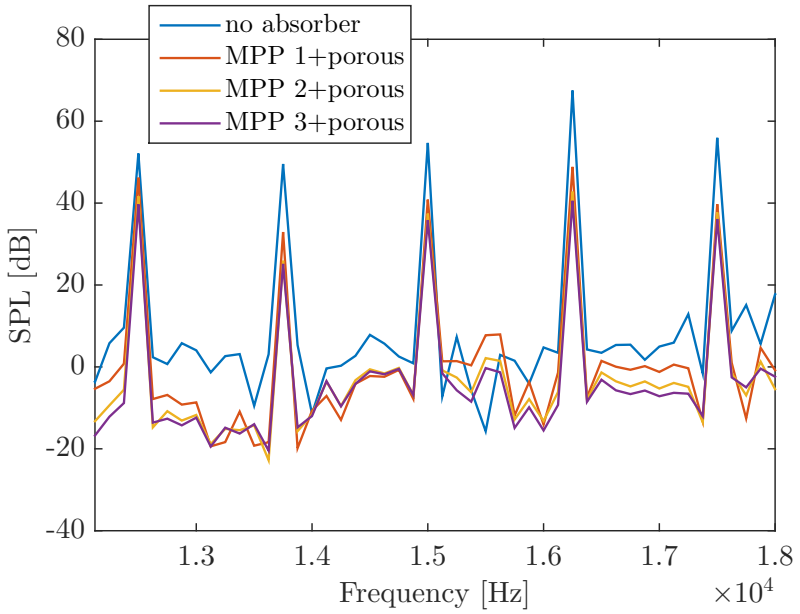

Figure 5.17: SPL as a function of the frequency at micro 1 without absorber and for three types of MPPs backed by porous cavities.

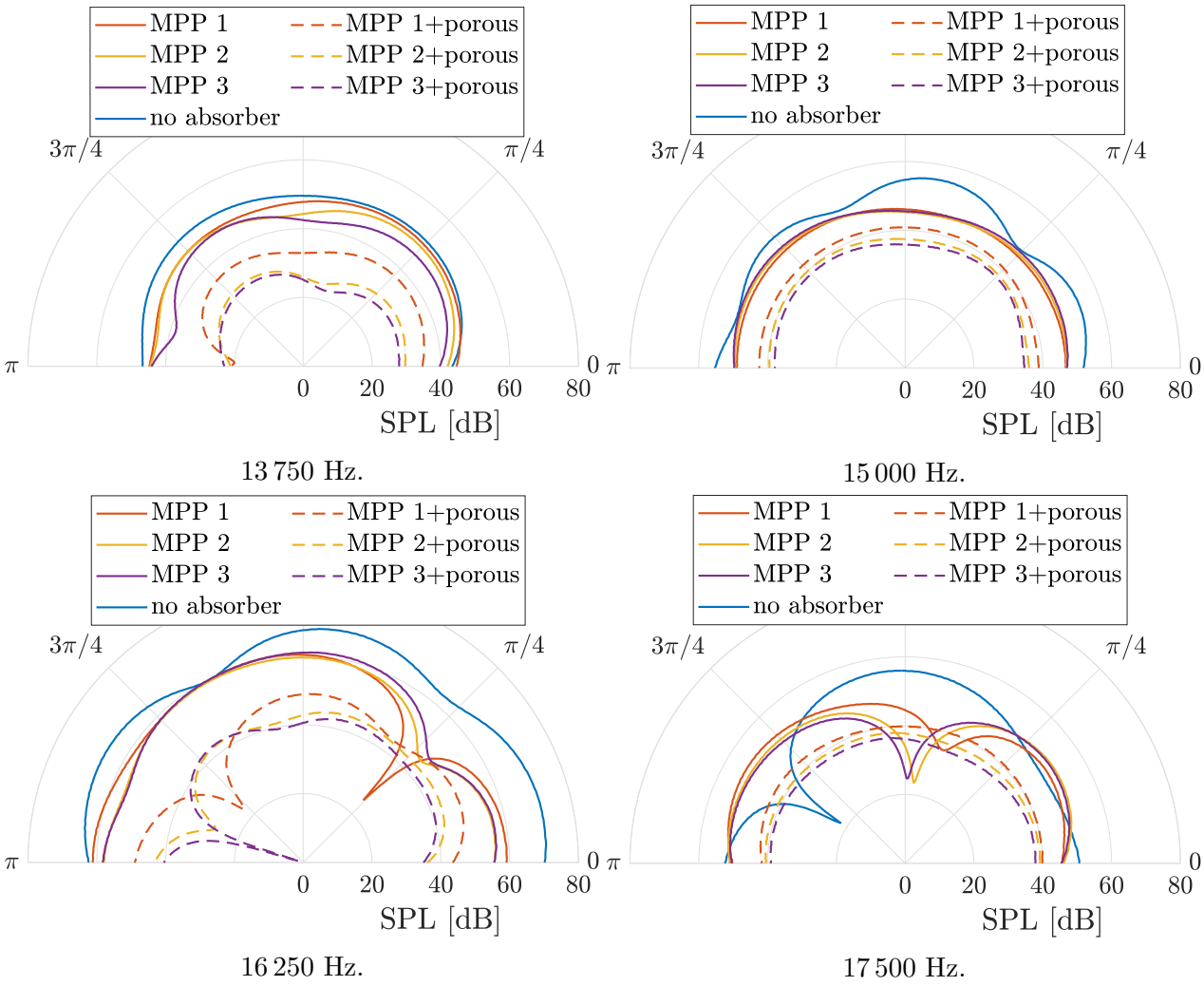

Figure 5.18: SPL at different frequencies obtained at the polar set of microphones without absorber and for three types of MPPs backed by air or porous material filled cavities.

Id	13 750 Hz	15 000 Hz	16 250 Hz	17 500 Hz
MPP 1 + porous	33.95	41.05	44.14	40.98
MPP 2 + porous	27.91	38.33	41.09	38.77
MPP 3 + porous	26.52	37.07	39.34	37.13
No absorber	49.63	52.47	65.73	49.57

Table 5.4: Mean SPL [dB] at different frequencies over the polar set of microphones for three types of MPPs backed by porous cavities and without absorber.

5.2.4 Discussion

Three absorber types have been presented to attenuate noise at high frequencies. They all allow a broadband noise attenuation but MPPs are designed for the attenuation to be maximal at a specific frequency, which is the BPF in the case of the present work. The mean attenuation obtained on the polar set of microphones are summarised in table 5.5 in order to better compare tables 5.1, 5.3 and 5.4.

Absorber type	13 750 Hz	15 000 Hz	16 250 Hz	17 500 Hz
porous 3.5 mm	21.16	15.97	15.20	12.43
porous 5.5 mm	24.52	20.78	23.86	19.56
porous 7.5 mm	26.37	17.82	24.09	16.78
MPP 1	2.20	5.25	8.76	1.79
MPP 2	3.63	4.90	9.48	2.65
MPP 3	5.89	4.40	8.63	3.09
MPP 1 + porous	15.68	11.42	21.59	8.59
MPP 2 + porous	21.72	14.14	24.64	10.80
MPP 3 + porous	23.11	15.40	26.39	12.44

Table 5.5: Mean attenuation [dB] over the polar set of microphones for the different types of absorbers with the best result highlighted in red for each frequency.

What can be concluded is that MPPs are by far less interesting than the other two solutions. The difference between porous linings and MPPs backed by porous cavities is that porous materials create a good uniform attenuation over all the frequencies studied. Conversely, MPPs with porous cavities can generate a higher attenuation at a specific frequency but are less efficient at the others. As one rotor rotation speed has been considered in this study, the focus is only put on attenuating 16 250 Hz. The BPF is indeed the most important frequency to cancel as highlighted through experiments (cf. figure 4.9). MPPs porous backed are thus more advantageous.

Additionally, the practical implementation of the solution should be taken into account in the comparison. Porous materials are less expensive but it can more easily be contaminated by dirt. On the other hand, micro-perforated panels are in some extent costlier but allow to protect the porous material from contamination. The MPPs with porous cavities seem finally to be the best option for high frequency noise attenuation. A treatment for low frequencies, especially targeted at the rotor rotation speed frequency, should then be provided in order to obtain a complete study of noise attenuation. This is the subject of the following section based on metamaterials.

5.3 Metamaterials

5.3.1 Theoretical background

Metamaterials are a more recent type of silencers. They are defined as artificial materials made of subwavelength periodic structures designed to manipulate and propagate sound waves in a controlled way. Metamaterials were required in the acoustic field because of the need in attenuating low frequencies. They are then mainly developed to bypass the mass-density law of sound transmission stating that the acoustic transmission is inversely proportional to the isolating wall thickness. Following this law, the attenuation at low frequencies using traditional non-resonant materials requires very thick walls what is not possible in most cases. The most common metamaterials are based on locally resonant units such as Helmholtz resonators or membranes.

A classical existing solution based on the HR concept presented above is the acoustic liner; it consists in a perforated sheet over a honeycomb structure equivalent to an array of HR [29]. It is often used for aeronautical devices such as aircraft nacelles. Many other sound barrier mechanisms have been implemented based on this type of resonance such as, for instance, meta-structures composed of funnel-shaped HRs [7] or coplanar spiral-shaped HRs [4]. However, these two slow down or prohibit the fluid passage what is not an option in this case.

Secondly, membrane type metamaterial, *i.e.* a stiff small mass immersed in a circular soft membrane, is a particular spring-mass system that has an effective purely imaginary speed of sound in a certain frequency range. This imaginary speed of sound is due to an effective negative mass density and causes the acoustic wave to exponentially decay over space. This very specific system is often used in duct acoustic but the membrane has the major inconvenient to block the mean flow, it is therefore not of interest for the present work but detailed implementations can be found in various articles [33, 34, 50].

The challenge is then to enhance the airflow passing what is the primary function of a hair dryer. It is achievable by considering a transverse bilayer metamaterial where the two regions have different impedances (Z_1 and Z_2) and refractive indices (n_1 and n_2) as depicted in figure 5.19. This contrast between the acoustic properties of the two regions is necessary to obtain attenuation at the desired frequency. This can notably be achieved through the specific structure presented by Ghaffarivardavagh *et al.* [16] where region 2 corresponds to channels coiled in the form of helix as shown in figure 5.20. As the acoustic waves are forced to propagate through the helical structure, region 2 is equivalent to a medium with a high effective refractive index. It can indeed be found that [51]

$$Z_2 = \frac{\rho_0 c_0}{t(r_2 - r_1)} \quad \text{and} \quad n_2 = \frac{1}{\sin\phi} \tag{5.12}$$

where r_1 and r_2 are respectively the internal and external radii of the metamaterial and ϕ is the helix angle. Whereas, in region 1, the classical properties are:

$$Z_1 = \frac{\rho_0 c_0}{\pi r_1^2} \quad \text{and} \quad n_1 = 1. \tag{5.13}$$

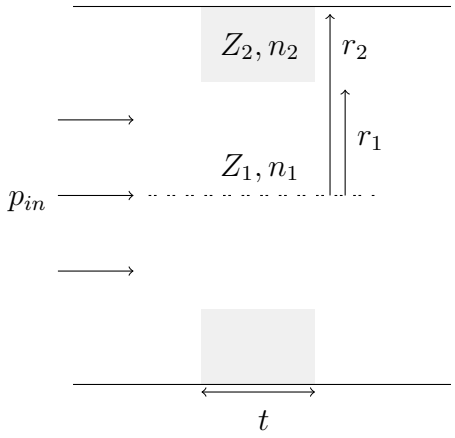

Figure 5.19: Transverse bilayer metamaterial as theoretically presented in [16] for a wave with normal incidence.

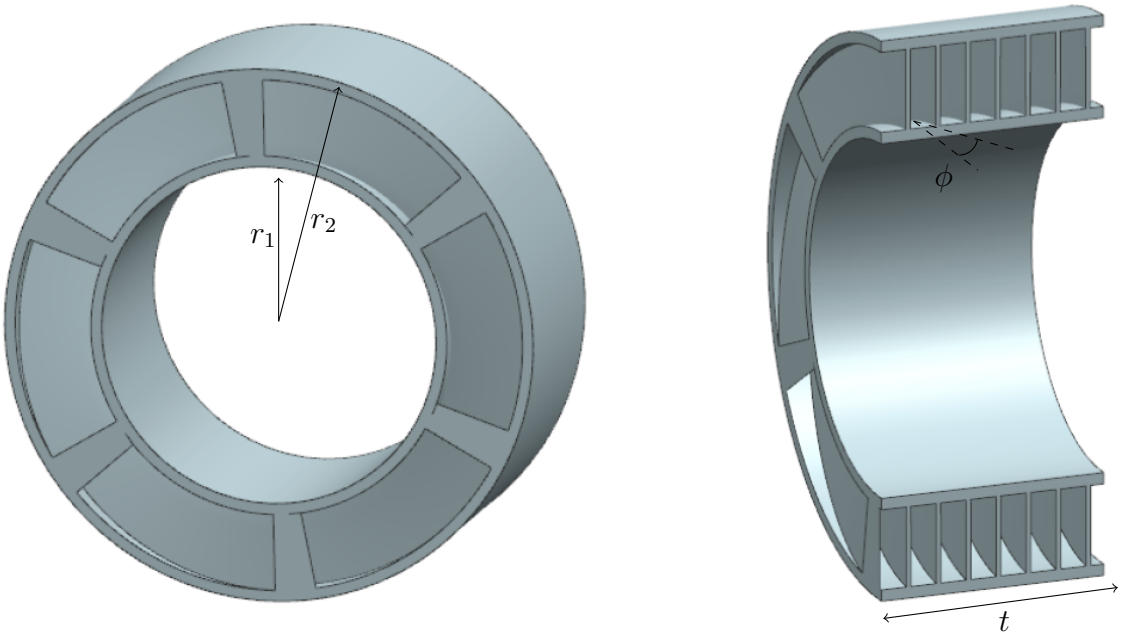

Figure 5.20: Ultra-open metamaterial with channels coiled in the form of helix with region 1 for $0<r<r_1$ and region 2 for $r_1<r<r_2$.

The key principle is to obtain resonance in region 2 while region 1 remains in a continuum state what is possible since they present different refractive indexes. It is known, by analogy to any oscillating system as a pendulum [22], that a phase shift of π appears when any system is excited at resonance. In these specific conditions, the waves leaving region 2 are out-of-phase with respect to the waves who have travelled region 1 resulting in a destructive

interference. The resonance of region 2 is achieved when

$$n_2 \cdot t = \frac{\lambda}{2} \tag{5.14}$$

$$\Leftrightarrow \frac{t}{\sin\phi} = \frac{\lambda}{2}, \tag{5.15}$$

where t is the thickness of the metamaterial. Under this condition, the waves are radiated by the resonator in opposite phase into the host structure leading to a stop band effect. This system of attenuation is effective for both waves with normal or oblique incidence and at all the multiples N of $\lambda/2$. As it is also effective at low frequencies, it has been decided to implement it in the cylindrical geometry of this work.

5.3.2 Numerical implementation

The frequency of interest is 1 250 Hz, the rotation speed frequency. Different metamaterials have been numerically tested between 900 and 1 700 Hz, adding them in the classical set-up thanks to a horn-like chamfer according to figure 5.21 with infinite surface boundary condition. The acoustic fluid is allowed to penetrate the metamaterial channels where the mesh is refined to 1 mm in order to correctly feel the geometry.

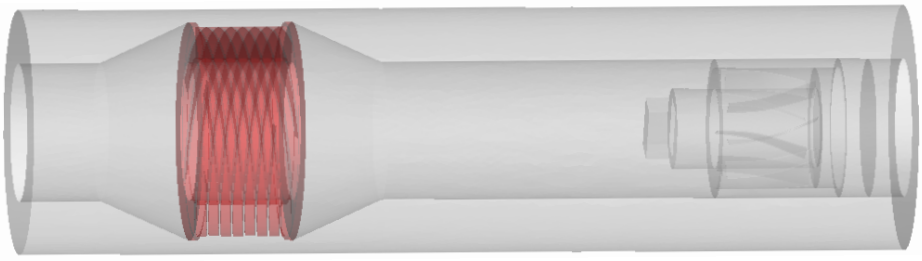

Figure 5.21: Ultra open metamaterial (in red) added in the cylinder set-up.

A very important point to mention is the fact that, in order not to alter the air flux inside the hair dryer, the metamaterial has been added inside the casing of the cylinder through the help of integration chamfers. However, these horn-like shapes in themselves have some impact on the waves propagation and thus on the results.

Figure 5.22 shows notably the SPL for the two geometries (simple cylinder and hollowed out cylinder with a 23° angle) without metamaterials. It can be observed that the amplitude of the peak is increased of 11.9 dB at 1 250 Hz. Figure 5.23 displays the output maps at the same frequency for the two geometries. From those, the hypothesis is made that the modification of the geometry is similar to a change in the boundary conditions in the left part of the cylinder since at a specific wavelength, the nodes are not positioned at the same place (different z values). This is a major difference between the results presented in the paper and in this work that must be kept in mind.

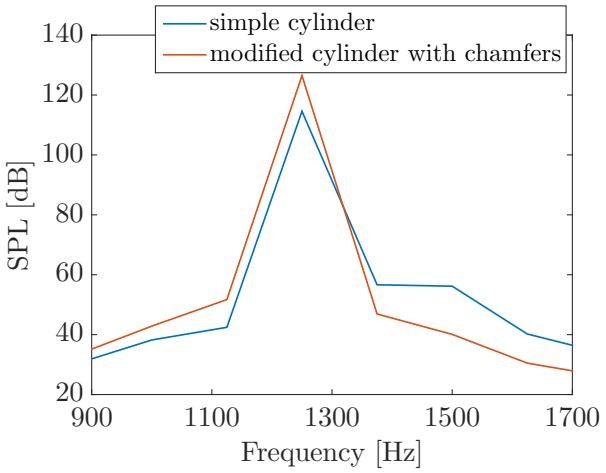

Figure 5.22: SPL as a function of the frequency at micro 1 for the two geometries.

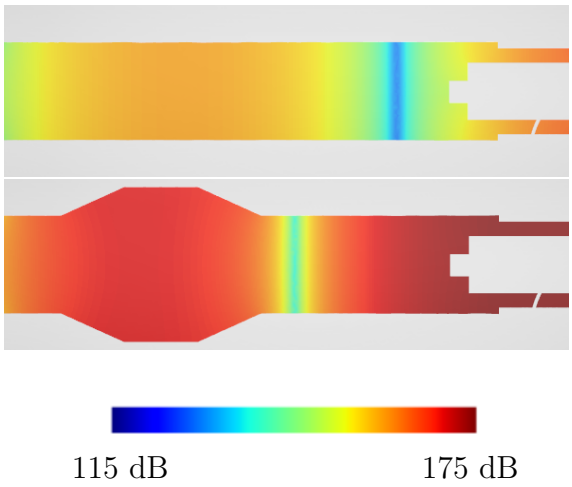

Figure 5.23: SPL output map [dB] at 1 250 Hz for the two geometries.

Five metamaterials have been first implemented around the configuration of interest (cf. equation 5.15). Their geometrical characteristics are listed in table 5.6. In this first analysis, the metamaterials are all integrated in the internal radius of the cylinder with the same angle of chamfer, of opening equal to 23°.

Id	ϕ [°]	t [mm]	r_1 [mm]	r_2 [mm]
Meta 1	9	20.3	15.5	24.5
Meta 2	9	19.3	15.5	24.5
Meta 3	9	21.3	15.5	24.5
Meta 4	8	20.3	15.5	24.5
Meta 5	10	20.3	15.5	24.5

Table 5.6: Identifier, helix angle ϕ, thickness t, internal radius r_1 and external radius r_2 of five ultra open metamaterials (1,2,3,4,5).

Figure 5.24a shows the comparison between metamaterials with different thicknesses at microphone 1. Regarding the theory, Meta 3 should be the most efficient system at 1 250 Hz. However, it can be observed that this is Meta 1 that creates the strongest peak attenuation of 16.8 dB at microphone 1 against respectively 12 and 7 dB for Meta 2 and 3. Additionally, Meta 2 seems to be more efficient at 1 375 Hz and similarly, Meta 3 presents a small dip at 1 125 Hz. This shows that as the thickness t increases, the frequency attenuated decreases. This result is in accordance with equation 5.15.

Furthermore, figure 5.24b displays results for three metamaterials with different helix angles. Meta 1 is still the best solution of attenuation at 1 250 Hz. It can be seen that the attenuated

frequency increases with the helix angle as Meta 4 presents a dip at 1 125 Hz and Meta 5 at 1 375 Hz. This is also consistent with equation 5.15.

Additionally, figure 5.25 shows that, contrarily to cases with absorbers at higher frequencies, the SPL at 1 250 Hz is constant on a polar set of microphones. It is therefore consistent to study the efficiency of metamaterials based on results at micro 1 only since it correctly relates the global trends.

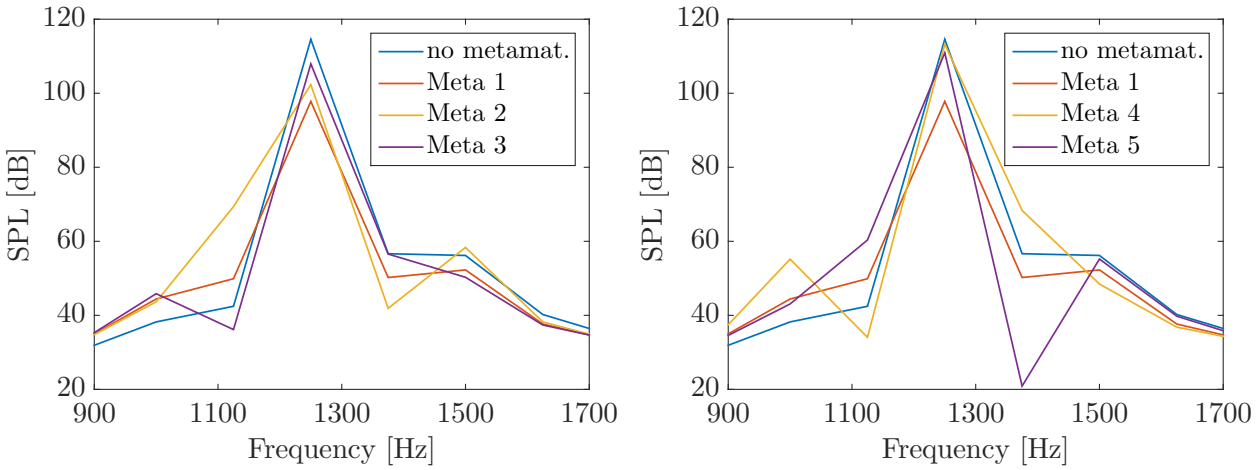

(a) Metamaterials (1,2,3). **(b)** Metamaterials (1,4,5).

Figure 5.24: SPL as a function of the frequency at micro 1 without metamaterial and for three metamaterials as described in table 5.6.

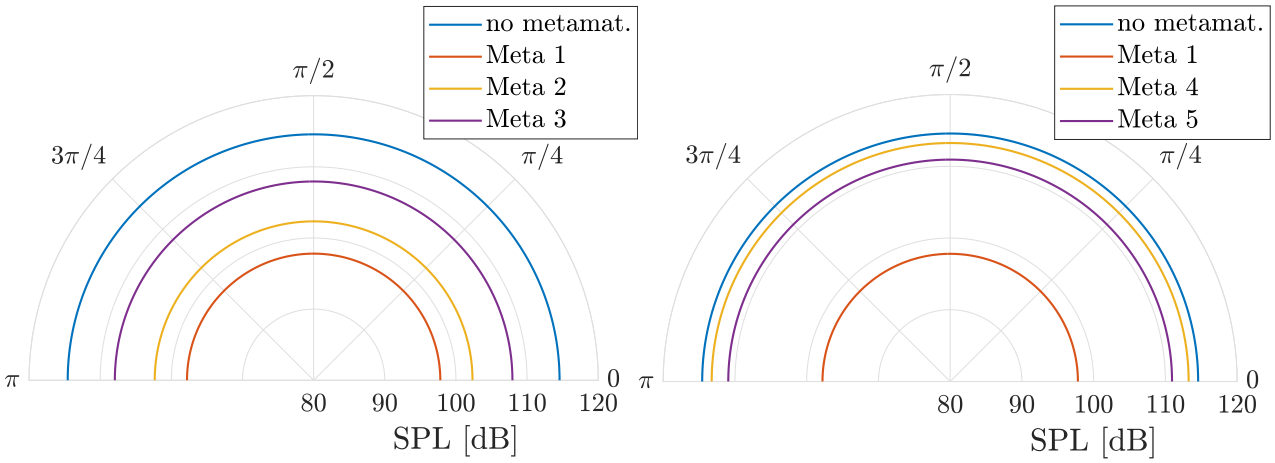

(a) Metamaterials (1,2,3). **(b)** Metamaterials (1,4,5).

Figure 5.25: SPL at 1250 Hz obtained at the polar set of microphones without metamaterials and for three metamaterials as described in table 5.6.

The phase output map at 1 250 Hz for Meta 1 is displayed in figure 5.26. The difference between the phase in the metamaterial (0°) and the phase inside zone 1 of the cylinder (180°)

is clearly visible at this frequency. The direct consequence is the SPL shown in figure 5.27 that translates the destructive interference. The attenuation at the output (left part) of the metamaterial is observed as the transmitted wave has its sound pressure level decreased from 160 to 120 dB on a very small distance. The resonance of the metamaterial can also be observed since its pressure is especially high at this frequency.

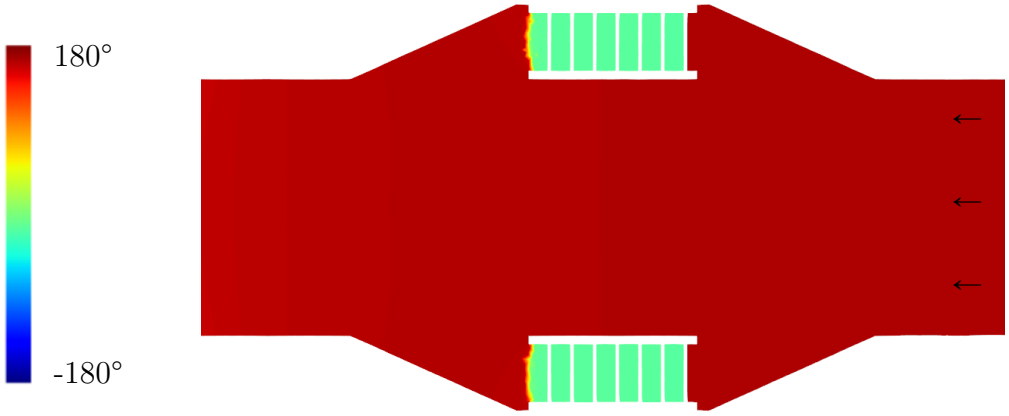

Figure 5.26: Pressure phase output map at 1 250 Hz for Meta 1.

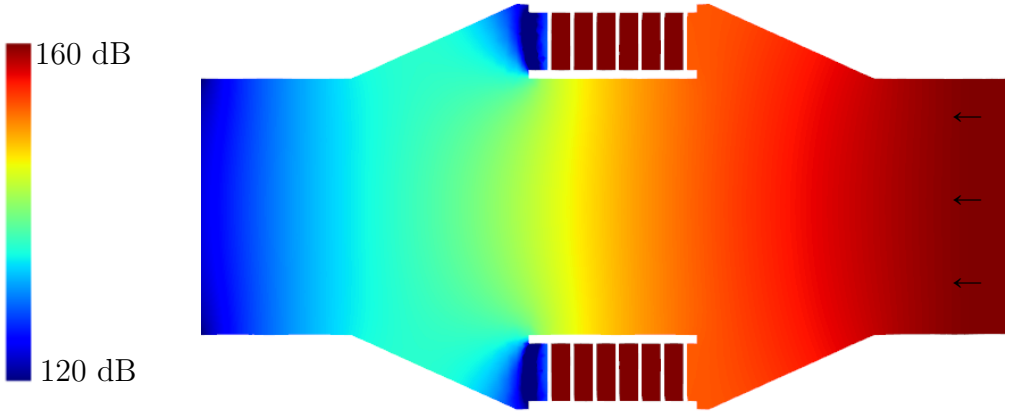

Figure 5.27: SPL output map at 1 250 Hz for Meta 1.

Finally, according to the paper [16], if the impedance ratio Z_2/Z_1 decreases (with a constant ratio of refractive indexes), the attenuation should be obtained on a larger frequency range since the opening area of region 1 is decreased. Therefore, additional tests have been carried out around the working configuration of Meta 1 with different radii. These changes of parameters should not impact the frequency of attenuation, only dictated by the thickness t and the helix angle ϕ. The additional metamaterials are listed in table 5.7. It is

important to note that for Meta 6 and 7, as it is the external radius that is modified, the opening angle (initially equal to 23°) is also modified. Therefore, to see if a variation of chamfer angle has an influence on the results, Meta 10 has been tested too. It is exactly the same metamaterial as Meta 1 but integrated in the cylinder with a chamfer angle 10° smaller.

Figures 5.28a and 5.28b show the SPL at micro 1 for a change of external and internal radii respectively. However, no general trend can be observed regarding the impedance ratio as predicted theoretically. As a matter of fact, Meta 7 should create an attenuation on a broader spectrum than Meta 1 but this is not the case in the numerical results. Similarly, Meta 8 should be efficient on a larger frequency band than Meta 1 and 9 but this is not especially the case. Figure 5.29 displays the individual effect of the chamfer on the resulting SPL. As this angle is decreased for Meta 10 (gentler slope), the performance are reduced of 3 dB at 1 250 Hz compared to Meta 1. Therefore, the changes obtained for Meta 6 and 7 are also influenced by the change of chamfer. However, it is complicated to quantify the two contributions.

This study demonstrates that the resulting attenuation is extremely sensitive to all the geometrical parameters. This can be due to different factors. Firstly, the results in the paper are based on an integration of the metamaterial inside the cylinder as displayed in figure 5.19. However, it has been shown that the mandatory entrance cone and its angle play a role in the mechanisms of reflection for the waves entering the metamaterial (cf. figures 5.23 and 5.29). Therefore, it can not directly be said that as the external radius increases or internal radius decreases, a broader attenuation is obtained. Additionally, the difference between the ratios Z_2/Z_1 described in table 5.7 is relatively small (compared to the cases studied in the paper) as the geometry does not allow an important change of radii. All these results show that implementing a metamaterial in a real case may be complicated. An experiment based on Meta 1 has thus been carried out to see its practical efficiency.

Id	ϕ [°]	t [mm]	r_1 [mm]	r_2 [mm]	chamfer angle [°]	Z_2/Z_1 [-]
Meta 1	9	20.3	15.5	24.5	23	4.13
Meta 6	9	20.3	15.5	22	17	5.72
Meta 7	9	20.3	15.5	27	29	3.23
Meta 8	9	20.3	8.5	24.5	23	0.70
Meta 9	9	20.3	12	24.5	23	1.78
Meta 10	9	20.3	15.5	24.5	13	4.13

Table 5.7: Identifier, helix angle ϕ, thickness t, internal radius r_1 and external radius r_2 of six ultra open metamaterials (1,6,7,8,9,10).

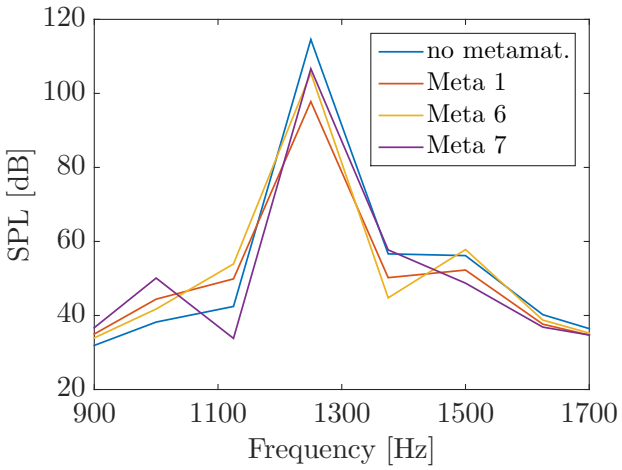

(a) Metamaterials (1,6,7).

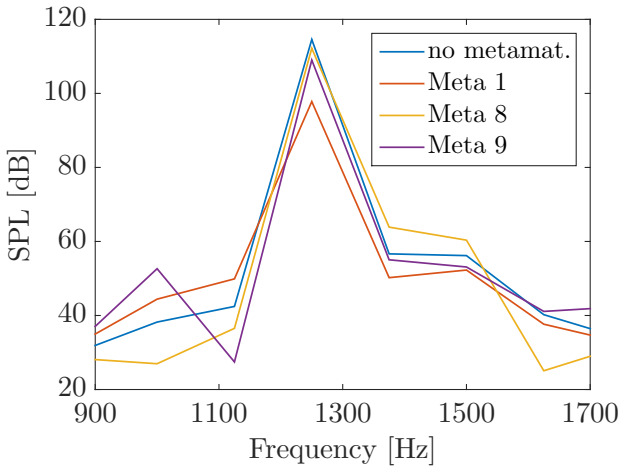

(b) Metamaterials (1,8,9).

Figure 5.28: SPL as a function of the frequency at microphone 1 without metamaterial and for three metamaterials as described in table 5.7.

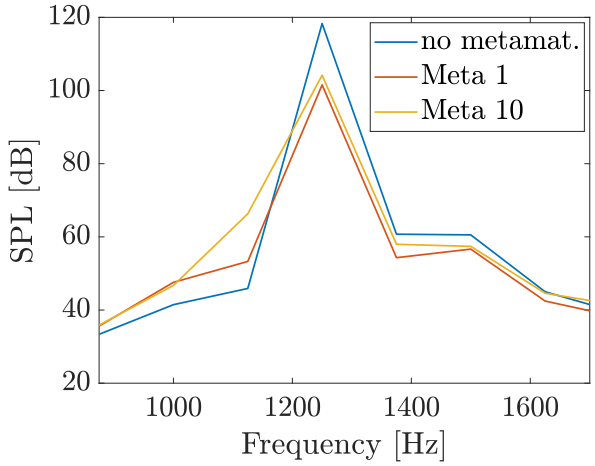

Figure 5.29: SPL as a function of the frequency at microphone 1 without metamaterial and for two metamaterials as described in table 5.7.

5.3.3 Experimental results

The design of the metamaterial Meta 1 has been experimentally tested in order to validate the system. To do so, the model has been 3D printed in acrylonitrile butadiene styrene (ABS) in two configurations: the simple cylinder without metamaterial and the cylinder with the horn-like integration and the metamaterial as depicted in figure 5.30. The experiments have been carried out in an acoustically isolated room by inserting the engine *Keli* inside the models. Measurements were taken with a sonometer at 1 m of the device, perpendicularly to the cylinder axis, as shown in figure 5.31, with the cylinder suspended by rubber bands to avoid any vibration.

(a) Whole system.

(b) Metamaterial Meta 1.

Figure 5.30: Cylinder with Meta 1 3D printed in ABS.

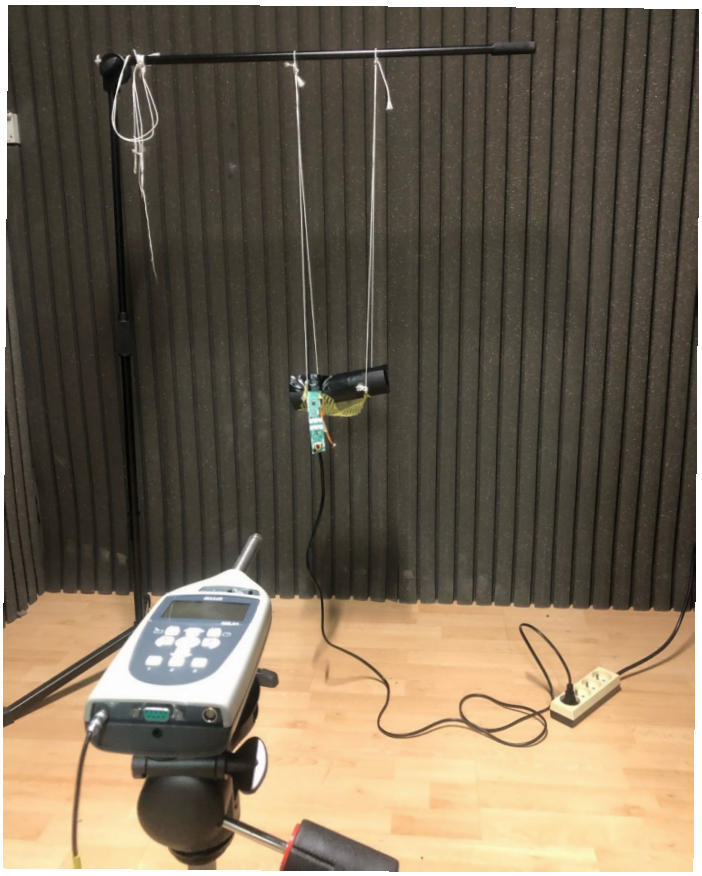

Figure 5.31: Experiments set-up in an anechoic room with the suspended model.

Even if the absolute SPL value has no meaning in itself since it is related to the saturation of the device, both results can be compared with each other. The SPL obtained are displayed

in figure 5.32 for the whole audible frequency range. At 1 250 Hz, an attenuation of 5.17 dB is obtained. Additionally, the peaks at 2 500 Hz and at the BPF are attenuated of 1.81 and 7.29 dB respectively. Nevertheless, the SPL is increased of 4.26 dB at 15 000 Hz with the metamaterial what highlights the sensitivity of the solution.

For a virtual microphone also placed at 1m of the cylinder axis, ACTRAN numerical results show an attenuation of 16.7 dB at 1 250 Hz. This means that the experiment decreases the gain of 69%. This could be due to the horn-like integration that deviates the air flux. The air then hits the metamaterial, creating noise due to turbulence effects. This points out the limitations of the numerical implementation of Lighthill analogy. Finally, some errors can also be induced by the 3D printing of the metamaterial, altering its geometrical parameters.

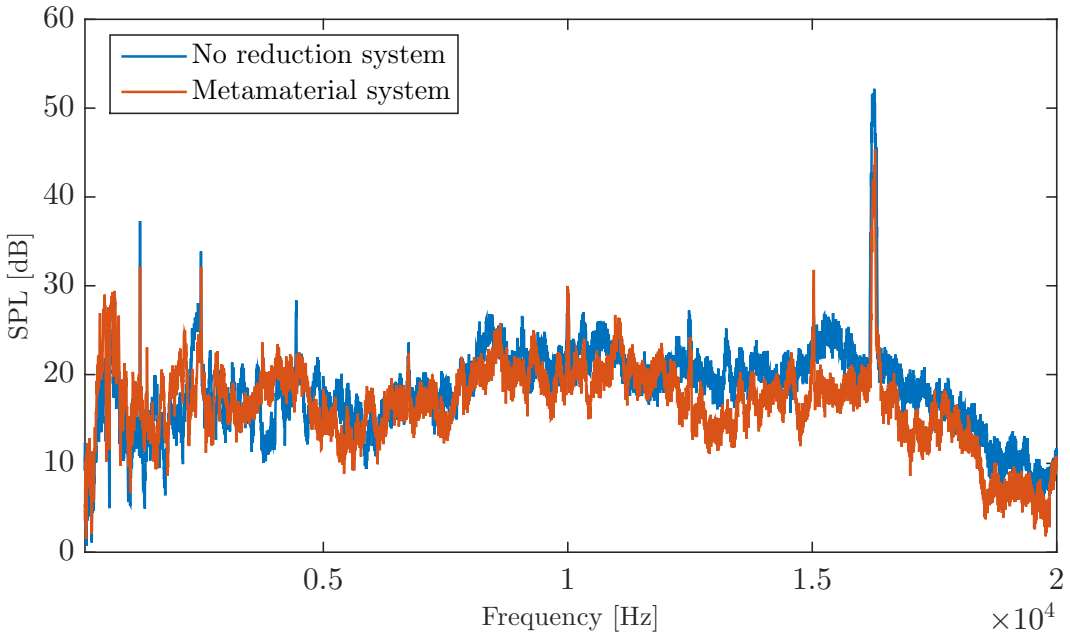

Figure 5.32: SPL as a function of the frequency from experiments for the engine *Keli* inside a simple cylinder and inside a cylinder with Meta 1.

5.4 Final combination

To conclude this chapter, the combination of both a metamaterial and an absorber has been implemented inside the same geometry to ensure that they do not alter each other in operation. It has been decided to use Meta 1, the most efficient metamaterial in addition to MPP 3 backed by a porous cavity. Emphasis is then placed on attenuating the first peak (at 1 250 Hz) and the one located at the BPF since the previous section has once again highlighted their major importance.

Figure 5.33 shows the SPL at microphone 1. Additionally, figure 5.34 presents the SPL on the polar set of microphones at 1 250 and 16 250 Hz. By lack of time, it was not possible to

simulate each case (Meta 1 and MPP 3 with porous materials) individually over the entire spectrum in order to decouple the effects of each.

The curve without attenuation system has a mean value over the whole spectrum of 15.92 dB. Similarly, the attenuation solution has a mean SPL of 6.64 dB, *i.e.* a mean attenuation of 9.27 dB that is satisfying. Furthermore, gains of 18.48 dB and 21.04 dB are achieved at 1 250 and 16 250 Hz respectively. These results prove the efficiency of the solutions implemented.

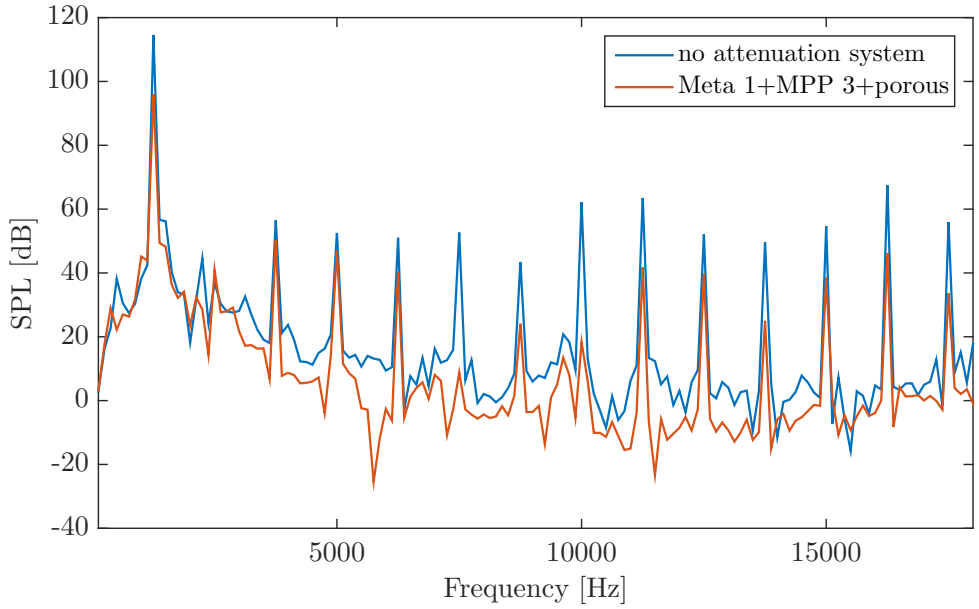

Figure 5.33: SPL as a function of the frequency at micro 1 without attenuation solution and for the combination of Meta 1 and MPP 3 porous backed.

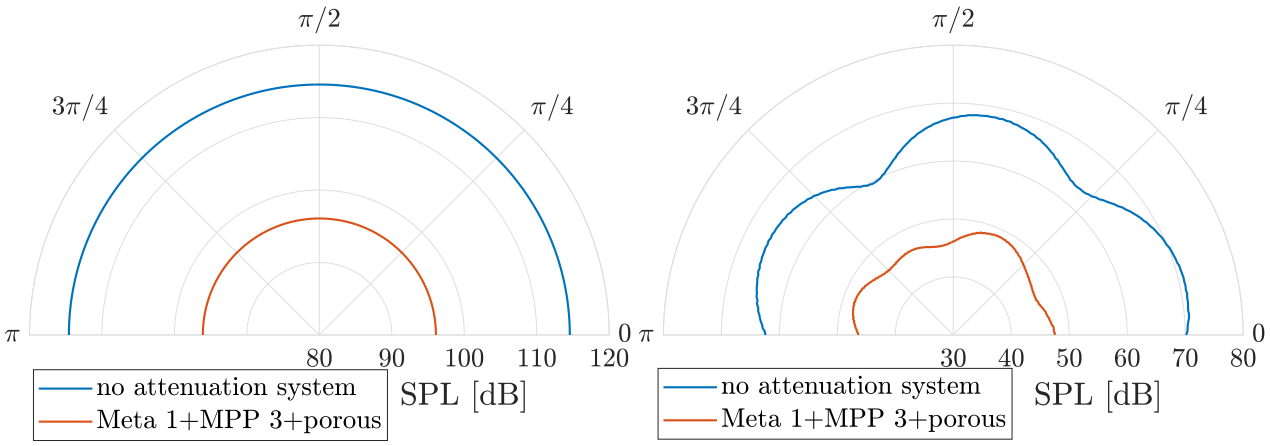

(a) 1 250 Hz. **(b)** 16 250 Hz.

Figure 5.34: SPL at different frequencies obtained at the polar set of microphones without attenuation solution and for the combination of Meta 1 and MPP 3 porous backed.

Chapter 6

Conclusion

6.1 Key results

In this master thesis, solutions have been presented and implemented in order to reduce the noise produced by a hair dryer. The whole acoustic work has been realised using Actran software and experimental tests have been carried out at the Babyliss research and development center. The work has been made gradually and the results related to the different stages are summarised below.

Firstly, an acoustic study has been realised by inserting a point source inside a rigid cylinder with thickness. The classical set-up, also used in the other chapters, composed of a mesh of 1.7 mm elements size and an ellipsoidal infinite surface, has been presented. The spectral response of such a case has been found to highlight the resonance frequencies of the system showing a higher SPL amplitude. Additionally, the different duct modes of propagation and cut-off frequencies have been discussed. More importantly, it has been shown that the special hair dryer casing does not add complexity to the results, demonstrating that the whole study can be realised on a simple cylinder.

Chapter 4 then develops the aspects linked to the real source of noise: the engine, the rotor-stator interaction being the most important contribution according to the literature. Lighthill analogy, a method used to deal with flow-induced noise, is thus theoretically developed and numerically implemented based on CFD results obtained with StarCCM+. It has been shown that the source terms obtained through the Actran CFD interface lacked consistency. Surface sources indeed present dipoles distribution at harmonics of the rotor rotation speed frequency that should only appear at the BPF in a perfect numerical case. This artefact is supposed to be linked to the blades CFD mesh that does not present a angular periodicity, creating an unbalanced effect in the results. Additionally, these truncated sources create very important peaks at the harmonics of the rotation frequency on the SPL frequency spectrum. It has been shown that even if these are due to numerical errors, they are also present in an experimental spectrum, in lesser extend, due to machining inaccuracies.

The last chapter concerns the development of solutions to attenuate the noise created at low and high frequencies, focusing on the BPF and the harmonics of the rotation speed frequency. Two types of passive systems have been described: absorbers and metamaterials. The key results are reported next.

Three types of acoustic absorbers have been implemented inside the cylinder thickness. Firstly, three porous linings have been tested at high frequencies: 3.5, 5.5 and 7.5 mm with a flow resistivity R equal to 22 000 N·s/m^4. It has been found that a thickness of 3.5 mm is not enough to correctly absorb the noise and that 7.5 mm lining allows to obtain a mean attenuation until 24 dB at the BPF but also a good attenuation at a broadband level for the whole spectrum. Furthermore, it has been observed that the attenuation increases with the flow resistivity for $R \in [18\,000; 26\,000]$ N·s/m^4. Secondly, three micro-perforated panels have been designed to work at the BPF. It has been found that the absorption obtained does not necessarily respect the theory based on normal incident waves stating that the lower the porosity, the higher the absorption. Additionally, a maximal attenuation of 9 dB is obtained at the BPF while lower efficiency is observed at other frequencies. It has then been decided to combine both solutions in order to get a broadband effect superimposed to a higher attenuation at the BPF by adding porous materials inside the MPPs cavities. In that case, a mean attenuation until 26 dB can be obtained at the BPF while showing at least 10 dB attenuation at the other frequencies contrarily to MPPs air backed. Regarding the experimental spectrum provided by BaByliss, this last solution has been considered as the best one.

Finally, metamaterials have been briefly introduced. A specific helical structure designed to work at 1 250 Hz has been presented and adjusted in order to see the influence of the geometrical parameters. It has been found that, according to the theory, the targeted frequency increases as the thickness of the metamaterial decreases or as the helix angle increases. However, no specific correlation has been observed regarding the variation of the internal and external radii of the metamaterial. Finally, even if a configuration has been found to create an important attenuation of 16.8 dB at the rotor rotation speed frequency, the sensitivity and the lack of robustness of this solution have been highlighted. Experiments have also shown an attenuation of 5.17 and 7.29 dB at 1 250 and 16 250 Hz respectively. However, the SPL at 15 000 Hz has been increased of 4.26 dB. These results at higher frequencies are more difficult to explain and interpret. As final result, a combination of both a metamaterial and a MPP porous backed as been shown to create interesting SPL decreases of 18.48 and 21.04 dB at 1 250 and 16 250 Hz respectively with a broadband uniform attenuation.

6.2 Further works

The present work implements passive attenuation solutions based on aero-acoustic sources. However, a major improvement could have been brought to what has been realised and a lot of studies remain to be done.

6.2.1 Major improvement

As mentioned in chapter 4, the CFD on which the aero-acoustic study is based is biased by the CFD mesh bringing artefact peaks in the SPL. A major obvious improvement that could have been realised in this work was to re-do the CFD analysis with a converged blade mesh presenting an angular periodicity in order to verify that the results here presented are well tainted by this numerical error and to re-do a correct acoustic analysis. This would also have made it possible to study the mitigation solutions with an excitation closer to reality. However, by lack of time, this was not an option for this master thesis.

6.2.2 Air flux verification

The attenuation solutions proposed are supposed to have no impact on the air flux passing inside the hair dryer as they are integrated inside the casing and do not block the passage. However, absorbers naturally modify the friction coefficient of the boundaries and metamaterials are added by hollowing out a cone in the casing. These two modifications influence the behaviour of the air flux in the internal casing. Even if this influence is supposed to be minimal, it could be interesting to simulate the cylinder with the final attenuation solutions in order to quantify the possible changes in the internal flux and verify that no flow rate drop appears.

6.2.3 Three speeds generalisation

The most important point to investigate to make these solutions is the generalisation of the solution to other rotor rotation speeds. As a matter of fact, the study has focused on one specific rotation speed frequency and therefore one BPF. However, devices as hair dryers often propose until two or three power levels and thus rotation speeds. In this context, a different conclusion would have been drawn at high frequencies, preferring porous linings acting on a broader frequency band. Another possible solution would have been to create MPPs with three different cavity thicknesses each centred on a specific frequency. However, at low frequencies, the metamaterial is not robust enough to deal with a large frequency range as it has been shown to only work at one frequency. The system should then be adapted through the investigation of a succession of metamaterials designed to act at different frequencies or by tuning the pitch variation of the helical pathway [45].

6.2.4 Engine modifications

Even if it was not a degree of freedom in this thesis, a suggestion for further studies is to redesign the rotor and/or the stator since their interference is the principal source of noise. For example, it has been demonstrated that the rotor-stator tone noise can be reduced thanks to a properly swept and leaned stator [11]. Interaction between the rotor and the stator can also be reduced thanks to a correct spacing between the two parts [18]. Moreover, the rotor noise in itself can be diminished. For instance, it has been demonstrated that the rotor blades skew angle plays an important role in the noise sources. It has notably been shown that a fan skew angle optimum for noise emission can be obtained depending on the

operating flow rate. Similarly, it has been demonstrated that leading-edge serration can also be an interesting solution to decrease the rotating blades noise [3, 19]. Additionally, it has been found that reducing blade tip clearance also reduces noise [14]. All these suggestions, and others, could be further investigated. An iterative process could indeed be realised with CAD model modifications, CFD and acoustic Lighthill analogy simulations.

6.2.5 Active noise control

In the present study, only passive systems have been added in the casing of the hair dryer. Nevertheless, it is known that active systems, even if they are more expensive, can present high performance in fan noise reduction. Further research could then be carried out regarding, to cite a few, wall mounted secondary acoustic sources [38], rotor casing mounted secondary air jets [44] or fan mounted directly on a electronic shaker [26]. These systems have a proven track record of tonal noise cancellation.

Appendix A

Fourier transform properties

The Fourier transform properties are briefly described here mentioning that $P(\omega)$ is the Fourier transform of $p(t)$ as:

$$p(t) \Leftrightarrow P(\omega). \tag{A.1}$$

The time-shift property of the Fourier transform is:

$$p(t - t_0) \Leftrightarrow P(\omega)e^{-i\omega t_0}. \tag{A.2}$$

The time and frequency scaling property is:

$$p(at) \Leftrightarrow \frac{1}{|a|}\ P(\frac{\omega}{a}). \tag{A.3}$$

Furthermore, the time derivative properties state that:

$$\frac{dp(t)}{dt} \Leftrightarrow i\omega P(\omega), \tag{A.4}$$

$$\frac{d^n p(t)}{dt^n} \Leftrightarrow (i\omega)^n P(\omega). \tag{A.5}$$

Finally, the convolution product of two signals in the time domain is converted as a product in the frequency domain following:

$$x(t) = f(t) \otimes g(t) = \int_{-\infty}^{\infty} f(\tau) \cdot g(t - \tau)\ d\tau \tag{A.6}$$

$$\Leftrightarrow X(\omega) = F(\omega) \cdot G(\omega). \tag{A.7}$$

Conversely,

$$x(t) = f(t) \cdot g(t) \Leftrightarrow X(\omega) = F(\omega) \otimes G(\omega) \tag{A.8}$$

where

$$X(\omega) = \frac{1}{2\pi} \int_{-\infty}^{\infty} Y(\sigma) \cdot Z(\omega - \sigma)\ d\sigma. \tag{A.9}$$

Appendix B

Bessel equation and functions

The complete Helmholtz equation (cf. equation 2.20) in cylindrical coordinates can be written as

$$\frac{\partial^2 P}{\partial r^2} + \frac{1}{r}\frac{\partial P}{\partial r} + \frac{1}{r^2}\frac{\partial^2 P}{\partial \phi^2} + \frac{\partial^2 P}{\partial z^2} + k^2 P = 0. \tag{B.1}$$

A solution of the following form can be applied:

$$P(r, \theta, z) = J_n(r; k_z)\ e^{in\theta}\ e^{ik_z z}, \tag{B.2}$$

if J_n satisfies

$$\frac{d^2 J_n}{dr^2} + \frac{1}{r}\frac{dJ_n}{dr} + \left((k^2 - k_z^2) - \frac{n^2}{r^2}\right) \cdot J_n = 0 \tag{B.3}$$

where k_z represents the axial wave number.

This equation can be transformed into the Bessel equation of order n by imposing the change of variables $\xi = \kappa r$ with $\kappa = \sqrt{k^2 - k_z^2}$:

$$\frac{\partial^2 J_n(\xi)}{\partial \xi^2} + \frac{1}{\xi}\frac{\partial J_n(\xi)}{\partial \xi} + \left(1 - \frac{n^2}{\xi^2}\right) \cdot J_n(\xi) = 0. \tag{B.4}$$

The solution of this type of differential equation is [49]:

$$J_n(\xi) = \sum_{m=0}^{\infty} \frac{(-1)^m}{m!\ (m+n+1)!} \left(\frac{\xi}{2}\right)^{2m+n}. \tag{B.5}$$

The first zeros of the function $\frac{\partial J_n(\xi)}{\partial \xi}$ are summarised in table B.1.

m	ξ_{0m}	ξ_{1m}	ξ_{2m}	ξ_{3m}	ξ_{4m}	ξ_{5m}
0	0.000	-	0.000	-	0.000	-
1	3.831	1.841	3.054	4.201	5.317	6.415
2	7.015	5.331	6.706	8.015	9.282	10.519

Table B.1: mth first zeros ξ_{mn} of the derivative of the Bessel functions $J'_n(\xi)$ for n=0, 1, 2, 3, 4 and 5.

Bibliography

[1] J.-F. Allard. *Propagation of sound in porous media : modelling sound absorbing materials*. Second edition. John Wiley and Sons, 2009. ISBN: 978-0-47074-661-5.

[2] *ANSI/ASA S1.1*. Acoustical Society of America (ASA), 2013.

[3] T. M. Biedermann, F. Kameier, and C. O. Paschereit. "Optimised test rig for measurements of aerodynamic and aeroacoustic performance of leading edge serrations in low-speed fan application". In: Volume 1: Aircraft Engine; Fans and Blowers; Marine (2018). DOI: 10.1115/GT2018-75369.

[4] X. Cai et al. "Ultrathin low-frequency sound absorbing panels based on coplanar spiral tubes or coplanar Helmholtz resonators". In: *Applied Physics Letters* 105.12 (2014). DOI: 10.1063/1.4895617.

[5] L. Cao et al. "Porous materials for sound absorption". In: *Composites Communications* 10 (2018), pp. 25–35. ISSN: 2452-2139.

[6] J. Carbajo et al. "Perforated panel absorbers with micro-perforated partitions". In: *Applied Acoustics* 149 (2019), pp. 108–113. ISSN: 0003-682X.

[7] S. Cho et al. "Tunable two-dimensional acoustic meta-structure composed of funnel-shaped unit cells with multi-band negative acoustic property". In: *Journal of Applied Physics* 118.16 (2015), p. 163103. DOI: 10.1063/1.4934360.

[8] N. Curle. "The Influence of Solid Boundaries upon Aerodynamic Sound". In: *Proceedings of the Royal Society of London. Series A, Mathematical and physical sciences* 231.1187 (1955), pp. 505–514.

[9] J. P. Dalmont, C. J. Nederveen, and N. Joly. "Radiation impedance of tubes with different flanges: numerical and experimental investigations". In: *Journal of Sound and Vibration* 244.3 (2001), pp. 505–534. ISSN: 0022-460X.

[10] M. E. Delany and E. N. Bazley. "Acoustical properties of fibrous absorbent materials". In: *Applied Acoustics* 3.2 (1970), pp. 105–116. ISSN: 0003-682X.

[11] E. Envia and M. Nallasamy. "Design selection and analysis of a swept and leaned stator concept". In: *Journal of sound and vibration* 228.4 (1999), pp. 793–836. ISSN: 0022-460X.

[12] J. E. Ffowcs Williams and D. L. Hawkings. "Sound Generation by turbulence and surfaces in arbitrary motion". In: *Philosophical transactions of the Royal Society of London. Series A: Mathematical and physical sciences* 264.1151 (1969), pp. 321–342. ISSN: 1364-503X.

[13] J. E. Ffowcs Williams and D. L. Hawkings. "Sound generation by turbulence and surfaces in arbitrary motion". In: *Philosophical Transactions of the Royal Society of London. Series A, Mathematical and Physical Sciences* 264 (1969), pp. 321–342. ISSN: 1364-503X.

[14] T. Fukano, Y. Takamatsu, and Y. Kodama. "The effects of tip clearance on the noise of low pressure axial and mixed flow fans". In: *Journal of sound and vibration.* 105.2 (1986-3). ISSN: 0022-460X.

[15] *GDTech Engineering*. https://www.gdtech.eu/.

[16] R. Ghaffarivardavagh et al. "Ultra-open acoustic metamaterial silencer based on Fano-like interference". In: *Physical Review B* 99 (2019). ISSN: 2469-9950.

[17] C. Goffaux et al. "Evidence of Fano-like interference phenomena in locally resonant materials". In: *Physical review letters* 88.22 (2002).

[18] J. Han et al. "Stator modification methods for diagonal flow fans to achieve noise reduction of rotor-stator interaction". In: *Journal of mechanical science and technology* 36.2 (2022), pp. 785–796. ISSN: 1738-494X.

[19] G. Herold, F. Zenger, and E. Sarradj. "Influence of blade skew on axial fan component noise". In: *International journal of aeroacoustics* 16.4-5 (2017), pp. 418–430. ISSN: 1475-472X.

[20] M. S. Howe. *Theory of vortex sound*. Cambridge texts in applied mathematics. Cambridge University Press, 2003. ISBN: 1-107-13305-X.

[21] H. Hubbard. *Aeroacoustics of Flight Vehicles: Theory and Practice. Volume 1. Noise Sources*. 1991.

[22] Y. S. Joe, A. M. Satanin, and C. S. Kim. "Classical analogy of Fano resonances". In: *Physica Scripta* 74.2 (2006), pp. 259–266. DOI: 10.1088/0031-8949/74/2/020.

[23] S. Kimihiro et al. "Pilot study on wideband sound absorber obtained by combination of two different micro-perforated panel (MPP) absorbers". In: *Acoustical Science and Technology* 30.2 (2009), pp. 154–156. DOI: 10.1250/ast.30.154.

[24] F. Krömer. "Sound emission of low-pressure axial fans under distorted inflow conditions". PhD thesis. 2018. DOI: 10.25593/978-3-96147-089-1.

[25] F. Krömer, F. Czwielong, and S. Becker. "Experimental investigation of the sound emission of skewed axial fans with leading-edge serrations". In: *AIAA Journal* 57 (2019). ISSN: 0001-1452.

[26] G. C. Lauchle, J. R. MacGillivray, and D. C. Swanson. "Active control of axial-flow fan noise". In: *The Journal of the Acoustical Society of America* 101.1 (1997), pp. 341–349. ISSN: 0001-4966.

[27] M. J. Lighthill. "On Sound Generated Aerodynamically. I. General Theory". In: *Proceedings of the Royal Society of London. Series A, Mathematical and physical sciences* 211.1107 (1952), pp. 564–587. ISSN: 1364-5021.

[28] Z. Liu et al. "Acoustic measurement of a 3D printed micro-perforated panel combined with a porous material". In: *Measurement: journal of the International Measurement Confederation* 104 (2017), pp. 233–236. ISSN: 0263-2241.

[29] X. Ma and Z. Su. "Development of acoustic liner in aero engine: a review". In: *Science China Technological Sciences* 63 (2020). DOI: 10.1007/s11431-019-1501-3.

[30] D. Y. Maa. "Potential of micro-perforated panel absorber". In: *The Journal of the Acoustical Society of America* 104.5 (1998), pp. 2861–2866. DOI: 10.1121/1.423870.

[31] J.-L. Migeot, J.-P. Coyette, and G. Lielens. *Acoustics*. IJK Numerics, 2016.

[32] Y. Miki. "Acoustical properties of porous materials: Modifications of Delany-Bazley models". In: *Journal of the Acoustical Society of Japan (E)* 11.1 (1990), pp. 19–24. ISSN: 2185-3509.

[33] C. Naify et al. "Scaling of membrane-type locally resonant acoustic metamaterial arrays". In: *The Journal of the Acoustical Society of America* 132.4 (2012), pp. 2784–2792. ISSN: 0001-4966. DOI: 10.1121/1.4744941.

[34] C. Naify et al. "Transmission loss and dynamic response of membrane-type locally resonant acoustic metamaterials". In: *Journal of Applied Physics* 108.11 (2010). ISSN: 0021-8979. DOI: 10.1063/1.3514082.

[35] *NASA Space Flight Human-system Standard, Volume 1: Crew Health*. 2014.

[36] A. Oberai, F. Roknaldin, and T. Hughes. "Computational procedures for determining structural-acoustic response due to hydrodynamic sources". In: *Computer methods in applied mechanics and engineering* 190.3 (2000), pp. 345–361. ISSN: 0045-7825.

[37] World Health Organisation. "Environmental Health Criteria 12: Noise". In: (1995).

[38] F. Pla et al. "Active noise control of low speed fan rotor-stator modes". In: (1996). DOI: 10.2514/6.1997-1641.

[39] I. Prasetiyo, I. Sihar, and A. S. Sudarsono. "Realization of a thin and broadband micro-perforated panel (MPP) sound absorber". In: *Applied acoustics* 183 (2021). ISSN: 0003-682X.

[40] Y. J. Qian et al. "Investigation on micro-perforated panel absorber with ultra-micro perforations". In: *Applied Acoustics* 74.7 (2013), pp. 931–935. ISSN: 0003-682X.

[41] H. Ruiz, P. Cobo, and F. Jacobsen. "Optimization of multiple-layer micro-perforated panels by simulated annealing". In: *Applied Acoustics* 72.10 (2011), pp. 772–776. ISSN: 0003-682X.

[42] Free Field Technologies SA. *ACTRAN 2022 User's Guide. Vol. 1: Installation, operations, theory and utilities*. 2011.

[43] K. Sakagami et al. "Sound absorption characteristics of a single micro-perforated panel absorber backed by a porous absorbent layer". In: *Acoustics Australia* 39 (2011).

[44] M. Steger et al. "Tone noise reduction of a turbofan engine by additional aerodynamical blade forces". In: *16th AIAA/CEAS Aeroacoustics Conference*. DOI: 10.2514/6.2010-3982.

[45] M. Sun et al. "Broadband acoustic ventilation barriers". In: *Phys. Rev. Applied* 13 (2020). DOI: 10.1103/PhysRevApplied.13.044028.

[46] Y. Tao et al. "Recent progress in acoustic materials and noise control strategies – A review". In: *Applied materials today* 24 (2021). ISSN: 2352-9407.

[47] *TOA sound equipment*. https://www.toa.co.in/.

[48] J. M. Tyler and T. G. Sofrin. "Axial Flow Compressor Noise Studies". In: *SAE transactions* 70 (1962), pp. 309–332. ISSN: 0096-736X.

[49] G. N. Watson. *A Treatise on the theory of Bessel functions*. Cambridge University Press, 1944.

[50] Z. Yang et al. "Membrane-type acoustic metamaterial with negative dynamic mass". In: *Phys. Rev. Lett.* 101 (2008), p. 204301. DOI: 10.1103/PhysRevLett.101.204301.

[51] X. Zhu et al. "Implementation of dispersion-free slow acoustic wave propagation and phase engineering with helical-structured metamaterials". In: *Nature Communications* 7 (2016). ISSN: 2041-1723.